THE EVAPORATION OF MANGANESE FROM LIQUID IRON

THE EVAPORATION OF MANGANESE FROM LIQUID IRON UNDER REDUCED PRESSURES IN THE TEMPERATURE RANGE 1320°C TO 1810°C

By

TERRENCE DOUGLAS AURINI, B.ENG.

A Thesis
Submitted to the Faculty of Graduate Studies
in Partial Fulfilment of the Requirements
for the Degree
Master of Engineering

McMaster University
April 1964

MASTER OF ENGINEERING (1964)
(Chemical Engineering)

McMASTER UNIVERSITY
Hamilton, Ontario.

TITLE: The Evaporation of Manganese from Liquid Iron, at Reduced Pressures in the Temperature Range 1320° to 1810°C

AUTHOR: Terrence Douglas Aurini, B.Eng. (McMaster University)

SUPERVISOR: Professor R. G. Ward

NUMBER OF PAGES: (ix), 134

SCOPE AND CONTENTS:

This thesis presents a review of the theory of evaporation of pure substances with respect to kinetic and mechanistic models. These concepts are applied to multi-component evaporation and a model for the evaporation of solute atoms from a solvent is postulated. The evaporation experiments were performed on Fe 1% Mn melts at a constant pressure of approximately 10 microns over a temperature range of 1320° to 1810°C. The correlation between the experimental results and the expected theoretical results is discussed thoroughly in terms of surface control and diffusion control.

ACKNOWLEDGEMENTS

The author wishes to express his sincere gratitude to his research supervisor, Dr. R. G. Ward, whose direction and advice throughout the whole project led to a successful completion of the work.

In addition, the author would like to thank Dr. G. R. Purdy for his consultation on the mathematical analysis, Dr. C. M. Crowe for his suggestions on various aspects of the problem, Mr. H. Neumeyer whose technical suggestions and assistance allowed the experimental work to be performed efficiently, Mr. K. Pollock whose advice on computer programming was indeed beneficial, and to all the members of the Chemical Engineering and Metallurgical Engineering departments, who contributed to the solution of the problem through many discussions.

Special thanks go to Dr. G. Hines and the Steel Company of Canada for providing the services of the Chemical Laboratory for the chemical analyses.

This research project was made possible by a National Research Council Operating Grant.

TABLE OF CONTENTS

Subject Page

CHAPTER III

TABLE OF TABLES

TABLE OF FIGURES

CHAPTER I

INTRODUCTION

1.1 The Application of Vacuum in Metallurgical Processes

The concept of utilizing vacuum techniques in the treatment of metals is not a new one. The first United States patent for a vacuum furnace was received in 1873, however, it is only in the past decade or so that any significant progress has been made.

While there are certainly numerous individual reasons for applying vacuum processes in metallurgy, they may be categorized into three general groups:

1.1 (i) The Protective Nature of Vacuum

Heat treatment operations such as annealing, hardening and tempering, carried out in vacuum, result in no carbon reduction, and also result in bright finishes with no surface contamination. Heat treating in vacuum applies only to alloys with relatively low vapor pressures, such as steels. Alloys of Al, Zn, Mg and Pb with high vapor pressures would evaporate quickly as is experienced with the severe dezincification of a 70 – 30 brass[35], at approximately 600°C.

1.1 (ii) The Production of Gas Free Alloys

Degassification of metallic components is quite important, for the gas content of many alloys is often responsible for poor mechanical properties. The elimination of soluble gases under vacuum has been shown to have remarkable beneficial effects on the mechanical properties of certain alloys.[36, 42]

The working pressures in these vacuum systems are often less than the dissociation pressures of iron nitrides and hydrides, thus preventing their formation, and avoiding detrimental inclusions.

1.1 (iii) Separation Properties

One of the most important properties inherent in vacuum technique is the enhancement of the separation of two or more components. Vacuum distillation is widely used in chemical engineering as a means of separating many organic substances (vitamins from animal and fish oil[53]) which if heated to temperatures even approaching their normal boiling points, results in thermal decomposition. The application of vacuum permits the process to operate at a lower temperature, without fear of decomposition, and with a net increase in the rate of evaporation to allow separation in a reasonable length of time.

In considering distillation as a means of separating metallic components, it is obvious that it is impossible to operate at temperatures necessary to effect evaporation (for iron the boiling point is 2740°C). However, at low temperatures in the neighbourhood of the melting point (1539°C for iron) the net rate of evaporation is increased sufficiently to allow separation, if the system is operated under vacuum.

As in the separation of organic substances, metallic components also must have a significant difference in volatility before distillation can be considered as separation technique.

Olette[46] has considered the distillation of Mn, Cu, Sn, Si, S, As, P from iron, and Spendlove[40] discusses the distillation of Cd, Zn, Mg, Te, Bi, and Sb from tin and lead, and the vacuum leaching of Al from Al – Si alloys with high vapour pressure Zn.

1.2 The Scope of the Present Work

A natural sequel to the considerations discussed in section 1.1 (iii) is the determination of the kinetics of the evaporation process. It is the purpose of this thesis to study the evaporation of manganese from iron to elucidate the nature of its removal. The evaporation of manganese is postulated to occur by a first order reaction. Reaction rate constants have been determined in a temperature range 1320°C to 1810°C and have been plotted according to the Arrenhius relationship in order to determine the activation energy of the process. The results of the evaporation experiments are discussed thoroughly in terms of evaporation (surface) control and diffusion control.

CHAPTER II

THEORETICAL CONSIDERATIONS

A Theoretical Analysis of Rate of Evaporation for Single Component Systems

2.1 (i) Knudsen Maximum Rate Equation

The maximum evaporation rate from a liquid or a solid has been expressed by Knudsen[1], utilizing the kinetic theory of gases[2]. The phenomenon of evaporation is similar for liquid metals as for ordinary liquids, with perhaps one reservation. When considering evaporation from a metal, one usually regards the evaporation as a surface phenomenon since the hydrostatic pressure is so great, even at very low depths, that the vapour tension of most metal vapours is never large enough for bubble formation to occur.

From the kinetic theory of gases, the number of molecules ν striking a unit area of surface per unit time is given by,

$$\nu = \frac{N\bar{C}}{4}$$

where N is the number of molecules per unit volume, $\bar{C}$ is the mean velocity of the molecules and m is the mass per molecule. Then,

$$m\nu = \frac{\rho\bar{C}}{4} = W_{max}$$

Where ρ is the density of the vapour and W_{max} is the maximum number of molecules striking a surface of a substance per unit time when in equilibrium with its vapour.

Also, $\rho = \frac{Mp^{o}}{RT}$ from the ideal gas equation.

Where p^{o} is the saturation pressure of the vapour, M is the molecular weight of the vapour, R is the gas constant and T is the absolute temperature.

Also, $$\bar{C} = \sqrt{\frac{8p^o}{\pi\rho}} = \sqrt{\frac{8RT}{\pi M}}$$

therefore, $$W_{max} = \frac{1}{4} \cdot \frac{Mp^o}{RT}\sqrt{\frac{8RT}{\pi M}}$$

$$= p^o\sqrt{\frac{M}{2\pi RT}} \qquad (1)$$

Equation (1) represents the maximum number of molecules striking a surface at a constant temperature and pressure, hence at equilibrium this must equal the maximum number of molecules able to leave or evaporate from a surface.

In actual fact, for real gases, fugacities should be used instead of pressures, but at low pressures such as those used in evaporation studies, it can be shown that the fugacity and pressure are approximately equivalent[43].

2.1 (ii) Effect of Residual Pressure on the Maximum Rate of Evaporation

Equation (1) represents the maximum rate of evaporation, that is the rate of evaporation into a perfect vacuum. If, however, the pressure above the evaporating surface has an absolute value p, due either to high evaporation fluxes, or to a residual gas pressure, the maximum rate is then reduced to,

$$W = (p^o - p)\sqrt{\frac{M}{2\pi RT}} \qquad (2)$$

Ilschner and Humbert[51], studying the rate of evaporation of pure liquid silver and aluminum, using different residual pressures of argon, found that in the low pressure range, the rate was independent of pressure. For liquid silver the constant rate range was 0 to 1,000 microns and for aluminum it was 0 to 100 microns of mercury.

Spendlove[40] determined the effect of pressure on the rate of evaporation of zinc at constant power input. The results show the rate of evaporation is largely independent of pressure until 100 microns pressure is reached when the power input is 1.2 kilowatts. (figure 3.1)

2.1 (iii) The Rate of Evaporation Less than the Maximum Rate

In experimental work, it has been found that the experimental evaporation rate for some materials under vacuum is often less than the maximum evaporation rate calculated from equation (2). This observation results in the necessary introduction of an unknown factor α, referred to as the evaporation coefficient, such that,

$$W = \alpha\ (p^{o} - p) \sqrt{\frac{M}{2\pi RT}} \qquad (3)$$

According to Wyllie,[3] there are three means of accounting for these apparent discrepancies:

(a) A molecule arriving at the liquid surface, from the vapour, can possibly be reflected rather than condensed.

(b) Molecules that do condense may do so in a different configuration from that of the underlying substance (applicable to solids only).

(c) The molecular species involved may be wrongly identified.

With reference to liquids, the first possibility is the most probable.

In a recent compilation, Hirth and Pound[4] report that simply bonded liquids of spherically symmetrical molecules, which evaporate or condense as single atoms, should exhibit no surface constraints and should follow the maximum evaporation rate deduced by Knudsen, that is where the evaporation coefficient $\alpha = 1$.

This assertion has been verified experimentally by Knudsen[5] who found $\alpha = 1$ for clean liquid mercury. Neumann and Schmoll[6], studying the evaporation of liquid potassium, determined $\alpha \approx 1$. Volmer and Estermann[7] repeating the work of Knudsen, verified that $\alpha = 1$ for liquid mercury. Holden et al[8] determined $\alpha = 1$ for liquid beryllium. In a more recent work, Ward[10] found $\alpha = 1$ for liquid iron. Knacke and Stranski[11] report results performed on solid metal films of copper, silver and cadmium, showing that $\alpha = 1$. Alty and MacKay[9], studying metallic systems report $\alpha = 1$ for carbon tetrachloride (CCl_4), which is a spherically symmetrical molecule, like the metallic molecules or uniatoms.

2.2 (i) Maximum Rate of Evaporation from Classical Chemical Kinetics

Penner[16] approaches the overall evaporation flux from another direction, that of classical chemical kinetics. If the rate of loss of molecules from a given volume V, $-dMv/dt$, is proportional to the number of molecules, Ms, in the liquid surface at time t, then,

$$-\frac{dMv}{dt} = kMs \qquad (4)$$

where k is the specific evaporation constant.

Equation (4) leads to,

$$W = k\,\rho/n^{1/3} \qquad (5)$$

where ρ is the density of the evaporating species, n is the number of molecules per unit volume and W is the rate of evaporation per unit area.

The rate constant k is written in the Arrenhius form as a function of temperature;

$$k = A \exp(-\Delta Ev/RT) \qquad (6)$$

where ΔEv is the activation energy for evaporation and A is a frequency factor.

Equations (5) and (6) lead to:

$$W = \rho\,(2\Delta Hv/M)^{1/2}/V_f^{1/3}n^{1/3} \exp(-\Delta Hv/RT) \qquad (7)$$

or,

$$W = p_s\,(M/2\pi RT)^{1/2}\left[2\sqrt{2\pi}\,e\,(V_f/V)^{1/2}\right] \qquad (8)$$

where e is the base of the natural logarithm, p_s is the vapor pressure, V is the volume per molecule in the liquid state, ΔHv is the heat of vaporization and V_f is the free volume defined by Kincaid and Eyring[19], which is discussed in a later section.

Equation (8) is seen to be quite similar to Knudsen's equation (1) for maximum evaporation, except for the bracketed term. At room temperature the bracketed term tends to unity, and the Knudsen equation is obeyed. However, at higher temperature, V_f/V varies with temperature and equation (8) and equation (1) no longer have the same dependence on temperature and hence are no longer equivalent. Utilizing the classical theory of unimolecular reactions yields an expression which is equivalent to Knudsen's equation at any temperature. This analysis yields an expression:

$$W = 2e \quad p^{o} \, (M/2\pi RT)^{1/2} \qquad (8a)$$

which is Knudsen's equation multiplied by a factor (2e).

2.2 (ii) Maximum Rate of Evaporation from Droplets

Penner[23] investigated the evaporation from droplets, with respect to Knudsen's modified maximum rate equation for spherical droplets:

$$-\frac{dr}{dt} = \frac{p^{o}}{\rho_L} \sqrt{\frac{M}{2\pi RT}} \qquad (9)$$

where r is the radius of the droplet, p^{o} is the vapour pressure of the liquid and ρ_L is the liquid density.

In terms of the classical chemical kinetics discussed in the previous section, the maximum rate of evaporation may be written as:

$$-\frac{dr}{dt} = e \sqrt{\frac{2\Delta Hv}{RT\gamma}} \quad U \quad \exp\,(-\,\Delta Hv/RT) \qquad (10)$$

where e is the base of the natural logarithm, γ is the ratio of the specific heat at constant pressure over the specific heat at constant volume and U is the velocity of sound in the liquid.

In almost every case compared, the value of the rate of evaporation determined by equation (10) was less than that determined from equation (9). In general, however, the agreement was reasonable except for the highly associated liquids like water, methanol and ethanol. The agreement for long chain hydrocarbons became less with increasing chain length from n-pentane to n-octane.

It is not too surprising that associated molecules and long chain hydrocarbons do not yield the rate predicted by the Knudsen equation, since equation (10) was derived assuming all the molecules were free spheres.[23]

2.3 Maximum Rate of Evaporation from the Theory of Absolute Rates

Apart from the simple kinetic approach to overall evaporation fluxes, which obviously deserve merit, there has been a movement towards developing a mechanistic expression for evaporation. This development has been expressed by Hirth and Pound[4] utilizing the theory of absolute rates.[12] This approach describes the probability of an atom evaporating, as a function of a frequency of decomposition (atoms or molecules decaying from liquid state to gas state) ν^*, and the concentration of atoms in the activated state M . The overall evaporation is then given by:

$$W = \nu^* M^* \tag{11}$$

$$= \nu^* M_s \exp(-\Delta G^*/kT) \tag{12}$$

but,

$$\Delta G^* = \Delta H^* - T\Delta S^* \tag{13}$$

therefore,

$$W = \nu^* M_s \exp(\Delta S^*/k) \exp(-\Delta H^*/kT) \tag{14}$$

The entropy term is made up of several terms, such as those due to rotational, vibrational and translational energies; expressing each in terms of its partition function:

$$W = \nu^* M_s \frac{f^*_{tr} \, f^*_{vib} \, f^*_{rot}}{f_{tr} \, f_{vib} \, f_{rot}} \exp(-\Delta H^*/kT) \tag{15}$$

where M_s is the concentration of atoms in the normal surface state, f^* and f are the partition functions for activated and ground states respectively, ΔG^* is the Gibbs free energy of activation and ΔH^* is the activation enthalpy.

Although this approach has been followed by several authors,[13-17] the differences lie in the various interpretations of ν^* and f^*. Hirth and Pound[4] maintain that the present state of knowledge justifies only a very simple interpretation of the activated state. Glasstone et al[12] factor out the translational degree of freedom from the activated state by factoring its partition function f^*_{tr}. West and Zener,[18] in order to balance the degrees of freedom in the normal state, factor the vibrational partition function in the direction of activation, f_{vib}.

Therefore,

$$W = \nu^* M_s \frac{f^*_{tr}}{f_{vib}} \exp(-\Delta G^{*1}/kT) \qquad (16)$$

where ΔG^{*1} is the Gibbs free energy change with a degree of freedom missing from each state.

From the defining equations for f^*_{tr} and f_{vib},[12] equation (16) may be written:

$$W = M_s \omega \exp(-\Delta G^*/kT) \qquad (17)$$

where,

$$\omega = \frac{kT}{h}\left[1 - \exp\left(-\frac{h\nu}{kT}\right)\right]^{-1} \qquad (18)$$

where k is Boltzmann's constant, h is Planck's constant and ν is the vibrational frequency in the normal state.

Thus the overall evaporation flux at steady state will be:

$$W \equiv M_s \omega \exp(-\Delta G^*/kT) = p^\circ \sqrt{\frac{M}{2\pi RT}} \qquad (19)$$

2.4 The Accommodation Coefficient

As mentioned previously,[1] it has been found experimentally in many cases, that the actual rate of evaporation is somewhat less than that predicted by the Knudsen equation for maximum evaporation. In some cases the experimental value is considerably less than the predicted value. This deviation from ideality has necessitated the introduction of a coefficient, known simultaneously as the evaporation coefficient, (α_v), the condensation coefficient (α_c) and the accommodation coefficient. Depending on whether condensation or evaporation is occurring, the suitable coefficient is used. The present work deals mainly with evaporation and hence the evaporation coefficient α_v, will be used.

2.4 (i) Definition

The evaporation coefficient has been defined in several ways:

1) The fraction of atoms striking a liquid or solid surface, which condense. Conversely $(1 - \alpha)$ is the fraction of atoms returning to the vapour.
2) The effective surface area available for evaporation.
3) The experimentally determined rate of evaporation over the theoretical rate for evaporation into a perfect vacuum.

2.4 (ii) Experimental Results

Values of $\alpha_v < 1$ have been observed for several polar compounds, as listed in table I. Spingler,[20] investigating the evaporation of ammonium chloride (NH_4Cl) determined α_v to vary between 1/340 and 1/2,560, decreasing with increasing temperature. Melville and Gray[21] report the evaporation coefficient of red phosphorus as being between 10^{-7} and 10^{-9}. For this latter case, Stranski and Wolff[24] show that the very low value observed is due to the molecular species taking part in the evaporation and condensation. When phosphorus and arsenic evaporate, they do so as diatomic molecules P_2 and As_2, however, the equilibrium vapour consists of P_4 and As_4. The emission of P_4 or As_4 requires an energy equal to the heat of evaporation λ. The emission of $2P_2$ and $2As_2$ requires an energy of $(\lambda + \theta)$ where θ is the heat required for dissociation, and is large. The energy required to evaporate one molecule is therefore $1/2\ (\lambda + \theta)$ which is much greater than that anticipated, thus accounting for the low results.

For the present time it will be assumed that all the results presented in Table 1 show that the evaporation coefficient is less than one for the species mentioned, ignoring the effect of experimental errors such as errors in surface temperature measurement or surface contamination, which will be discussed in a later section.

2.4 (iii) Tentative Explanation for Accommodation Coefficient Less than One

From the experimental results it is obvious that when α was observed to be unity, the molecular species were generally spherically symmetrical, while when $\alpha < 1$ the units involved were not spherically symmetrical.

In systems where the molecular species is non-symmetrical and where association can occur, it is easy to imagine certain restrictions or constraints occurring in the liquid state. The most obvious restriction would be rotational, thus the rotational degree of freedom in the liquid state (not in the vapour) would experience constraints.

Kincaid and Eyring[19] introduce the concepts of "free volumes" and "free angle ratios" to elucidate the abnormalities occurring in associated liquids. They apply the notion of restricted rotation of associated molecules to account for abnormalities observed in thermal heat conductivities, heat capacities and dielectric constants.

A liquid is treated as being composed of individual molecules or atoms which move in a volume V_f, defined as the free volume, in a potential field due to its neighbours. The volume V is the total volume of the liquid divided by the number of molecules, and is related to V_f by:

$$V_f = C^3 (V^{1/3} - d)^3 \qquad (19a)$$

where d is the molecular diameter

C is a term characteristic of the type of packing

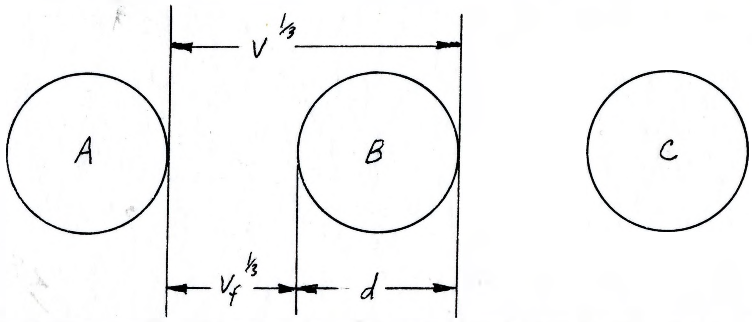

The free angle ratio, δ, is defined as the ratio of the partition functions for restricted rotation in the liquid phase and for free rotation in the vapour phase. For water and methanol the observed abnormalities cannot be explained by the free volume alone, which is normal, but rather by the product δV_f, which is abnormal, thus pointing out the effect of restricted rotation in the liquid.

Wyllie,[3] in his evaporation studies, found a very close correlation between the evaporation coefficient and the free angle ratio for benzene, carbon tetrachloride and highly associated liquids (Table I). Chloroform ($CHCl_3$) was the only discrepancy, but this was to be expected, for although $CHCl_3$ is highly polar, it does not form hydrogen bonds. These results are interpreted in terms of the structure of the surface of liquids, which Wyllie reasons can be compared, locally at least, to that of a solid bound on one side by a layer of freely rotating molecules.

2.4 (iv) Correlation between Accommodation Coefficient and the Free Angle Ratio

Hirth and Pound[4] and Penner[15], apply the theory of absolute reaction rates to explain some of the abnormalities observed with polar liquids. Since rotational restrictions occur in the liquid state, the rotational partition functions for the activated and restricted states, f^{*}_{rot} and f_{rot} respectively, are factored from equation (16):

$$W = \nu^{*} M_s \frac{f^{*}_{tr}}{f_{vib}} \frac{f^{*}_{rot}}{f_{rot}} \exp(-\Delta G^{*11}/kT) \qquad (20)$$

where ΔG^{*11} is the free energy of evaporation with two degrees of freedom removed.

From equation (15), this can be expanded to:

$$W = M_s \ \omega \ \frac{f^{*}_{rot}}{f_{rot}} \exp(-\Delta H^{*}/kT) \qquad (21)$$

When considering condensation of a polar molecule, it is obvious that in order to condense, the molecule must be in the proper orientation, otherwise, it will be repelled, thus the overall condensation flux (Wc) can be written:

$$Wc = \frac{f^{*}_{rot}}{f_{rot_v}} \quad p^{o}\sqrt{\frac{M}{2\pi RT}} \qquad (22)$$

where f_{rot_v} is the rotational partition function in the vapour.

The total flux under non-equilibrium conditions is(equation (2)):

$$W = \frac{(f^{*}_{rot})}{(f_{rot_v})} \quad (p^{o} - p)\sqrt{\frac{M}{2\pi RT}} \qquad (23)$$

From equation (23) it is seen that:

$$\alpha_v = \alpha_c = \frac{(f^{*}_{rot})}{(f_{rot_v})} \qquad (24)$$

There exist two possibilities arising from equation (24):

1) The rotational degrees of freedom are activated in the activated state, that is, there is no constraint due to rotational hindrance, thus $f^{*}_{rot} = f_{rot_v}$ or:

$$\alpha_v = \alpha_c = 1 \qquad (25)$$

as is the case for spherically symmetrical molecules.

2) The rotational degrees of freedom are not activated in the activated state, that is, there are constraints on the system due to rotational hindrance, thus $f^{*}_{rot} = f_{rot}$ which means that:

$$f^{*}_{rot}/f_{rot_v} = f_{rot_L}/f_{rot_v}$$

where subscripts L and v refer to the liquid and vapour respectively which according to the definition of Kincaid and Eyring[19] is the free angle ratio, thus:

$$\alpha_v = \alpha_c = \delta < 1 \qquad (26)$$

Wyllie[3] mentions the possibility of an adsorbed surface layer being important, resulting in a two step mechanism:

$$\text{Liquid} \underset{W_{L2}}{\overset{W_{L1}}{\rightleftharpoons}} \text{Adsorbed Layer} \qquad (27)$$

$$\text{Adsorbed Layer} \underset{W_{L4}}{\overset{W_{L3}}{\rightleftharpoons}} \text{Vapour} \qquad (28)$$

Combining (27) and (28) Hirth and Pound determine (from the kinetic solutions):

$$\alpha_v = \alpha_c = 1/\left[1 + (1/5) \exp\left\{(\Delta H^*_{L2} + \Delta H_{hole} - \Delta H^*_{L3})/kT\right\}\right] \quad (29)$$

where ΔH_{hole} is present due to the probability of an adsorption hole being available on the surface for adsorption to occur. The results of part I of table I agree with equation (29) except for the case of benzene.

2.4 (v) Other Interpretations of the Accommodation Coefficient

(a) Kirkwood[24] believes that the free volume theory used in the preceding derivations, which assumed that each molecule exhibited gas-like thermal motion, surrounded by the force-fields of its neighbours, might be replaced by a more exact treatment.

(b) The experimentally determined evaporation coefficient for water varied so greatly from that predicted by Knudsen, that Lype[26] was prompted to investigate the system. He suggests that hydrogen bonds exist throughout the water and hence results in a psuedo-crystalline solid, making the Polanyi-Wigner theory of escape of molecules from the surface of a solid applicable.

(c) Another investigation by Zwick[26] presents the evaporation phenomenon by means of a simple kinetic model, which he does not intend to take into account the restrictions due to rotation hindrances of associated molecules. He expresses the condensation and evaporation limits as a function of the accommodation coefficient α.

2.5 Factors Affecting the Accommodation Coefficient

2.5 (1) Contamination Effects on Accommodation Coefficient

It has been shown for clean liquid metals that the evaporation coefficient is unity. However, Knudsen found that for his mercury experiments, any slight surface contamination resulting from a poor vacuum, reduced the evaporation coefficient by a factor as great as 1,000. Hickman and Torpey[33] found for still water, that the evaporation coefficient varied from 0.001 to 0.02, depending on the degree of purity.

2.5 (ii) Surface Temperature Effects on Accommodation Coefficient

It is apparent in evaporation studies that the surface temperature of an evaporating liquid can be below that of the bulk liquid, due to the loss of heat required for evaporation. This phenomenon is more likely to occur where large evaporation fluxes are predominant, or where a liquid has a low thermal conductivity. Surface cooling has been noted by Bradley[28] and Littlewood and Rideal[22] in the study of long chain hydrocarbons, and by Spendlove[50] during the rapid evaporation of zinc from unstirred melts.

Failure to take surface temperature lowering into account will necessarily result in a lowering or an apparent lowering of the evaporation coefficient.

2.5 (iii) Variation of Accommodation Coefficient with Temperature

Stranski and Wolff,[24] in questioning the application of Knudsen's equation, to all forms of evaporation, suggest that it is wrong to assume that the evaporation coefficient is always constant. They suggest a temperature dependence of the type:

$$\alpha_v = a \exp(-EK/kT) \qquad (30)$$

where EK is an excitation energy of condensation.

A precise relationship between the accommodation coefficient and temperature is not known. Experimental results have shown a strong dependence of α on temperature, and yet other results illustrate no temperature dependence. Spingler,[20] investigating the evaporation of ammonium chloride determined that the accommodation coefficient decreased with increasing temperature, from 1/ 340 at 118°C to 1/2,560 at 221°C. Melville and Gray's measurements on the evaporation of red phosphorus displayed the same temperature dependence, with the accommodation coefficient varying from 10^{-7} at 305°C to 10^{-9} at 408°C. Bennewitz[34] experimented on the evaporation of cadmium and found the accommodation coefficient independent of temperature, having a value of unity over the range 198 to 234°C. In their work on liquid mercury, Volmer and Estermann[7] determined the accommodation coefficient to be unity between 0°C and 50°C, on the other hand, in studying the evaporation of solid mercury from −39°C to −64°C, they found a steady decrease from unity to 0.85.

From the limited experimental data available it is somewhat difficult to determine the actual dependence of the accommodation coefficient on temperature. If any dependence at all is present, it would seem to favour a decrease of α with increasing temperature. This dependence of α on temperature is valid for solids, since the desorption rate increases faster than the surface diffusion rate as the temperature increases, resulting in reflection rather than nucleation.

2.6 Validity of the $\alpha - \delta$ Relationship

Two schools of thought exist as to the validity of equation (26). The first group, and the majority, believe that sufficient experimental data has been accumulated to confirm the theory that in some liquids, internal constraints do exist, which hinder their evaporation rates. The second opinion is that the apparent agreement between the accommodation coefficient and the free angle ratio is more or less fortuitous and any apparent decrease in the accommodation coefficient from unity is explained logically by errors in surface temperature measurement (Littlewood and Rideal[22] believe this to be true) and/or by the presence of impurities.

The primary motive for acknowledging the validity of equation (26) is the obvious agreement between the accommodation coefficient and the free angle ratio as seen from table I. In order to discount the postulation that a reduction in the accommodation coefficient is due to a reduction in the surface temperature, caused by surface cooling, Alty and MacKay[9] measured the thermal accommodation coefficient, α_T, for free evaporation of water, where:

$$\alpha_T = \frac{Tv}{Ts} \qquad (31)$$

where Tv is the r.m.s. temperature of the evaporating vapour and Ts is the temperature of the substrate.

If the accommodation coefficient is less than unity only because of surface temperature lowering, it is obvious that the thermal accommodation coefficient defined by equation (31) must also be less than unity. Alty and MacKay determined the thermal accommodation coefficient for water to be unity, while the accommodation coefficient was determined to be 0.04. This experiment thus eliminates surface cooling as the primary reason for observed accommodation coefficients less than unity for water.

The results in part I of table I show experimental values of the accommodation coefficient of glycerol and water to be 0.05 and 0.02 respectively. Part II of table I, however, show for the same to systems that the accommodation coefficients are 1 and 0.4. Hickman and Torpey[33] conclude that the accommodation coefficients for high purity glycerol and water, and consequently all the compounds in table I are actually unity and any discrepancy may be rationalized by the presence of impurities.

Hirth and Pound, however, do not agree that surface contamination is responsible for a lowering of the accommodation coefficient. They note that in the experiments where low values of accommodation coefficients were determined (for glycerol and water) the evaporation took place from stationary surfaces, whereas in the cases where the accommodation coefficients approached unity, the evaporation took place from a rapidly moving, turbulent stream. The argument put forth is that the high turbulence created in the stream is sufficient to continuously disrupt the liquid-vapour interface and hence disrupt the surface dipole. Also, in such a turbulent stream, the actual evaporating surface area could conceivably be somewhat greater than that calculated, resulting in an apparent increase in the accommodation coefficient.

2.7 Variations from Theory

From the experimental data available, it is seen from part III table I that the only apparent discrepancies with the theories of evaporation occur in the experimental accommodation coefficients for the long chain hydrocarbons. Although they are polar, and non-symmetrical the experimental accommodation coefficients are equal to unity (cupric acid, tetradecanol and dodecanol have accommodation coefficients less than unity due to surface cooling), showing disagreement with the theory. Eyring[17] concludes that in long chain or large planar molecules, the rotational degrees of freedom in the activated state are activated, hence they exhibit no constraints and should follow the evaporation kinetics of equation (25).

B Theoretical Analysis of Rate of Evaporation for Multi-Component Systems

In metallurgy, vacuum is used as a refining and separation technique and thus it is necessary to know the relative volatilities of various metallic components. From the relative volatilities, the rates of evaporation may be determined, and hence the time for refinement or separation may be estimated. The use of vacuum conditions as a refining technique demands that the impurities present in a substrate must have a greater volatility than the substrate (the refining reaction also occurs by gas evolution in some cases, which is obviously enhanced by a vacuum). For the use of vacuum as a separation technique the only criterion is that the volatilities be different, that is the rates of evaporation are different. A rough estimate of relative volatilities may be gained by analysis of the vapour pressure curves of figure I.

2.8 (i) Maximum Rate of Evaporation Under Vacuum

Similar to the single component evaporation discussed in the first section of this chapter, multi-component evaporation can be described by a slight revision of the Knudsen maximum rate equation, that is:

$$W_{max} = p_v \sqrt{\frac{M}{2\pi RT}} \qquad (32)$$

where p_v is the vapour pressure of the component concerned, above its solution in the metal substrate.

Any element going into solution with another element, experiences a decrease in its vapour pressure from p^o (the vapour pressure of the element above its pure solution) to p_v (the vapour pressure of the element above its solution with another element). The value p_v/p^o is called the activity of that element in the solution:

$$a = p_v/p^o = \gamma N \qquad (33)$$

where a is the activity, γ is the activity coefficient and N is the mole fraction of the element in solution.

Therefore:

$$W_{max} = \gamma N p^o \sqrt{\frac{M}{2\pi RT}} \qquad (34)$$

Similarly from before,

$$W_{max} = \alpha \gamma N p^o \sqrt{\frac{M}{2\pi RT}} \qquad (35)$$

Multicomponent systems, undergo the same modes of evaporation and restrictions discussed in section A for single component systems, and much of the material presented in the first section may be conveniently expanded for the multi-component systems. The present discussion, however, deals with the evaporation of metal uniatoms, which are spherically symmetrical and should be free from any constraints. Certain differences which are inherent in the evaporation of multi-component systems are discussed fully in later sections.

2.8 (ii) Evaluation of the Maximum Rate of Evaporation

To determine the maximum rate of evaporation from equation (34) or (35), requires a knowledge of vapour pressures (figure I) of pure solutions, as well as values of activity coefficients.

For ideal solutionsobeying Raoult's law, $\gamma = 1$, but for non-ideal solutions γ is greater or less than unity depending upon whether the solution displays positive or negative deviation, respectively, from Raoult's law. With reference to the iron system, nickel, cobalt, chromium[57] and manganese[56] are quite similar to iron in chemical properties and atomic size, thus they would tend to form ideal solutions with iron.

Elements which form intermetallic compounds with iron, tend to continue the attraction into the liquid state, resulting in a negative deviation from Raoult's law. Silicon, aluminum and titanium form intermetallic compounds with iron (seen from phase diagrams) as do magnesium and tellurium with lead, and hence in liquid solution of iron or lead respectively these elements would exhibit negative deviation from Raoult's law. For positive deviations from Raoult's law to occur, the self-interactions between like atoms in a solution must be greater than the mutual interactions resulting in a tendency towards separation into two phases. Copper in iron behaves in this manner,[58] as the Cu-Cu interactions and the Fe-Fe interactions are more preferred than the Cu-Fe interactions.

2.8 (iii) Quantitative Evaporation Treatment

The steel industry is interested in a quantitative study of the evaporation of various elements from a solution in iron. Olette[46] has postulated such a method, using Knudsen's maximum rate equation, in the form:

$$W_{max} = \gamma N p^{o} \sqrt{\frac{M}{T}} \sqrt{\frac{1}{2\pi R}} \qquad (36)$$

Consider a hypothetical solution of A gm of Fe and B gm of element Y at $T^{o}K$, under vacuum. After t seconds the distillate yields x gm Fe and y gm of Y, thus the melt contains (A - x) gm Fe and (B - y) gm Y. From equation (36), the rate of evaporation of iron is:

$$\frac{dx}{dt} = \gamma_{Fe} \left[\frac{(A-x)}{M_{Fe}} \Big/ \left\{ \frac{(A-x)}{M_{Fe}} + \frac{(B-y)}{M_{Y}} \right\} \right] p^{o}_{Fe} \sqrt{\frac{M_{Fe}}{T}} \sqrt{\frac{1}{2\pi R}} \qquad (37)$$

A similar expression may be written for dy/dt, the rate of evaporation of Y. In order to obtain a quantitative treatment of the possibility of eliminating element Y from Fe under vacuum, the rate of evaporation of Y is divided by that of iron:

$$\frac{dy}{dx} = \left(\frac{\gamma_Y}{\gamma_{Fe}}\right) \left(\frac{p^o_Y}{p^o_{Fe}}\right) \sqrt{\frac{M_{Fe}}{M_Y}} \left(\frac{B-y}{A-x}\right) \qquad (38)$$

or:

$$\frac{dy}{dx} = \beta \left(\frac{B-y}{A-x}\right) \qquad (39)$$

where β is defined as the evaporation coefficient, but it should be noted that β has no relation to the ordinary evaporation coefficient, α_v, which has been discussed at length in section A.

Separating the variables, and integrating equation (39) yields:

$$y = -\frac{B}{A^{\beta}} (A-x)^{\beta} + B \qquad (40)$$

or,

$$\frac{100y}{B} = 100 \left(1-\frac{100x}{A} \cdot \frac{1}{100}\right)^{\beta} + 100 \qquad (41)$$

It can be seen that $\frac{100y}{B} = y^1$ and $\frac{100x}{A} = x^1$ are the respective percentages of element Y and Fe lost through evaporation.

Then:

$$y^1 = 100 - 100 \left(1-\frac{x^1}{100}\right)^{\beta} \qquad (42)$$

Equation (42) is represented graphically in figure 2, showing the percent of Y lost through evaporation versus Fe lost (at constant temperature) as a function of the new evaporation coefficient β. It is seen that β is a measure of the ease of refinement of an element from iron, under vacuum. Calculation of β from equations (38) and (39) can enable one to predict the amount of the element evaporated or if β is less than one, predict that its removal from iron under vacuum is impossible.

2.8 (iv) The Effect of Pressure on the Maximum Rate of Evaporation

The effect of residual pressure on the maximum rate of evaporation has been discussed for single component evaporation in section 2.1 (ii) and it is evident that residual pressure will have the same retarding effect on the rate of evaporation from multi-component systems.

Ward[10] investigated the evaporation rate of manganese from liquid iron under pressures ranging from two microns up to atmospheric pressure, and he determined that the rate of evaporation was independent of pressure in the low range from 0 to 70 microns which is similar to the findings of Ilschner and Humbert[51], and Spendlove[40], for single component systems.

2.9 (i) Vacuum Distillation as a Chemical Reaction

Parlee et al[44] caution against the indiscriminate use of classifying metallurgical reaction rates, which are diffusion controlled, as an ordered chemical reaction, such as first order, second order etc. In studying the carbon-oxygen reaction, they postulate that the rate of reaction at the melt surface is:

$$r = \frac{D_o}{\delta_o} A \left[C_o - \frac{k^1 p_{co}}{C_c} \right] \qquad (43)$$

where D_o is the diffusion coefficient of oxygen in iron, δ_o is the boundary layer thickness, A is the area of the gas metal interface, C_o and C_c are the bulk oxygen and carbon concentrations respectively, k^1 is the reaction rate constant for the surface reaction and p_{co} is the partial pressure of carbon monoxide.

They point out that the growing trend in metallurgy would be to classify equation (43) as a first order reaction, but emphasize that this procedure is possible only if $C_o >> k^1 p_{co} / C_c$, in which case:

$$r = kC_o \quad \text{where } k = \frac{D_o}{\delta_o} A \tag{44}$$

which is a first order reaction with respect to the oxygen concentration.

Mauret and Vorsanger[45] studied the effect of association on evaporation rates and found that the rate of loss of weight was a straight line function of time, between the initial evaporation period and the last fraction of evaporation. The slope of the line produced is thus proportional to the rate of transformation of the substance from liquid to vapour and may be thought of as a zeroth order reaction:

$$\frac{dm}{dt} = k \tag{45}$$

integrating equation (45):

$$m_i - m = kt$$

where m_i is the initial mass, m is the mass at any time t and k is the zeroth order reaction rate constant or the specific evaporation coefficient.

Similarly, Ward[10] proposes first order kinetics for the evaporation of manganese, chromium, aluminum and copper from solutions of iron under vacuum. In this case, the loss of solute atoms, M, from the solvent to the vapour are represented by the reaction:

$$M_{\text{Liquid}} \longrightarrow M_{\text{Vapour}} \tag{46}$$

This reaction is first order with respect to the concentration of the solute in the solvent, that is:

$$\frac{1}{A} \frac{dC_M}{dt} = - k^{11} \frac{C_M}{V} \tag{47}$$

where C_M is the weight present of the solute in solvent, V is the volume of the melt, A is the evaporation surface area, and k^{11} is the specific evaporation constant.

Integrating equation (47) yields:

$$\int_1^2 \frac{dC_M}{C_M} = k^{11} \frac{A}{V} \int_1^2 dt$$

or,

$$\ln C_{M_2} / C_{M_1} = - \frac{k^{11}A}{V} (t_2 - t_1) \qquad (48)$$

From the solution of equation (47), it is seen that a plot of the log of the concentration of the metallic species versus time will yield a straight line, whose slope will determine k^{11} the specific evaporation constant. For various solutes evaporating from a common solvent at constant temperature, the k^{11} values will determine which components evaporate quickest. Figures 10 to 24 illustrate that a plot of log C versus time does yield a straight line, verifying the postulation of first order kinetics.

2.9 (ii) Energy of Activation:

The specific reaction rate constant for any reaction, be it zeroth order, first order, second order etc, is related to temperature by the Arrenhius equation:[43]

$$k^1 = Ae^{-E/RT} \qquad (49)$$

where A is the frequency factor, and E is the energy of activation for the process.

Equation (49) may be written:

$$\log k^1 = -2.303 \frac{E}{R} \frac{1}{T} + \log A \qquad (50)$$

It is evident from equation (50) that a plot of the specific reaction rate constant, k^1, versus $1/T^{\circ}K$ will yield a straight line whose slope determines the activation energy for the reaction.

Mauret and Vorsanger[45] experimented on the evaporation of water, methanol, ethanol and benzene, toluene and cyclohexane at different temperatures, and assuming a zeroth order reaction, were able to determine the activation energy for evaporation. In applying chemical kinetics to this system they were able to show conclusively that the activation energy for evaporation is larger than the energy of vapourization for associated liquids, such as water, methanol and ethanol. This technique also demonstrated that for non-associated liquids such as benzene, toluene and cyclohexane, these two energies are numerically identical, within the limits of experimental errors.

Similarly, for first order reactions where Mn, Cu and Cr evaporate from iron,a plot of the type discussed in the previous section should yield the activation energy for evaporation of these elements. This activation energy is discussed in a later section.

The applicability of the Arrenhius plot has its limitations over wide temperature ranges, and it has been shown[52] that for certain chemical reactions, the activation energy varies with temperature .

2.10 Evaporation from Stirred Melts

The first part of chapter II dealt with the evaporation of pure liquids and it was shown that only the surface phenomena are of interest i.e. desorption from the surface is the rate limiting step in evaporation from pure liquids. In considering a two component system, where a dilute solute is evaporating from a solvent, the simple case of surface control is no longer applicable and several other factors could also be rate limiting:

1) The transport of the solute atoms through the bulk of the melt to the vicinity of the gas – liquid interface.
2) The transport of the solute atoms across an effective liquid boundary layer to the gas – liquid interface.
3) The desorption of the solute atoms from the liquid metal surface into the gas phase.
4) The transport of the solute atoms across an effective gas boundary layer into the bulk of the gas phase.
5) The transport of the solute atoms through the bulk gas phase to the condensation or growth surfaces.
6) The growth or condensation of solute atoms.

In a vacuum system where the melt in question is heated and stirred by an induction coil, several of the preceding rate limiting steps can be excluded as having little or no effect upon the rate of solute evaporation.

The stirring currents produced by the induction coil would eliminate transport of the solute through the bulk as being a possible rate limiting step. In vacuum, the transport of the solute atoms through the bulk gas phase would be unlikely to be a rate limiting step, and providing the vapor pressure of the solute plus solvent is less than 1,000 microns of Hg[54], the transfer of solute atoms through a gas boundary layer would not be rate limiting. The water – cooled chamber would present no obstruction to condensation and hence this factor may be eliminated.

In this type of system considered, the only possible rate limiting steps are the diffusive flow of the solute atoms across an effective liquid boundary layer, and the desorption of the solute atoms from the liquid metal surface.

2.10 (i) Transport in the Liquid Phase

The model used to describe the transfer of solute from the bulk liquid phase to the liquid-gas interface is that of Machlin[48] which is fashioned after the penetration theory of Higbie[55]. This model assumes the presence of a frictionless, laminar layer near the interface through which the solute must diffuse to reach the liquid-gas interface.

The application of Fick's second law for this transient process, imposing the appropriate boundary conditions[49] yields an expression:

$$\frac{dM}{dA} = \frac{2}{\sqrt{\pi}} \sqrt{Dt^1}\,(C_o - C_s) \qquad (51)$$

where $\frac{dM}{dA} \equiv$ loss of solute per unit area of liquid-gas interface

$C_o \equiv$ average concentration of solute in the melt

$C_s \equiv$ concentration of solute at the liquid-gas interface

$D \equiv$ diffusivity of solute in liquid solvent

$t^1 \equiv$ contact time of liquid with gas.

To determine the rate of solute decrease, in terms of concentration:

$$\frac{dC_o}{dA} = \frac{dM}{dA} \cdot \frac{dA}{dt} \cdot \frac{1}{V} \qquad (52)$$

where $\frac{dA}{dt} \equiv$ rate of disappearance of surface

$V \equiv$ volume of the melt

Equation (51) reduces to:

$$-\frac{dC_o}{dt} = \left(\frac{8Dv}{\pi r h^2}\right)^{1/2} (C_o - C_s) \qquad (53)$$

where $v \equiv$ velocity of the liquid surface at the outer radius

$r \equiv$ radius of the melt

$h \equiv$ height of the melt

Under constant conditions of melt size and power input equation (53) may be written as:

$$-\frac{dC_o}{dt} = k_1 (C_o - C_s) \qquad (54)$$

or

$$W_D = k_1 (C_o - C_s) \qquad (55)$$

where $W_D \equiv$ rate of solute transfer in gm/cm^2/sec.

$k_1 \equiv$ specific evaporation constant for diffusion.

2.10 (ii) Desorption from the Liquid Surface

The rate of transport of solute atoms from the surface of the liquid into the gas phase is described by the Knudsen equation for evaporation from multicomponent systems:

$$W_E = \alpha \gamma N_s p^o \sqrt{\frac{M}{2\pi RT}} \qquad (56)$$

where $N_s \equiv$ mole fraction of solute at the surface

The Knudsen equation, equation (56), represents the maximum rate of solute transfer, ie it assumes the surface concentration of the solute is the same as that of the bulk and there is no frictionless boundary layer present. If, however, there is diffusional resistance, the surface concentration will be lowered, and the Knudsen equation will still apply, although predicting a lower transfer due to a lower surface concentration.

Equation (56) may be written in terms of surface concentration:

$$W_E = k_2 \quad C_s \tag{57}$$

where $W_E \equiv$ rate of solute transfer in gm/cm^2/sec.

$k_2 \equiv$ specific evaporation constant for evaporation

2.11 Limiting Cases for Evaporation Rate Control

The amount of solute transferred through the frictionless liquid boundary layer must equal that which is desorbed from the liquid surface, that is

$$W_D = W_E \quad \text{or}$$

$$k_1 \; (C_o - C_s) = k_2 \, C_s \tag{58}$$

from which

$$C_s = \left(\frac{k_1}{k_1 + k_2} \right) C_o \tag{59}$$

2.11 (i) Evaporation as the Rate Limiting Step

In order that the desorption of solute atoms from the liquid surface be the rate limiting step, the surface concentration must equal the bulk concentration ie $C_s = C_o$. From equation (59) this means that

$$\frac{k_1}{k_1 + k_2} = 1 \tag{60}$$

To satisfy equation (60), $k_1 >> k_2$, which means that specific evaporation constant for evaporation control is much less than that for diffusion control and hence the process is controlled by the surface desorption reaction.

2.11 (ii) Diffusion as the Rate Limiting Step

If the overall solute transfer is controlled by diffusion of the solute in the liquid, a boundary layer like the one described in section 2.10 (i) must exist, where the surface concentration is much less than the bulk concentration ie $C_s << C_o$. To satisfy this condition, it is seen from equation (59) that:

$$\frac{k_1}{k_1 + k_2} << 1 \qquad (61)$$

or $$k_2 >> k_1$$

This means that the specific evaporation coefficient for evaporation control is much greater than that for diffusion control and hence all the resistance to mass transfer lies in the diffusion through the boundary layer.

2.11 (iii) Simultaneous Diffusion and Desorption Control

Combining equations (59) and (57) yields an expression describing the rate of solute evaporation, W, in terms of both diffusion and evaporation parameters:

$$W = \left(\frac{k_1 \ k_2}{k_1 + k_2} \right) C_o \qquad (62)$$

The specific evaporation constant may be expressed by an overall specific evaporation constant k:

$$W = kC_o \qquad (63)$$

Equation (63) describes the evaporation process as an ordered reaction of the first order and is analogous to equation (47).

If the process is evaporation controlled, equation (57) may be written:

$$W = k_2 C_o \qquad (64)$$

Comparing equations (63) and (64) it is obvious that k/k_2 is a measure of the extent of the evaporation or diffusion control. If $k/k_2 \longrightarrow 1$ it is obvious that evaporation control predominates and conversely if $k/k_2 \longrightarrow 0$, diffusion control predominates.

Ward[10] experimentally determined k for Mn, Cu, and Cr evaporating from dilute solutions in liquid iron. The ratio k/k_2 was calculated at 1570 to be 0.22, 0.49 and 0.95 respectively, illustrating that at 1570°C, manganese evaporation is predominately diffusion controlled, copper is controlled by both diffusion and evaporation and that chromium is largely controlled by diffusion. It was noted in these experiments that as the ratio C_s/C_o increased, the p_o value for the system decreased, suggesting that perhaps a plot of p_o vs C_s/C_o might be a good criterion for predicting the rate limiting step in evaporation of multicomponent systems i.e. the $p_o \gamma$ value for any element could be calculated, and from the plot the controlling step may be determined.

CHAPTER III

EXPERIMENTAL APPARATUS AND TECHNIQUE

3.1 Experimental Apparatus

3.1 (i) The Power Supply

The power unit used a vertically mounted, water cooled motor generator set with an output frequency of 3,000 cycles per second and with a maximum power output of 30 kilowatts. In this set, the generator output is fed to an induction coil through an associated network of condensers to create a resistive load, ie where the voltage and current are in phase resulting in maximum power being generated. The circuit conditions, such as voltage, resistance, amperage and power were indicated and controlled on a master control panel.

3.1 (ii) The Vacuum Chamber

A Stokes induction heated vacuum furnace was used, fully modified for application to this work. The vacuum was produced by a 3 H.P. Stokes rotary piston backing pump in series with two parallel connected Stokes 2,500 watt, four inch booster pumps, capable of reaching a pressure of 1 micron Hg. An external Balzer mechanical pump was used to evacuate the secondary vacuum chambers, such as the air locks on the sampling and addition outlets.

The vacuum chamber is depicted pictorially in figures 3(a) and (b) and schematically in figure 4. The experimental setup allowed the performance of several functions while under vacuum: taking samples from the melt, taking temperatures with an immersion thermocouple, taking temperatures continuously by optical pyrometry, measuring the pressure by electric and manometric techniques, observing the melt, making alloying additions, performing condensation experiments, introducing controlled atmospheres and pouring the melt.

(a) The experiments were performed on carbon free and carbon saturated melts. For carbon free runs, the sampling tubes were made from 6 mm silica tubing with a wall thickness of 1 mm. The silica tubing was cut into 9 inch lengths and from each of these, two 4-1/2 inch tubes, with one closed end, were formed by melting with an oxy-acetylene torch. The tubes were cut on a diamond cutting wheel to form an opening 3/4 inch by 1/4 inch, approximately 3/4 inch from the closed end. This opening allowed the taking of a cylindrical sample of dimensions 3/4 inch long by 0.2 inch diameter.

The sample tubes used are shown in figure 5 (a) and (b). Figure 5 (a) represents the first type used, utilizing a small set screw to hold the tube in place while sampling. This method proved too time consuming, particularly on the high temperature runs, when relatively short sampling times were needed. The alternative sampling device is shown in figure 5 (b). The same procedure was used for making the sampling tube, however, the mode of holding it while sampling was different. The sample tube was held by a swagelock fitting with a polyethylene ferrule, so the tube could be securely held and released by merely adjusting the pressure on the ferrule. This latter method proved much less time consuming, and generally more satisfactory than the former method.

The use of silica sample tubes in carbon saturated melts is rendered unsatisfactory due to the reduction of silica by the carbon, at temperatures below 1540°C. This occurs according to the reaction:

$$SiO_2 + 2C \longrightarrow 2CO + Si$$

The evolution of CO gas makes it impossible to collect any sample, so the sampling was performed with graphite sample tubes, seen in figure 5 (c). The graphite tubes were made from 1/2 inch diameter carbon rods, cut into 3 inch lengths, drilled with a 1/4 inch bit leaving one end closed. The open end was tapped. An opening was filed in the graphite, 1/2 inch from the closed end, with dimensions 3/4 inch by 1/4 inch. The tapped end was screwed onto the end of the sample pipe which was fitted with a threaded rod, to secure the sample tubes during sampling.

(b) The immersion thermocouple was used to calibrate the two-colour optical pyrometers and consisted of Pt-Pt 13% Rh thermocouple wire of 0.020 inch diam. The set-up illustrating the use of this thermocouple is pictured in figure 6. The thermocouple insulators were manufactured from alumina, and the immersion protective sheath was a metamic material which is a combination metal and ceramic. In this particular case, the pure ceramic material was alumina which was interlaced with a continuous network of high melting point molybdenum, to increase the thermal conductivity and also to increase the ductility in order to reduce thermal stresses. The type shown in figure 6 (a) was capable of measuring temperature continuously up to 1800°C as long as vacuum conditions persisted.

(c) The operating temperature was measured continuously by a two-colour optical pyrometer. The obvious advantages of this type of temperature measurement were that the temperature measurement was continuous, making for more precise temperature control and that no correction needed to be made for variations in emissivity . The two types of two colour pyrometers used were, a Latronics Colouratio pyrometer with temperature ranges 1100 - 2100/2100 - 3100°C, with a recorder output of 100 mv, and a Milletron Thermoscope with temperature ranges of 800 - 1300/1300 - 1800°C, with a recorder output of 100 mv.

(d) The pressure in the vacuum chamber was measured by several different methods, some serving as checks on others.

The fore pump pressure and the rough vacuum in the chamber were measured using Stokes electrical gauges with pressure ranges from 0.1 to 20 mm Hg and 1 to 1,000 microns Hg respectively. This type of gauge operates on the principle that the heat lost by a hot filament, due to thermal conduction through the residual gas, is a function of the number of molecules present per unit volume, and thus a function of the pressure. A Balzer thermal conductivity gauge served as a check on the pressure in the tank. The Balzer gauge was calibrated by an external source and was perhaps a more reliable estimate of the chamber pressure.

The low pressure in the tank was measured by a Stokes cold cathode ionization gauge with a pressure range of 0 to 20 microns Hg. In this type of vacuum gauge, a set current of electrons is omitted thermionically from an incandescent filament and attracted to a cold cathode. The electrons ionize a fraction of the gas molecules, which create an ion current which is directly proportional to the molecular density and hence the pressure. This gauge operated well when no heating was present, but seemed to be drastically changed by a small increase in pressure, so more confidence was placed in the Balzer reading under molten conditions.

Whereas the electronic gauges measured the total pressure in the chamber, including that due to condensable materials, the pressure created by non condensable vapours was measured by an Edwards Vacustat. This gauge is a tilting version of the McLeod gauge, based on the application of Boyles Law. The pressure range measured was 1 to 1,000 microns Hg.

A Bourdon pressure gauge was utilized to measure the chamber pressure in the range from atmospheric pressure to 30 inches Hg vacuum. This gauge was primarily used to measure the amount of controlled atmosphere bled into the vacuum chamber.

(e) The vacuum chamber contained three observation ports, one mounted on the door to observe the melt behaviour during melting, one mounted on the top through which the optical measurements were taken and where the melt surface could be observed, and one on the top which allowed observation of the melt while pouring.

(f) Provision was made for the addition of alloying materials through an external air lock on the side of the furnace. The alloying charge was added to the bucket, then the air lock chamber was evacuated using the Balzer pump, a vacuum gate valve was opened and the charge bucket was positioned over the melt, and the charge was dropped into the melt. Any number of alloying additions could be made without disrupting the pressure in the vacuum chamber. The charging bucket assembly is shown in figure 7.

(g) The condensation experiments were performed, utilizing the same vacuum port as that used to measure the chamber pressure with the Balzer thermal conductivity gauge. The water-cooled copper condensing plate is shown in figure 8. Thin copper sheets 1/16 inch thick by

2-3/4 inch diameter were bolted to the water cooled plate, to act as a growth site for any impinging metallic vapours.

(h) Controlled atmospheres such as argon and natural gas could be added to known pressures, through a vacuum valve.

(i) The induction coil was fitted in an asbestos box at the center of the vacuum chamber, located along a rotating axis which was connected by a series of gears and chains, through a vacuum lock, to a control wheel outside the vacuum chamber. The melt could then be poured under vacuum, from outside the system, while observing the operation through the sight glass mounted on the top.

3.1 (iii) The Induction Furnace

The induction coil was a 3/8 inch copper tubing, interwoven with asbestos tape to insulate the turns. The coil was wound to form a cylindrical heating zone 7 inches long with a diameter of 6 inches.

Three types of refractories were used for the molten iron experiments:

(a) Lumag 741 (alumina + magnesia)

(b) Zircoa F-5C (zirconia)

(c) Kaiser 102 (magnesia)

A detailed chemical analysis of the refractories used is presented in table 2.

The zircoa F-5C crucible is a prefired mixture and was centered in the induction coil, and the excess volume between the crucible and the coil was packed with either Lumag 741 or Kaiser 102. Lumag 741 and Kaiser 102 are fine grained powder refractories which were rammed, about a form, precut to the size of crucible desired. The rammed crucible has several advantages over the prefixed crucible:

(a) With a rammed crucible, the thermal stresses are not nearly as severe as those in a prefired crucible, where cracking occurs.

(b) The size of the crucible made from a ramming mixture may be altered as desired, simply by changing the size of the form.

The ramming form was constructed from a 3 inch diameter graphite rod, 11 inches long, tapering from 3 inches at the top to 2-7/8 inches at the bottom, for ease of removal. A 1/2 inch hole was drilled near the top to remove the graphite block after the firing procedure and a 1/4 inch hole was drilled along the longitudinal axis to allow escape of gases during firing. A cutaway view of the crucible after firing is shown in figure 9(a).

In another crucible setup, the graphite block was made similar to the one described above except that the maximum diameter was 2-1/2 inches. This arrangement included a 5/8 inch graphite sleeve with an outside cylindrical diameter of 5 inches, being 7 inches long and rammed on both sides with the ramming mixture. A graphite plate 5/8 inch thick by 5 inches in diameter was positioned at the bottom of the induction coil, and covered with ramming material. The cutaway diagram is shown in figure 9(b).

3.1 (iv) Metallic Components

All the experiments were performed using electrolytic manganese (99.9%Mn) and Stelco bar stock (0.057%C, .01%P, .026%S, .33%Mn).

3.1 (v) Chemical Analyses

The manganese content was analysed according to the persulphate method[72]. Low carbon determinations were performed by a combustion technique, where the resulting CO_2 was passed through a solution of $Ba(OH)_2$, of known resistance. The change of resistance due to reaction with CO_2 was calibrated as a function of concentration. High carbon determinations were performed by measuring the volume of CO_2 released on combustion.

3.2 Experimental Technique

The majority of the experiments were carried out in the rammed crucibles, requiring a good technique for the production of a low porosity crucible wall. The evaporation experiments were performed on iron-manganese alloys, with the manganese content in the neighbourhood of 1%. Condensation and evaporation experiments were carried out to determine the rate of evaporation of iron. Temperature calibration curves were determined for both the Milletron and Latronics two-colour optical pyrometers.

3.2 (i) The Crucible

The Lumag 741 and Kaiser 102 crucibles were rammed dry, using a flat instrument to insure compact packing. The bottom of the induction coil was filled with approximately 2 inches of ramming material and then the graphite form, which was wrapped in several layers of paper, was centered in the coil and the crucible was rammed at increasing depths of 2 inches. The removable crucible assembly was then replaced in the vacuum chamber and pumping down was commenced, using the backing pump.

Four to 10 inches of argon (Hg) was bled into the tank to minimize the rate of degassing of the refractory material and the graphite core, so that the graphite core was not blown out by rapid degassing. The motor-generator set was turned on and the power was immediately brought up to the maximum (30 kilowatts) and the refractory was allowed to sinter under the white hot graphite core for thirty minutes. After the sintering, the chamber was brought to atmospheric pressure and the graphite core was removed and quenched in water. The removal of the core was facilitated by burning off the paper wrapping, which resulted in a loose fit of the core to the crucible.

The crucibles which were formed using a graphite sleeve were constructed in the same manner above, however, the graphite sleeve acted as a shield for the inner core and hence longer sintering times, up to 1 hour, were required before sintering was complete.

The rammed crucibles were far superior to the prefired crucibles, for the latter were very susceptible to thermal stresses, and many cracks formed, threatening the leakage of the melt onto the coil. The rammed crucibles presented no such problems, forming a shock resistant wall, relatively impervious to the melt. Of the two refractory powders used, the Kaisor 102 (magnesia) seemed to offer maximum stability and compactness.

3.2 (ii) Manganese Evaporation

The evaporation experiments were carried out, adhering to a set sequence of events. The vacuum chamber was allowed to degas to its maximum vacuum (1 micron Hg) at which time the motor-generator set was turned on, and power was fed into the coil. Maximum power was obtained by careful balancing of the condenser network and transformer taps, after the Curie temperature had been reached. As the temperature of the steel approached 1300°C, 4 inches (Hg) of argon was bled into the vacuum chamber, under which the melting of the steel occurred, minimizing the rapid degassing of the melt due to the carbon – oxygen reaction. This reaction causes violent degassing of the melt, which results in "spitting" of the melt into the vacuum chamber. The phenomenon of "spitting" was generally observed when the charge material was new Stelco steel which had not been previously vacuum treated — the chamber pressure was increased to 10 inches (Hg) of Argon in this case.

Having attained the molten condition, the chamber was again evacuated to approximately 1 micron Hg at a temperature slightly exceed- the melting point of iron (1539°C). The melt was held under vacuum for several minutes (up to 30 minutes) to ensure complete degassing. At this point in the procedure, the melt temperature was brought to the desired working temperature and held there by fine adjustment of the power input to the induction coil. Good temperature control was achieved in this manner and the temperature could be held at the desired level within $\pm$ 10°C.

For making manganese additions to the melt, the chamber pressure was raised to 4 inches (Hg) with Argon, to ensure that the lower melting, high vapour pressure manganese did not evaporate as it made contact with the melt surface. Manganese was added to form a 1% Mn – Fe liquid alloy. When the operating temperature was near that of the freezing point of iron, the manganese addition tended to freeze the surface, hence just prior to adding the manganese the power input was raised to 100%.

In making carbon additions to the melt, even at pressures of 25 inches (Hg) of Argon (absolute) the high oxygen content of the melts resulted in severe degassification and spitting. This difficulty was overcome by the use of natural gas as the controlled atmosphere. The methane present acted as a deoxidizer, so when the Carbon was added no violent CO evolution resulted. A careful pump down resulted in very little melt loss due to spitting. The manganese was added to the carbon saturated melts in the same manner as described above.

The manganese was allowed to mix thoroughly with the melt for five minutes and then the chamber was evacuated. The chamber was evacuated to approximately 300 microns Hg in 2 minutes, utilizing the backing pump, at which time the booster pumps were turned on and pumping continued for 2 more minutes (pressure approximately 10 microns Hg) and then sampling began.

Samples were taken from the combined temperature and sample port, seen in figure 4. The sample port, along with the addition port was equipped with a vacuum air lock to prevent contamination of the vacuum. The sample tube was dipped into the melt and a sample extracted, noting the time of contact. At the precise time of contact, the melt surface cooled up to 15°C and fine adjustment of the power input overcame this difficulty. Samples were taken every 1 to 2 minutes up to a maximum of eight times per run. The evaporation experiments, performed on the carbon saturated melts required longer sampling intervals (5 to 10 minutes) since the manganese activity is lowered by the carbon and also the rate of evaporation is lowered as the temperatures are decreased.

The quantity of charge varied between 2,200 gm to 2,800 gm as an attempt was made to conduct the evaporation experiments from a melt approximately 7 to 8 cm deep. Originally, the experiments were performed individually, that is after an experiment had been run, the charge was poured. This method was extended to performing a maximum of five runs on the same charge; after each run more manganese was added, and evaporation experiments were conducted at different temperatures. The melt was allowed to freeze in the crucible and cool under vacuum. The change in the height was determined by the height before and after the experiments were carried out. More charge material could then be added to bring the level up for the next series of experiments.

The number of runs performed on a crucible was limited only by the condensation of evaporated material on the upper part of the crucible, which gradually created a restriction to evaporation. The crucibles were changed generally every 10 runs; in the earlier stages of the experiments the crucibles were changed more frequently.

During the evaporation experiments, the evaporation products condensed on the water cooled chamber walls and also on the sight glasses, creating a particularly serious situation by condensing on the pyrometer sight glass causing low temperature readings. This occurrence was simply circumvented by the use of a rectangular sight glass (figure 6b) which could easily be moved to a clean surface to read the correct temperature. The sight glass rested on an "O" ring and was held in place by the vacuum.

The samples were then stripped of the silica holder, weighed to determine the drop in melt height due to loss of samples and sent to be analysed for manganese and carbon.

3.2 (iii) Condensation and Evaporation Experiments

The experimental setup for the condensation experiments is shown in figure 8. To perform the condensation experiments, it was necessary to remove the fitting for the Balzer thermal conductivity gauge. The pressure could be measured by the Stokes gauge which had been calibrated from the Balzer gauge.

The charge was melted as usual under 4 inches (Hg) of argon, and evacuated to maximum vacuum, then the temperature was brought to the desired value, and held steady for a few minutes. The condenser plate was then swung over the melt and lowered to within 1 cm of the melt surface. This distance was later increased to prevent the condenser plate from going too deep into the heating zone, as there was some evidence of copper melting. The condensation was allowed to continue for one minute, then the condenser plate was lifted out of the crucible and swung away. The weight gain due to iron condensation was determined by weighing the copper sheet before and after the experiment. The experiments were carried out mostly at high temperature to determine the applicability of the Knudsen rate equation at high temperatures. This method had the disadvantage that during the time of condensation, the temperature could not be measured and had to be assumed constant.

The evaporation experiments were performed by measuring the distance from the top of the furnace to the flat surface of the solidified melt, by means of an inside micrometer. The charge was then melted and evaporated at a constant temperature for times up to forty minutes. The melt was allowed to cool, and the decrease in melt height due to evaporation was measured, as before.

3.2 (iv) Temperature Calibration

The optical pyrometers were calibrated with a Pt – Pt13%Rh immersion thermocouple. The charge was melted, and kept steady at a temperature just above the melting point of iron while under vacuum. The thermocouple was immersed in the melt through the air lock used previously for sampling. The temperature was taken with the thermocouple junction approximately 1 inch below the melt surface. The power input was raised 5 to 10 percent creating a slow rise in temperature of approximately 5 to 10 degrees per minute, so as to minimize any chance of lag to the potentiometer. The potentiometer reading was recorded every 5 degrees up to 1750°C when the power was dropped and the potentiometer readings were again recorded. Temperature calibrations were performed over the range 1300°C to 1800°C.

CHAPTER IV

EXPERIMENTAL RESULTS

4.1 Introduction

In this section, the results of the investigations of the evaporation of manganese from liquid iron, under reduced pressures, are presented. The experiments are presented in three phases:

1) Evaporation from low carbon, liquid iron under the influence of induction stirring.
2) Evaporation from low carbon, shielded, iron melts.
3) Evaporation from high carbon liquid iron under the influence of induction stirring.

The results from the above experiments were used to calculate specific evaporation coefficients as a function of temperature. The specific evaporation coefficient data are presented graphically in an Arrenhius plot, to determine the activation energy or energies of the evaporation process, and to elucidate the kinetic nature of the process.

Evaporation and condensation experiments on pure iron are presented to illustrate the adherence of this system to the Knudsen model of maximum evaporation, particularly at high temperatures.

4.2 (i) Evaporation from Induction Stirred Melts (Low Carbon)

In these experiments, the manganese concentration of the melt was measured as a function of time. The experiments were carried out at various temperatures, ranging from a low of 1539°C (melting point of iron) to a maximum of 1810°C. The results are shown in table III and graphically in figures 10 to 24.

From the equation:

$$\ln C = \ln C_i - \frac{Ak}{V} t \qquad (65)$$

where $C \equiv$ Mn concentration in the bulk

$C_i \equiv$ Mn concentration at time zero

$k \equiv$ specific evaporation coefficient

$V \equiv$ volume of the melt

$A \equiv$ evaporation surface area

it is seen that the slopes of the lines obtained from figures 10 to 24 are equivalent to $- Ak/V$. The specific evaporation coefficient is then given by:

$$k = - \frac{V \text{ (slope)}}{A} \qquad (66)$$

The value V/A has units of length, and depends on the surface area available for evaporation, A, and may be regarded as the effective depth of the melt. The induction coil has a certain lifting power which tends to raise the surface of the melt in a circular arc (figure 25). This "stirring pressure" then tends to increase the evaporation surface A, and is given by:

$$p_s = \frac{57.7}{\sqrt{f}} \frac{P}{A^1} \qquad (67)$$

$p_s \equiv$ stirring pressure of the melt (lbs/in^2)

$f \equiv$ frequency of the power supply (cps)

$P \equiv$ power induced in the melt (k watt)

$A^1 \equiv$ cylindrical area of the melt

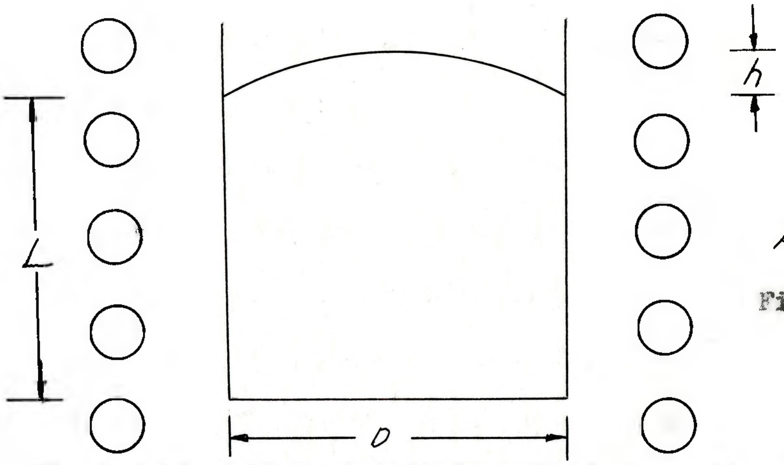

$A' = \pi D L$

Figure 25

The height which the melt is raised above the normal height, L, is h, shown in figure 25, and is given by:

$$h = p_s/\rho \qquad (68)$$

$\rho \equiv$ density of iron (lbs/in^3)

$h \equiv$ height in inches

or
$$h = \frac{221}{\sqrt{fA^1}} P \qquad (69)$$

A similar relationship has been determined by the Brown, Boveri Co.[59] for estimating the height h:

$$h = 31.6 \sqrt{\frac{\mu}{\rho f}} \; \frac{P}{A^1} \; \frac{1}{\gamma} \qquad (70)$$

where $\mu \equiv$ relative permeability

$\rho \equiv$ specific resistance

$\gamma \equiv$ specific gravity

From the calculated height, the surface area of the melt was determined from the expression:

$$A^1 = \frac{\pi}{4} (2h^2 + D^2) \qquad (71)$$

Utilizing equations (69) and (70) the melt height due to lifting was calculated to vary between 1.50 and 2.00 cm at minimum and maximum power used experimentally, giving rise to an area increase (over that of a plane surface) of 8.2% to 14.0%. Ward[10] experimentally measured the area increase by freezing the surface while the power was still applied (by the introduction of air) and measuring the surface area. In this manner, the experimental area increase was approximately 10%.

The area term used for the evaporation surface, A, was that of the plane surface increased by 10%.

The volume term employed was the mean volume, i.e. the average of the volume before the experiment plus that after the experiment, which is simply the starting volume less that required for sampling and that lost by evaporation.

Ward[10] sampled by pouring a portion of the melt into a chill mould, which resulted in a loss of 20% of the original charge. This loss was considered significant and corrections were made to the time intervals to allow for the decrease in height:

$$t_3^1 = (t_3 - t_2) \frac{M_o}{M_2 - M_3} \qquad (72)$$

where t_3^1 ≡ corrected time for the third sample

t_3 ≡ actual time of third sample

t_2 ≡ actual time of second sample

M_o ≡ initial weight

M_2 ≡ weight of bath after second sample

M_3 ≡ weight of bath after third sample

The sampling in the present work was performed with silica sample tubes which collected from 3 to 8 grams of the melt, resulting in a total bath reduction of not greater than 2%. The loss in this case was not considered significant, nor was that due to evaporation and hence no time corrections were considered necessary.

The slopes of the lines in figures 10 - 24 were determined by a weighted least squares (Appendix A), with the calculations being carried out by an I.B.M. 7040 computer. The results are listed in table IV, along with an estimation of the error. The graphical representation is shown in figure (26).

4.2 (ii) Evaporation from Shielded Melts (Low Carbon)

The arguments presented in the preceding section were applied to the calculations involved in the evaporation of manganese from shielded melts, however, the area term was decreased (5% over the plane surface area) due to the decrease in height caused by a decrease in power.

In these experiments, a carbon sleeve and bottom plate were inserted to shield the melt from the stirring effects of the induction field. A correlation relating the surface velocity of the melt, $\bar{U}$, to the height increase is given by Brown, Boveir Co.[59]

$$\bar{U} = 1/2\sqrt{2gh} \qquad (73)$$

where g ≡ acceleration due to gravity

From equation (73) it is seen that the height of the melt, h, is directly proportional to the power input, P, and hence the surface velocity is proportional to the power input to the 1/2 power.

Tocco Co.[62] has presented a relation from which the power absorbed in an electrical conductor may be calculated from the depth of penetration, Δ. In the first depth of penetration 81% of the power is absorbed, in the second depth of penetration 81% of the remaining power is absorbed etc. For non-magnetic materials, the relation for Δ is given by:

$$\Delta = 3.16\sqrt{\frac{\rho}{f}} \qquad (74)$$

Δ $\equiv$ depth of penetration into non magnetic species (inches)

ρ $\equiv$ resistivity of non magnetic species (microhm-inch)

f $\equiv$ frequency of power supply

The resistivity of the graphite(Union Carbide brand AUC) is much larger than that of iron (in the non-magnetic state), having a value of 307 microhm-inch compared to 40-50 microhm inch for iron. Thus, the depth of penetration into a graphite load is much higher than that for iron. For the 3000 cps system the first depth of penetration in graphite is 1.00 inch and in iron it is 0.40 inch. The graphite sleeve and plate used were 5/8 inch thick, resulting in an absorption of approximately 50% of the total power input.

The surface velocity, from equations (73) and (70) is proportional to $P^{1/2}$ and it is seen that the velocity is decreased approximately 30% by a carbon sleeve 5/8 inch thick.

Knuppel and Oeters[60] determined mean surface velocities of 20 cm/sec for unshielded melts at 1600 to 1700°C, whereas the theoretical values from equation (73) are 27 and 32 cm/sec respectively. The authors dropped pieces of carbon on the melt surface and timed their distance of travel. Machlin[48] observed surface velocities in the order of 10 cm/sec, utilizing the motion of particles floating on the top of the melt.

In the present experiments, pieces of carbon were dropped on the surface and attempts were made to measure the surface velocity by taking time exposures and measuring the size of the blur. This technique proved unsatisfactory and no experimental determination of the effect of the shield on the velocity of the melt was obtained.

The shielded experiments were carried out in the temperature range 1680°C to 1810°C. The results are listed in table IV (b) and illustrated graphically in figure 26.

4.2 (iii) Evaporation from High Carbon Iron Melts

To conduct evaporation experiments below the melting point of iron (1539°C) necessitated the use of high carbon melts, having a minimum liquidus temperature of 1130°C[61].

The calculations of section 4.2 (i) apply, with the exception in the low temperature calculations, the plane surface area of the melt was used to calculate the effective bath height since the power input was so low that the height increase due to induction pressure was negligible.

The specific evaporation coefficients calculated in this manner were all low, due to the effect of carbon on the activity of manganese. Schenck and Neumann[56] and Ohtani[57] have determined the effect of carbon on manganese at 1540°C, with major contradictions. Ward[63] gives preference to the data of Schenck and Neumann and the data employed in the calculations are according to Schenck and Neumann. The value f_{Mn}^{c} is called the interaction coefficient of carbon on manganese, and is a measure of the change of f_{Mn}^{Mn}, which is the effect of manganese on manganese in iron, caused by the addition of carbon to the manganese-iron system[64].

$$f_{Mn} = f_{Mn}^{c} \cdot f_{Mn}^{Mn} \qquad (75)$$

where $f_{Mn}^{Mn} = 1$ since iron-manganese is an ideal solution

$\therefore f_{Mn} = f_{Mn}^{c}$; f_{Mn} is the activity coefficient of Mn in Fe.

The interaction coefficient is related to the weight percent by the expression: $\log f_{Mn}^{c} = e_{Mn}^{c}[\%C]$ (76)

where e_{Mn}^{c} is the interaction parameter of C on Mn

The factor e_{Mn}^{c} is constant at infinite dilution. The approximation is made that e_{Mn}^{c} is constant at high carbon, and it is estimated from the data of Schenck and Neumann for Mn concentration of 1%. Lacking additional data at other temperatures, the following approximation is made:

$$e_1T_1 = e_2T_2 \qquad (77)$$

which states that as the temperature approaches infinity, the interaction parameter approaches zero.

Interaction parameters were calculated for the temperature used according to equation (77) and the manganese activity coefficient was calculated from equation (76). Thus,

$$k_{corr} = \frac{k}{f_{Mn}^{c}} \qquad (78)$$

$k_{corr} \equiv$ corrected evaporation coefficient

$k \equiv$ experimental evaporation coefficient

The results are shown in table IV C and in figure 26. The correction due to carbon in solution increases the evaporation coefficient by approximately a factor of three.

4.3 Activation Energy

The graph of the specific evaporation coefficient vs the reciprocal of the temperature represents the Arrenhius plot which predicts the slope being proportional to the activation energy for the process:

$$\text{Slope} = -\frac{Q}{2.303R} \qquad (79)$$

$R \equiv$ gas constant

As a first approximation, the slope in the low temperature region yields an activation energy in the neighbourhood of 45 k cal/g-mole, while that at higher temperature yields an activation energy of approximately 26 k cal/g mole. The shielded results yield an activation energy of approximately 17 k cal/g mole. The experimental results are, however, curvilenear and these straight line approximations are only estimates (section 5.2).

4.4 Specific Evaporation Constant for Diffusion

The specific evaporation constants of figure (26) represent the overall specific evaporation constants, including diffusion and evaporation. The relation between the overall, diffusive and evaporative evaporation constants is given by equation (62):

$$k = \frac{k_1 k_2}{k_1 + k_2} \qquad (80)$$

or

$$k_1 = \frac{k k_2}{k_2 - k} \qquad (81)$$

The specific evaporation constant due to evaporation alone, is derived from the Knudsen maximum rate equation, written in terms of weight percentages:

$$\frac{dC}{dt} = \frac{p^o}{\rho} \sqrt{\frac{M}{2\pi RT}} \quad C \qquad (82)$$

where ρ is the density of iron at temperature T[65]

or $\frac{dC}{dt} = k_2 C$

Thus

$$k_2 = \frac{p^o}{\rho} \sqrt{\frac{M}{2\pi RT}} \qquad (83)$$

where $p^o \equiv$ vapour pressure of manganese

The value for k_1 (specific evaporation constant for diffusion) can then be calculated. The k, k_1, k_2 values and the shielded specific evaporation constants are plotted in figure 27.

A plot of the ratio k_1/k_2 vs $1/T$ is presented in figure 28.

4.5 Evaporation and Condensation Experiments

4.5 (i) Condensation Experiments

The results of the condensation experiments, illustrating the agreement between the experimental maximum rate of evaporation and that predicted by Knudsen[1] are shown in table V (a). The Knudsen equation of section 2.1 (ii) was used in the form:

$$W = 0.05833\,(p^o - p)\sqrt{\frac{55.83}{T}} \qquad (84)$$

where $p \equiv$ the residual gas pressure

$p^{o} \equiv$ vapour pressure of iron

The vapour pressures used in the calculations were from the results reported by Kubashewski and Evans[66].

From table V (a) it is seen that the experimental maximum evaporation rate is less, in every case, than that predicted by Knudsen, over a temperature range from 1575°C to 1695°C. The values range from a low of 7% to a high of 62%, scattered randomly over the temperature range employed.

4.5 (ii) Evaporation Experiments

The results of the evaporation experiments are shown in table V (b) and it is seen that the experimental maximum rate of evaporation agrees with that predicted by the Knudsen maximum rate equation within 20%.

CHAPTER V

DISCUSSION OF THE RESULTS

5.1 Calculation of the Specific Evaporation Constant

The specific evaporation constants were calculated from the slopes of the lines shown in figures 10 – 24, assuming an error in the height measurement of ± 0.5 cm. This allowance of 0.5 cm arises from the fact that the evaporation surface area was assumed constant over the power input range, when in actual fact it is dependent on the power input (equation (76)). Errors are also introduced in the method of measuring the height decrease after evaporation.

In the low temperature range, the use of high carbon melts made it necessary to correct for the effect of carbon in decreasing the activity of manganese. The activity coefficients of manganese due to carbon were calculated from the data of Schenck and Neumann[56] within ± 0.05. The experimental error introduced in the calculations is caused by the assumptions of section 4.2 (iii).

The dependability of the Schenck and Neumann data is verified by the high carbon run No. 4/1. The uncorrected evaporation constant at 1625°C was determined to be 8.1 cm/sec which was corrected to 22.0 cm/sec from the Schenck and Neumann activity coefficient data. The specific evaporation constants for all the experiments are plotted in figure 26, and it is observed that the corrected specific evaporation constant is consistent with the specific evaporation constants evaluated from low carbon experiments. Utilization of the data of Ohtani[57] results in a corrected specific evaporation constant of 9 to 10 cm/sec which is definitely inconsistent with the experimental low carbon data. The use of the Ohtani data yields low specific evaporation constants since these data show that carbon has very little effect on manganese in iron, at dilute manganese concentrations.

5.2 The Activation Energy for the Process

The experimental data plotted in figure 26, may be compared with the predicted data of Knudsen (equation (82)). From the analysis presented in chapter I it is obvious that the Knudsen prediction represents the maximum possible rate of evaporation and therefore predicts the maximum possible specific evaporation constant. Figure 26 shows that at low temperatures, the experimental specific evaporation constant approaches that predicted by Knudsen. The Knudsen derivation is based on an evaporation control mechanism and this means that in the low temperature range, the evaporation of manganese from liquid iron is controlled by the desorption of manganese from the surface (equation (57)).

The vapour pressure data used to calculate the Knudsen maximum evaporation constant were calculated from the data of Kubashewski and Evans[66], which are reported to be within ± 20%. From figure 26 it is seen that within the range of experimental error the results might be explained entirely by evaporation control at approximately 1320°C and lower.

If evaporation control predominated, the experimental curve would adhere quite closely to the Knudsen curve, over the whole temperature range. However, at temperatures $>1320°C$ it is seen that the experimentally determined specific evaporation constant becomes progressively less than that predicted by Knudsen. The result is a gradual increase in the slope of a tangent to the curve, (i.e. the slope becomes less negative) varying from a maximum at low temperatures to a minimum at higher temperatures. The increase in the slope indicates a transition from evaporation control to diffusion control.

The slope of the Knudsen line yields an activation energy of 57.2 kcal/g mole, which is the activation energy required for the evaporation of manganese from iron. The slope of the tangent to the experimental curve at $6.30 \times 10^{-4}\ {}^{o}K^{-1}$ yields an activation energy of approximately 45 kcal/g mole and the tangent to the curve at higher temperatures ($5.00 \times 10^{-4}\ {}^{o}K^{-1}$) is equivalent to an activation energy of 26 k cal/g mole. The activation energy for the process studied thus tends to the activation energy for Mn ($Q = 57$ kcal/g mole) evaporation at lower temperatures and to the activation energy for Mn diffusion ($Q = 3$ kcal/g mole)* at higher temperatures, i.e. in the temperature range considered, the process of Mn evaporation from liquid iron under reduced pressures proceeds from largely evaporation control at low temperatures to largely diffusion control at high temperatures.

It is observed in figure 26 that at $1/T = 5.81 \times 10^{-4}\ {}^{o}K^{-1}$ the maximum specific evaporation constant according to the Knudsen relationship, is greater than that determined experimentally by a factor of 2. Thus, at this temperature the predicted curves for evaporation control and for diffusion control must intersect, the latter being simply a line whose slope is calculated from the activation energy for the diffusion of Mn in Fe.

* see page 65

Smithells[73] reports an energy of activation for diffusion of Mn in Fe as approximately 6 kcal/g mole. However, the model of Machlin[48] (equation(53)) predicts for diffusion control that the specific evaporation constant is proportional to $D_{Mn}^{1/2}$ (where D_{Mn} is the diffusivity of Mn in Fe) and since:

$$D = Do \ \exp - E/RT \qquad (85)$$

where E is the activation energy for diffusion

$$D^{1/2} = Do^{1/2} \exp - E/2RT \qquad (86)$$

It is apparent that the specific evaporation constant for diffusion control is related to E/2 and hence the activation energy from the Arrenhius plot would be 6/2 = 3 kcal/g mole.

Figure 27 represents the Arrenhius plot combining all the possible specific evaporation constants. Theoretically one would expect the experimental curve to asymptotically approach the limiting cases for evaporation and diffusion control at low and high temperatures respectively. However, it is observed that in the low temperature range this holds true, but in the high temperature range the experimental curve approaches the limiting diffusion curve, and crosses over. This phenomenon is not too startling if one analyses the conditions for evaporation at high temperatures in an induction heated furnace.

5.3 The Effect of Stirring on the Specific Evaporation Constant

The apparent inconsistency of the experimental data with that predicted can readily be interpreted by examining the effects of stirring on mass transfer rates governed entirely or partly by diffusional processes. In induction heated processes, higher temperatures are achieved by an increased power input, which is related directly to the degree of stirring in the melt (equation (70) and (73)), thus at elevated temperatures the melt experiences greater stirring effects than at lower temperatures. An increase in the stirring rate has the effect of decreasing the thickness of the diffusion boundary layer, resulting in larger evaporation rates than would normally be expected. The maximum slope in the high temperature range of figure 26 is equivalent to an activation energy of 26 kcal/g mole which indicates that diffusion alone is not the rate limiting step. If the experiments could be carried out over the entire temperature range at the stirring conditions present in the low temperature region, the high temperature results would probably behave as expected and asymptotically approach the theoretical diffusion control curve.

Knuppel and Oeters[60] studied the effect of induction stirring on the rate of absorption of N_2 into an iron melt. They utilized a magnesia crucible containing 3.6 kg of molten iron, with a refractory stirring rod connected to a variable speed motor. At 1600°C they measured the mass transfer coefficient for the absorption of N_2, with stirring speeds of 120 r.p.m. and 300 r.p.m., to be 4.5 cm/sec and 15.5 cm/sec respectively. In another experiment on the degassing of N_2 from liquid iron at 1600°C, they measured the mass transfer coefficient for nitrogen desorption under vacuum to be 14.5 cm/sec. They conclude that in diffusion controlled processes such as multi-component evaporation, the stirring speed is directly proportional to the rate of evaporation, and in particular, the degassing of nitrogen from liquid iron (at reduced pressures) which is induction stirred, is equivalent to stirring a non-induction influenced melt at 300 r.p.m.

In some experiments (figure 26), the degree of stirring was decreased by the insertion of a graphite shield (section 3.1 (iii)) and the rate of evaporation of Mn was reduced considerably. The experiments were performed in the high temperature region where it was considered that the effects of stirring would be most important. In the low temperature experiments on unshielded melts, observations of the melt surface did not show any stirring effects, and particles floating on the surface, at times, did not move. From these observations it was concluded that shielded experiments were unnecessary in the low temperature region. Also, in the low temperature region it has been shown that manganese evaporation tends to evaporation control ($Cs/Cm \rightarrow 1$) and thus the rate of evaporation would be largely independend of the stirring rate.

The decrease in the surface agitation due to the insertion of the graphite shield was readily noticeable. The magnitude of the surface velocity has been predicted to decrease by approximately 30% for the conditions studied (section 4.2 (ii)). From figure 26, the corresponding decrease in the specific evaporation constant varies from 37% at 5.15×10^{-4} $^{o}K^{-1}$ to 42% at 4.9×10^{-4} $^{o}K^{-1}$, which indicates a strong relationship between surface velocity and the specific evaporation constant. The calculations leading to the prediction of a 30% decrease in surface velocity made no provision for the effect of the absorption power of the graphite plate and hence the 30% value is probably a low estimate of the velocity decrease.

Although the experimental results for the shielded experiments are undoubtedly curvilinear in nature, they have been approximated to a straight line equivalent to a mean activation energy, over this temperature range, of 17 kcal/g mole. This observation illustrates a trend towards the activation energy for diffusional transfer due to the decrease in stirring. The activation energy for the process in the high temperature range would be expected to approach 3 kcal/g mole (section 5.2) as the degree of induction stirring was decreased to zero. It was mentioned previously (section 4.2 (ii)) that 81% of the power input would be absorbed in a graphite sleeve 1.00 inch thick, but the use of such thick shields was not possible in the present experimental setup because of the limited space in the heating zone of the induction coil.

Figure 26 shows that the experimental curve for specific evaporation constants for shielded experiments approaches the theoretical diffusion control line at temperatures greater than 1800°C, illustrating that complete diffusion control is being approached. As the temperature is decreased, one would expect the high stirring specific evaporation constant curve to coincide with the low stirring specific evaporation constant curve at a temperature where stirring effects are negligible, as shown in figure 26.

The specific evaporation coefficients determined by Ward[10], for the same Mn-Fe system (figure 26), are slightly less than those observed in the present investigation. The slight discrepancies could be interpreted by differences in the stirring characteristics of the two systems, as Ward's experiments were performed on considerably larger melts (10 kgm vs 2-3 kgm) which could result in decreased stirring rates due to an increase of the drag at the crucible-melt interface.

Figure 26 shows that the present data are not inconsistent with the prediction of Machlin[48], however, the Machlin model assumes complete diffusion control and Machlin states that any agreement with experimental results, within a factor of 2 or 3, is sufficient to illustrate agreement with the theory.

5.4 The Controlling Process

The plot of figure 26 should undoubtedly be curvilinear, approaching the two limiting cases of diffusion and evaporation control at the outer limits of the temperature range employed (1320°C to 1810°C). There is no fixed temperature at which one process suddenly supercedes the other, but there is a gradual transition from predominately evaporation control at low temperatures to predominately diffusion control at high temperatures. The actual plot of figure 26 has, however, been drawn with considerable linear sections at both the upper and lower ends as the experimental data do not justify any significant curvature.

In a similar analysis, Beeton[74] investigated the reduction of iron ore with hydrogen and concluded there was a discontinuity in the Arrenhius plot of mass transfer coefficient vs $1/T^{o}K^{-1}$, indicating that diffusion of hydrogen into the material and water vapour out suddenly takes precedence over the chemical reaction of hydrogen with the ore. This phenomenon is considered unlikely in the present study as the experimental results verify the curvilinear nature of the plot.

From equation (62) of chapter III it is seen that the specific evaporation constant for diffusion control, k_1, can be written in terms of the maximum specific evaporation constant (Knudsen's prediction),

k_2, and the overall specific evaporation constant, k:

$$k_1 = k\, k_2 / (k_2 - k) \qquad (87)$$

The values for k_1 were calculated and plotted with the other specific evaporation constants (k, k_2 and $k_{shielded}$) in figure 27. The resulting straight line, yields a slope equivalent to approximately 17 kcal/g mole. This figure obviously reflects the effect of stirring on the specific evaporation constant, producing a value 6 times that normally expected.

The ratio of the specific evaporation constant (overall), k , to that for evaporation, k_2, is plotted vs $1/T\,^{\circ}K^{-1}$ in figure 28, and in the limits (section 2.11) $k_1 >> k_2$ and $k_2 >> k_1$, represents the limits $Cs/C_o \longrightarrow 1$ and $Cs/C_o \longrightarrow 0$ respectively. Figure 28 clearly illustrates that at low temperatures, $k\ /k_2$ approaches unity, i.e. the surface concentration approaches the melt concentration and evaporation from the surface is rate controlling. It is also seen that at higher temperatures $k\ /k_2 \longrightarrow 0$, that is the surface concentration is much less than the bulk concentration and diffusion control predominates.

5.5 High Temperature Evaporation Rates

The decrease in the specific evaporation coefficient with increasing temperatures was shown to be unrelated to the reflection of molecules back into the melt due to high vapor densities in the gas phase adjacent to the liquid interface. The condensation experiments were inconclusive since the condensation plate could not be held close to the melt surface, due to melting, and at larger distances the evaporating area is considerably less than the condensation area, due to the spherical cap shape of the melt surface.

The evaporation experiments were conclusive in illustrating that the maximum evaporation rates predicted by Knudsen were verified at both low and high temperatures. The experimental results were within ± 20% of those predicted by Knudsen which were calculated using vapour pressures quoted within ± 20%. In addition, the decrease in the experimental specific evaporation constant from the maximum commences at temperatures below the melting point of iron and it is extremely unlikely that reflection would occur at these low vapour pressures.

5.6 Validity of the Evaporation Model

The original model, postulating that the controlling process in the evaporation of solute atoms from a solvent is either diffusion controlled in the liquid interface or surface controlled by the desorption of atoms from the surface, in the limiting cases, is apparently a good one. From the results it is observed that the model illustrates quite well the transition from evaporation control to diffusion control. However, this model, it has been shown, must be interpreted in terms of the stirring conditions in the melt, when applied to a system whose stirring conditions are not constant. A reasonable explanation of these stirring effects can be obtained by considering the effect of the stirring on the frictionless boundary layer.

Sehgal and Mitchell[75], in studying the evaporation of sulphur from liquid iron under vacuum utilize a similar model from which they predict that the loss of sulphur at reduced pressures is controlled either by diffusion in the liquid boundary or by desorption from the surface. They show first order kinetics for the reaction and suggest that the rate of evaporation of sulphur under vacuum is controlled by the rate of desorption of atomic sulphur from the liquid-gas interface. Their experiments were performed at 1585°C ± 5°C and no attempt was made to determine if a transition to diffusion control occurred at higher temperatures.

CONCLUSIONS

1) The evaporation of manganese from liquid iron at reduced pressures and at steelmaking temperatures (1550 - 1600°C) is governed by both diffusion in a liquid boundary and by desorption from the surface.

2) In the low temperature range (less than 1435°C) the evaporation of manganese from liquid iron, under vacuum, is largely a surface phenomenon, i.e. evaporation is controlling the process.

3) In the high temperature range (greater than 1435°C), the process reverts largely to control in the liquid boundary layer, i.e. diffusion control predominates.

4) In the region where diffusion control predominates, the rate of loss of solute atoms from a solvent, under vacuum, is affected to a great extent by the turbulence of the melt. The effect is an increase in the specific evaporation coefficient over that expected when no stirring is present, resulting in an increase in the importance of the desorption from the liquid surface.

5) The rate of evaporation of iron, under vacuum, adheres to the prediction of the Knudsen maximum rate equation. This illustrates that over the temperature range 1600°C to 1810°C the evaporation coefficient for liquid iron is unity, or iron exhibits no constraints in the liquid phase as expected.

6) The rate of evaporation of manganese closely approaches the

maximum rate predicted by Knudsen at temperatures close to 1300°C, indicating that the evaporation coefficient for manganese in iron is unity. The apparent decrease in the evaporation coefficient at higher temperatures is probably due to decrease in the surface concentration from that of the bulk, rather than due to constraints in the liquid phase.

7) The data of Schenck and Neumann[56] for activity coefficients of manganese due to the presence of carbon in iron are more consistent in these experiments than those presented by Ohtani[57].

The Schenck and Neumann data predict an activity coefficient for Mn in high carbon Fe in the neighbourhood of 0.35, whereas the Ohtani data predicts an activity coefficient of 0.9 to 1.0.

TABLE I

THE EVAPORATION COEFFICIENT AND FREE ANGLE RATIO FOR VARIOUS POLAR COMPOUNDS

	Compound	α_v	δ
(I)	Benzene	0.9	0.85
	Chloroform	0.16	0.54
	Ethanol	0.020	0.02
		0.024	0.02
	Methanol	0.045	0.05
	Glycerol	0.05	0.05
	Water	0.04	0.04
		0.02	0.04
(II)	Glycerol	1	0.05
	Water	0.4	0.04
(III)	2 – ethyl – hexyl phthalate	1	–
	2 – ethyl – hexyl – sebacate	1	–
	Myristic Acid	1	–
	Lauric Acid	1	–
	Hexadecanol	1	–
	Capric Acid	0.49	–
	Tetradecanol	0.68	–
	Dodecanol	0.22	–
	N – di – butyl phthalate	1	–
	Tri – heptymethane	1	–
	Tri decyl methane	1	–
	N – hexadecane	1	–
	N – octadecane	1	–
	N – heptadecane	1	–

TABLE II

CHEMICAL COMPOSITION OF THE REFRACTORIES

Percent	Lumag 741	Zircoa	Kaiser 102
Al_2O_3	25.2	0.4	0.3
MgO	66.9	0.02	96.0
SiO_2	5.8	34.2	1.5
CaO	1.3	0.03	1.3
TiO_2	0.3	0.2	-
Fe_2O_3	0.2		0.4
ZrO_2	-	65.0	-
Cr_2O_3	-	-	0.3
Misc.	0.30	0.15	0.2

TABLE III (a)

TIME - CONCENTRATION MEASUREMENT (LOW CARBON)

Run No.	Time (Min)	Manganese Concentration (Wt.Percent)	Average Carbon Content (Wt.Percent)	Run No.	Time (Min)	Manganese Concentration (Wt.Percent)	Average Carbon Content (Wt.Percent
2			0.003	9	0	0.20	0.005
	6.00	0.15			1.50	0.16	
	11.00	0.09			4.00	0.08	
	18.50	0.05			5.50	0.06	
	25.00	0.03			8.50	0.03	
3	0	0.11	0.003	10	0	0.18	0.003
	4.00	0.08			1.50	0.13	
	8.00	0.06			2.50	0.10	
	13.00	0.04			4.00	0.08	
	16.00	0.03			5.00	0.05	
	20.00	0.02			7.50	0.03	
5	0	0.45	0.003	11	0	0.44	0.002
	6.00	0.26			1.20	0.33	
	8.00	0.19			3.00	0.22	
	11.00	0.14			4.25	0.19	
	16.00	0.08			6.33	0.14	
	19.00	0.07			9.20	0.07	
	20.00	0.06		12	0	0.61	0.002
8	0	1.08	0.002		1.33	0.51	
	2.30	0.77			2.66	0.41	
	5.00	0.62			3.92	0.33	
	10.40	0.35			5.17	0.28	

TABLE III (a)
(cont'd)

Run No.	Time (min)	Manganese Concentration (Wt.Percent)	Average Carbon Content (Wt.Percent)
13	1.50	0.51	0.006
	3.00	0.37	
	4.50	0.32	
	5.83	0.27	
	7.50	0.22	
	8.83	0.19	
14	0.33	1.12	0.003
	1.75	0.87	
	3.58	0.65	
	5.08	0.50	
	6.00	0.44	
15	0	0.63	0.002
	1.42	0.40	
	2.92	0.28	
	4.33	0.22	
	6.08	0.17	
	7.00	0.13	
17	2.08	0.61	0.004
	4.17	0.42	
	5.25	0.38	
	6.50	0.33	
	7.67	0.30	
18	0	0.63	0.004
	1.17	0.48	
	2.50	0.35	
	3.92	0.28	
	5.00	0.24	
	6.08	0.19	
20	0	0.54	-
	1.42	0.39	
	2.83	0.30	
	4.50	0.22	
	6.00	0.17	
	7.67	0.13	
	9.33	0.105	
	10.58	0.08	
21	0	0.24	-
	1.17	0.17	
	2.33	0.12	
	3.33	0.10	
	4.50	0.075	
	5.82	0.065	
22	0	0.40	-
	1.00	0.35	

TABLE III (a)
(cont'd)

Run No.	Time (min)	Manganese Concentration (Wt.Percent)	Average Carbon Content (Wt.Percent)
22 cont.	2.25	0.26	
	3.42	0.19	
	4.92	0.15	
23	0	0.75	–
	1.20	0.62	
	2.48	0.52	
	3.80	0.42	
	5.22	0.36	
	6.55	0.28	
	8.00	0.25	
24	0	0.70	–
	1.37	0.58	
	2.67	0.37	
	4.00	0.29	
	5.23	0.23	
	6.67	0.175	
25	0	0.71	–
	1.22	0.60	
	4.12	0.39	
	5.48	0.30	
	7.17	0.245	
	8.72	0.19	
26	0	0.80	–
	1.23	0.55	
	2.62	0.37	
	3.73	0.285	
	4.93	0.215	
	5.92	0.17	
27	0	1.09	–
	1.32	0.85	
	2.38	0.70	
	3.67	0.57	
	5.27	0.41	
	6.68	0.33	
	8.38	0.22	
28	0	0.49	0.002
	1.57	0.41	
	3.28	0.33	
	4.80	0.29	
	6.17	0.24	
	7.43	0.23	
	8.63	0.21	
	9.83	0.18	
29	0	0.52	0.003

TABLE III (a)
(cont'd)

Run No.	Time (min)	Manganese Concentration (Wt.Percent)	Average Carbon Content (Wt.Percent)
29 cont.	1.38	0.35	
	2.85	0.26	
	4.22	0.22	
	5.53	0.17	
	6.53	0.14	
	7.75	0.11	
	9.00	0.11	
30	0	0.40	0.004
	1.20	0.30	
	2.62	0.22	
	3.62	0.18	
	4.82	0.16	
	6.03	0.11	
	7.17	0.10	
	8.30	0.09	
31	0	0.28	0.003
	1.60	0.18	
	2.78	0.13	
	3.58	0.12	
	4.58	0.10	
	5.62	0.08	
	6.62	0.07	
31 cont.	7.88	0.06	
32	0	0.20	0.002
	1.13	0.14	
	2.30	0.12	
	3.28	0.09	
	4.57	0.07	
	5.90	0.06	
	7.25	0.05	
	8		
33	0	0.74	0.003
	1.47	0.55	
	2.70	0.50	
	4.13	0.43	
	5.53	0.33	
	6.70	0.29	
	8.18	0.24	
34	0	0.79	0.004
	1.43	0.60	
	2.70	0.56	
	4.05	0.48	
	5.48	0.41	
	6.72	0.37	

TABLE III (a)
(cont'd)

Run No.	Time (min)	Manganese Concentration (Wt.Percent)	Average Carbon Content (Wt.Percent)
34 cont.	8.00	0.32	
	9.18	0.29	
35	0	1.16	0.003
	1.50	0.99	
	2.82	0.97	
	4.13	0.82	
	5.42	0.71	
	6.67	0.65	
	7.92	0.60	
	9.07	0.55	
36	0	0.87	0.002
	1.37	0.63	
	2.65	0.51	
	3.97	0.39	
	5.20	0.35	
	6.62	0.29	
	7.88	0.23	
	9.17	0.19	
37	0	0.81	0.002
	1.13	0.76	
	2.43	0.45	
	3.60	0.43	
37 cont.	5.00	0.35	
	6.08	0.28	
	7.03	0.24	
	8.12	0.23	
	10.23	0.17	
38	0	0.85	0.003
	1.23	0.72	
	2.35	0.67	
	3.63	0.53	
	4.92	0.48	
	6.03	0.44	
	7.42	0.34	
39	0	0.93	0.004
	1.13	0.82	
	2.20	0.76	
	3.42	0.70	
	4.87	0.64	
	5.88	0.60	
	6.92	0.60	
40	0	1.16	0.003
	1.00	1.01	
	2.13	0.83	

TABLE III (a)
(cont'd)

Run No.	Time (min)	Manganese Concentration (Wt.Percent)	Average Carbon Content (Wt.Percent)
40 cont.	3.13	0.73	
	4.15	0.69	
	5.25	0.61	
	6.45	0.55	
41	0	1.00	0.002
	1.42	0.82	
	2.62	0.67	
	6.55	0.45	
	7.70	0.39	
	8.80	0.37	
	9.82	0.35	
42	0	0.58	0.003
	1.20	0.41	
	2.50	0.32	
	3.87	0.24	
	5.12	0.18	
	6.17	0.17	
	7.32	0.15	
	8.28	0.13	
44	0	0.67	0.005
	1.27	0.54	
	2.37	0.44	
44 cont.	3.62	0.34	
	4.58	0.32	
	5.63	0.26	
	6.63	0.21	
	7.58	0.18	
45	0	1.04	0.004
	1.15	0.91	
	2.40	0.77	
	3.52	0.65	
	4.58	0.59	
	5.70	0.55	
	6.75	0.49	
	7.75	0.47	
46	0	0.30	0.002
	0.82	0.26	
	2.25	0.15	
	3.00	0.12	
	5.10	0.08	
	6.92	0.04	
47	0	1.14	0.003
	1.55	1.02	
	2.72	0.98	

TABLE III (a)
(cont'd)

Run No.	Time (min)	Manganese Concentration (Wt.Percent)	Average Carbon Content (Wt.Percent)	Run No.	Time (min)	Manganese Concentration (Wt.Percent)	Average Carbon Content (Wt.Percent)
47 cont.	3.87	0.76		1/A	0	0.35	.002
	5.08	0.70			1.45	0.30	
	6.30	0.66			2.70	0.26	
	7.35	0.61			3.67	0.24	
	8.53	0.55			4.88	0.22	
49	0	1.74	0.002		6.15	0.20	
	3.47	0.94		2/A	0	1.22	.002
	4.90	0.65			1.13	1.00	
	8.35	0.42			2.30	0.93	
50	0	2.26	0.004		3.58	0.81	
	1.12	1.90			4.75	0.73	
	2.35	1.28			6.17	0.63	
	3.63	0.97		5/A	0	1.30	.003
	4.83	0.70			1.21	1.18	
	6.00	0.54			2.72	1.00	
					4.07	0.87	
					5.22	0.76	

TABLE III (b)

CONCENTRATION MEASUREMENTS

(Shielded Runs)

Run No.	Time (min)	Manganese Concentration (Wt.Percent)	Average Carbon Content (Wt.Percent)
51	0	1.50	0.005
	1.38	1.34	
	2.40	1.22	
	3.35	1.10	
	4.80	0.95	
	5.78	0.83	
	6.70	0.77	
52	0	1.86	0.003
	3.65	1.30	
	4.80	1.16	
	6.88	1.02	
53	0	0.50	0.003
	1.05	0.45	
	2.03	0.41	
	3.11	0.36	
	4.10	0.34	
	5.11	0.29	
	6.17	0.29	
54	0	1.20	0.005
	3.87	0.72	
	4.78	0.67	
	5.77	0.59	
	6.82	0.50	
56	0	1.00	0.004
	0.97	0.88	
	1.87	0.65	
	3.12	0.52	
	4.00	0.45	
	5.02	0.38	
	6.67	0.29	
57	0	2.04	0.003
	1.10	1.62	
	2.00	1.44	
	3.07	1.22	
	4.03	1.08	
	5.02	0.90	
	6.13	0.74	

TABLE III (c)

CONCENTRATION MEASUREMENTS

(High Carbon Runs)

Run No.	Time (min)	Manganese Concentration (Wt.Percent)	Average Carbon Content (Wt.Percent)
1f	0	2.34	4.37
	2.33	2.22	
	4.17	2.12	
	6.10	2.10	
	8.33	1.96	
1g	0	3.84	4.56
	1.75	3.70	
	3.73	3.36	
	6.28	3.32	
	8.53	3.20	
3/1	0	2.59	5.15
	3.20	2.42	
	6.00	2.22	
	11.8	2.11	
	16.7	2.07	
4/1	5.5	0.68	5.36
	10.5	0.50	
	15.0	0.45	
	20.0	0.32	
	25.5	0.25	
	30.5	0.19	
7/1	0	2.49	4.81
	10.0	2.26	
	17.0	1.99	
	24.0	1.80	
	31.5	1.58	
	39.5	1.48	
8/1	0	1.35	4.74
	8.0	1.29	
	13.5	1.26	
	22.0	1.14	
	30.0	1.12	
	40.0	1.10	
9/1	0	2.43	4.60
	8.5	2.30	
	16.5	2.20	
	24.5	2.06	
	33.0	1.92	
	41.0	1.86	

TABLE IV (a)

SPECIFIC EVAPORATION CONSTANT

Run No.	Slope (min^{-1})	Effective Bath Height (cm)	Evaporation Constant (cm/sec) X10^3	Temperature (^{o}C)	1/T ($^{o}K^{-1}$) X10^4
2	− 0.0771	7.86	10.1 ± 1.1	1530	5.55
3	− 0.0800	7.17	9.6 ± 0.8	1535	5.53
5	− 0.1022	7.78	13.3 ± 1.3	1588	5.38
8	− 0.1191	10.40	20.6 ± 1.9	1615	5.30
9	− 0.1776	6.36	18.8 ± 3.1	1660	5.17
10	− 0.1968	5.88	19.3 ± 2.2	1635	5.24
11	− 0.1955	8.17	26.6 ± 2.3	1730	4.99
12	− 0.1533	6.87	17.6 ± 1.5	1675	5.13
13	− 0.1379	7.91	18.2 ± 2.0	1600	5.34
14	− 0.1115	7.95	14.8 ± 2.4	1585	5.38
15	− 0.2268	7.63	28.8 ± 2.8	1730	4.99
17	− 0.1275	7.67	16.3 ± 2.4	1580	5.40
18	− 0.1885	7.35	23.1 ± 2.4	1665	5.16
20	− 0.1719	8.66	24.8 ± 2.1	1660	5.17
21	− 0.2528	8.35	35.2 ± 3.5	1770	4.89
22	− 0.2066	7.90	27.2 ± 2.7	1725	5.01
23	− 0.1518	7.69	19.5 ± 1.9	1660	5.17

TABLE IV (a)
(cont'd)

Run No.	Slope (min^{-1})	Effective Bath Height (cm)	Evaporation Constant (cm/sec) $\times 10^3$	Temperature (°C)	$1/T$ $(°K^{-1}) \times 10^4$
24	− 0.2174	7.19	26.1 ± 2.5	1700	5.07
25	− 0.1513	6.83	17.2 ± 1.4	1585	5.38
26	− 0.2730	6.68	30.4 ± 2.7	1735	4.98
27	− 0.1840	6.50	19.9 ± 2.0	1700	5.07
28	− 0.1030	9.15	15.7 ± 0.9	1610	5.31
29	− 0.1922	8.82	28.3 ± 2.2	1680	5.12
30	− 0.1962	8.32	27.2 ± 2.2	1710	5.04
31	− 0.1841	7.75	23.8 ± 2.1	1730	4.99
32	− 0.1935	7.45	24.1 ± 2.4	1740	4.97
33	− 0.1367	7.31	16.7 ± 1.5	1570	5.43
34	− 0.1097	7.14	13.1 ± 1.1	1560	5.46
35	− 0.0839	6.84	9.6 ± 0.9	1530	5.53
36	− 0.1715	6.56	18.8 ± 1.7	1600	5.34
37	− 0.1680	9.70	27.2 ± 2.1	1670	5.15
38	− 0.1167	9.38	18.2 ± 1.9	1625	5.27
39	− 0.0669	9.05	10.1 ± 0.9	1560	5.46
40	− 0.1170	8.73	17.0 ± 1.6	1595	5.35

TABLE IV (a)
(cont'd)

Run No.	Slope (min^{-1})	Effective Bath Height (cm)	Evaporation Constant (cm/sec) X10^{3}	Temperature ($^{\circ}$C)	1/T ($^{\circ}$K^{-1}) X10^{4}
41	− 0.1139	8.28	15.7 ± 1.4	1600	5.34
42	− 0.1985	8.11	26.8 ± 2.4	1710	5.04
44	− 0.1720	7.90	22.7 ± 1.7	1665	5.16
45	− 0.1107	7.82	14.4 ± 1.7	1590	5.37
46	− 0.2947	7.61	37.4 ± 4.4	1810	4.80
47	− 0.0896	7.51	11.2 ± 1.1	1560	5.46
49	− 0.1596	6.56	17.5 ± 3.3	1645	5.21
50	− 0.2292	6.17	23.6 ± 2.8	1635	5.24
1/A	− 0.0948	7.37	11.6 ± 1.5	1580	5.40
2/A	− 0.1050	7.01	12.3 ± 1.2	1555	5.47
5/A	− 0.1021	6.43	10.9 ± 1.0	1565	5.44

TABLE IV (b)

SPECIFIC EVAPORATION COEFFICIENT

(Shielded Runs)

Run No.	Slope (min^{-1})	Effective Bath Height (cm)	Evaporation Constant (cm/sec) $X10^3$	Temperature $(^{\circ}C)$	$1/T\ X10^4$ $(^{\circ}K)$
51	− 0.1001	9.80	16.4 ± 2.0	1755	4.93
52	− 0.0941	9.10	14.3 ± 1.5	1720	5.02
53	− 0.0954	8.57	13.6 ± 1.3	1680	5.12
54	− 0.1208	8.12	16.3 ± 1.7	1705	5.06
56	− 0.1692	6.70	18.9 ± 2.3	1800	4.82
57	− 0.1610	6.37	17.1 ± 1.6	1725	5.01

TABLE IV (c)

SPECIFIC EVAPORATION CONSTANT

(High Carbon)

Run No.	Slope (min^{-1})	Effective Bath Height (cm)	Activity Coefficient of Mn	Corrected Evaporation Constant (cm/sec) X10^{3}	Temperature (°C)	1/T°K X10^{4}
1f	0.0170	6.02	0.402	4.3 ± 1.30	1375	6.07
1g	0.0169	5.82	0.375	4.37 ± 1.41	1335	6.22
3/1	0.0139	9.64	0.354	6.29 ± 1.40	1435	5.86
4/1	0.0497	9.82	0.370	22.00 ± 4.30	1625	5.27
7/1	0.0139	9.30	0.367	5.88 ± 1.01	1390	6.02
8/1	0.00586	9.17	0.366	2.38 ± 1.00	1350	6.16
9/1	0.00678	8.80	0.367	2.73 ± 0.93	1310	6.32

TABLE V

RATE OF EVAPORATION OF IRON

Temperature $^{\circ}C$	Weight Gain or Loss (gm)	Time for condensation or evaporation (min)	Experimental Evaporation Rate ($gm/cm^2/sec$) $X10^{-4}$	Maximum Evaporation Rate ($gm/cm^2/sec$) $X10^{-4}$	Percent Error
(a) CONDENSATION EXPERIMENTS					
1575	.303	1	1.11	2.92	- 62
1630	1.146	1	4.19	5.58	- 25
1680	2.286	1	8.36	9.84	- 15
1690	2.45	1	8.97	10.94	- 18
1695	2.93	1	10.73	11.56	- 7.2
(b) EVAPORATION EXPERIMENTS					
1645	57.98	40	5.30	6.62	- 20
1690	62.08	25	9.08	10.94	- 17
1705	106.18	25	15.53	12.94	+ 20
1750	97.26	15	23.71	20.62	+ 15

TABLE VI

TABLE OF ERRORS

ITEM	DESCRIPTION	UNCERTAINTY (Percent)
V/A	Effective bath height	± 6
C	Manganese concentration	± 5
T	Temperature measurement	± 0.7
γ	Activity coefficient of Mn in high carbon Fe from the data of Schenck and Neumann	± 15
p^{o}	Vapour pressure determined from data of Schenck and Neumann	± 20
t	Time of sampling	± 1
Δh	Change in height from evaporation experiments	± 10
s	Slope of line from concentration-time plot, calculated statistically	± 10

BIBLIOGRAPHY

1. Knudsen, M.H., The Kinetic Theory of Gases (Methuen and Co., London, 1934).
2. Kennard, E.H., The Kinetic Theory of Gases (McGraw-Hill, London and N.Y., 1938).
3. Wyllie, G., Proc. Roy. Soc. A 197, 385 (1949).
4. Hirth, J.P. and Pound, G.M.
5. Knudsen, M., Ann. Phys. 47, 697 (1915).
6. Neumann, K. and Schmoll, K., Z. Phys. Chem. 64, 847 (1960).
7. Volmer, M. and Estermann, I., Z. Phys. 7, 1, 13 (1921).
8. Holden, R.B., Speiser, R, and Johnston, H.L., J. Am. Chem. Soc., 70, 3897 (1943).
9. Alty, T. and MacKay, C.A., Proc. Roy. Soc. A 149, 104 (1935).
10. Ward, R.G., J.I.S.I. 201, 11 (1963).
11. Knacke, O. and Stranski, I.N., Prog. in Met. Phys. 6, (Permagon Press, London and N.Y., 1956).
12. Glasstone, S., Laidler, K.J. and Eyring, H., The Theory of Rate Processes (McGraw-Hill Co. London and N.Y., 1941).
13. Herzfeld, K., J. Chem. Phys. 3, 319 (1935).
14. Stearn, A.G., and Eyring, H., J. Chem. Phys. 5, 113 (1937)
15. Neumann, K., Z. Phys. Chem. 16, 196 (1950).
16. Penner, S.S., J. Phys. Chem. 52, 367 (1948).
17. Mortensen, E.M. and Eyring, H., J. Phys. Chem. 64, 847 (1960).
18. Wert, C.A. and Zener, C., Phys. Rev. 76, 1169 (1949).
19. Kincaid, J.F. and Eyring, H., J. Chem. Phys. 6, 620 (1938).
20. Spingler, H., Z. Phys. Chem., (B) 52, 90 (1942).

21. Melville, H.W. and Gray, S.C., Trans Faraday Soc. 32, 271, 1026 (1936).

22. Littlewood, R. and Rideal, E., Trans Faraday Soc. 52, 1598 (1956).

23. Penner, S.S., J. Phys. Chem. 56, 475 (1952).

24. Stranski, I.N. and Wolff, G., Research 4, 15 (1951).

25. Kirkwood, J.G., J. Chem. Phys. 18, 380 (1950).

26. Lype, E.F., A.S.M.E. Trans. 77, 211 (1955).

27. Zwick, S.A., J. Appl. Phys. 31, 1735 (1960).

28. Bradley, R.S. and Shellard, A.D., Proc. Roy. Soc. A 198, 239 (1949).

29. Heideger, W.J., Dissertation Abst. 20, 3673 (1960).

30. Pruger, W., Z. Phys. Chem. 115, 202 (1940).

31. Trevoy, P.J., Ind. Eng. Chem. 45, 2366 (1953).

32. Hickman, K.C., Ind. Eng. Chem. 46, 1442 (1954).

33. Hickman, K.C. and Torpey, D.J., Ind. Eng. Chem. 44, 1882 (1952).

34. Bennewitz, K., Ann. Phys. 59, 193 (1919).

35. Ipsen, H.N., Fundamentals of Vacuum Heat Treating (Ipsen Industries, 1962).

36. Spendlove Jr. H.R., Servi, I.S. and Fritzler, G.A., Vacuum Metallurgy (Electrochem. Soc. 1954) p.24.

37. Ham, J.L. and Carr F.L., I bid, p. 35.

38. Saller, H.A., Dickerson, R.F. and Foster Jr., E.L., I bid, p. 49.

39. Wooding, P.J. and Sieckman, W., Metal Progress 77 (No. 1), 116 (1960).

40. Spendlove, M.J., Vacuum Metallurgy (Electrochem. Soc.), (1954), p. 192.

41. Damara, F.N., Huntington, J.S. and Machlin, E.S., J.I.S.I. 191, 266 (1959).

42. Bennett, G.H.J., Protheroe, H.T. and Ward, R.G., J.I.S.I. 195, 174 (1960).

43. Walas, S.M., Reaction Kinetics for Chemical Engineers (McGraw-Hill, 1959).

44. Parlee, N.A., Seagle, S.R. and Schuhmann Jr. R., Trans. A.I.M.E. 132 (1958).

45. Mauret, P. and Vorsanger, J.J., Compt. Rend. 248, 1808 (1959).

46. Olette, M., Memoires Scientifiques de la Revue de Metallurgie 57, No. 6, 467 (1960).

47. King, T.B., Vacuum Metallurgy (Reinhold Pub. Co., N.Y., 1958), p. 38.

48. Machlin, E.S., Trans. A.I.M.E. 314, 218 (1960).

49. Darken, S.L. and Gurry, R.W., Physical Chemistry of Metals (McGraw-Hill 1953).

50. Spendlove, M.J., Vacuum Metallurgy (London Interscience, 1961) p. 1065.

51. Ilschner, B. and Humbert, J., Z. Metallk. 51, 626 (1960).

52. Moelwyn and Hughes, Kinetics of Reactions in Solution (Oxford University Press, N.Y. 1947).

53. Treyball, R.E., Mass Transfer Operations (McGraw-Hill, 1955), p. 349.

54. Langmuir T., Phys. Rev. 2, 329 (1913).

55. Higbie, R., Trans A.I. Ch. E. 31, 365 (1935).

56. Schenck, H. and Neumann F., Arch. fur das Eisen. 29, 263 (1958).

57. Ohtani, M., Sci. Rep. Inst. Tohoku Univ. Ser A 3, 337 (1956).

58. Morris, J.P. and Zellars, G.R., Trans A.I.M.T. 206, 1086 (1956).

59. Brown, Boveri Co., Report from the Brown, Boveri Co., Mannheim, No. 5 (1959).

60. Knuppel, H. and Oeters, F., Arc. fur das Eisen. II, 729 (1962).

61. Metals Handbook, American Society of Metals.

62. Tocco Co., Bulletin No. 39 P6, The Ohio Crankshaft Co.

63. Ward, R.G., Introduction to the Physical Chemistry of Iron and Steelmaking (Arnold, London, 1962) p. 150.

64. Bodsworth, C., Physical Chemistry of Iron and Steel Manufacture (Longmans, 1963).

65. Kirshenbaum, A.D. and Cahill, J.A., Trans A.I.M.E. 224 No. 4, 816 (1962).

66. Kubaschewski, O. and Evans, E.L., Metallurgical Thermochemistry (Permagon, London, 1958) p. 326.

67. Guest, P.G., Nummerical Methods of Curve Fitting (University Press, Cambridge, 1961).

68. Mickley, H.S. Sherwood, T.K. and Reed, C.E., Applied Mathematics in Chemical Engineering (McGraw-Hill, N.Y., 1957).

69. Bankier, J.D., McMaster University, private communication.

70. Spendlove, M.J., Vacuum Metallurgy (Electrochem. Soc. 1954) p. 192.

71. Brotzmann, K., Arch. fur das Eisen 31, 67 (1960).

72. A.S.T.M. Methods for Chemical Analysis of Metals (A.S.T.M., 1961).

73. Smithells, C.J., Metals Reference Book (Butterworth, London, 1962) p. 601.

74. Beeton, T.B., J.I.S.I. 201, 913 (1963).

75. Sehgal, V.D. and Mitchell, A., J.I.S.I. 202, 193 (1964).

76. Volk, W., Applied Statistics for Engineers (McGraw-Hill, 1958).

APPENDIX A

MATHEMATICAL ANALYSIS

The equations:

$$Y = aX + b \tag{1}$$

$$\ln Y = aX + b \tag{2}$$

both represent straight lines, with Y and ln Y respectively as a function of X.

In both of the above cases, it is assumed that the X variable is precisely known and that the Y variable is imprecisely known.[67] In order to evaluate the best straight line, the sums of the squares of the deviations from the straight line is minimized. Where $\bar{y}$ is the estimated value of y, the sum of the squares of the deviations for equation (1) is given by:

$$\sum_{1}^{N} (y-\bar{y})^2 \tag{3}$$

However, equation (3) has been evaluated on the assumption that each Y variable for a given X is equivalent, that is, the standard deviation of each point, σ_i is the same.

In equation (2), however, the standard deviation of observations Y may be the same, but by the nature of the semi log plot, the standard deviation of log Y is not constant, that is, each point is not equivalent.

$$dY = Y d \ln Y \tag{4}$$

From equation (4) it is seen that a change in observation Y is equivalent to Y times a change in the log of Y. In applying this statement to the least squares line for an equation of type (2) above,

$$\sum_{1}^{N} \left[(\ln Y - \ln \bar{Y})\, Y\right]^{2} \qquad (5)$$

Equation (5) is treated in the usual least-square manner:

$$\sum_{1}^{N} (\ln Y - aX - b)^{2}\, Y^{2} \qquad (6)$$

To minimize the sum of the squares of the deviations:

$$\frac{\partial}{\partial a} f\,(X_i, Y_i) = 0 \text{ and } \frac{\partial}{\partial b} f\,(X_i, Y_i) = 0 \qquad (7)$$

Equation (7) then leads to:

$$a = \frac{\sum_{1}^{N} X\,(\ln Y) Y^{2} \sum_{1}^{N} Y^{2} - \sum_{1}^{N} (\ln Y) Y^{2} \sum_{1}^{N} X\,Y^{2}}{-\left[\sum_{1}^{N} X\,Y^{2}\right]^{2} + \sum_{1}^{N} X^{2}\,Y^{2} \sum_{1}^{N} Y^{2}} \qquad (8)$$

$$\text{and } b = \frac{-a \sum_{1}^{N} X\,Y^{2} + \sum_{1}^{N} (\ln Y)\, Y^{2}}{\sum_{1}^{N} Y^{2}} \qquad (9)$$

From equation (8), it is impossible to estimate a possible error in the determination of the slope[69]. The error in the slope must be determined from a least squares plot and estimated to be the error in the weighted least squares.

The analysis is taken from Volk[76] and is written:

$$(n-2)S_{y/x}^2 = \Sigma Y^2 - \frac{(\Sigma Y)^2}{n} - a\,\Sigma XY + a\,\frac{\Sigma X\,\Sigma Y}{n} \qquad (10)$$

where $S_{y/x}^2$ is regression of y upon x

the standard deviation of the slope is estimated by

$$S_b = \frac{S_{y/x}}{\sqrt{\Sigma(X-\bar{X})^2}} \qquad (11)$$

APPENDIX B

CRUCIBLE - MELT INTERACTIONS

In induction melting techniques a pollution reaction occurs due to the interaction of the crucible material with the melt.

$$1/3\ Al_2O_3 = 2/3\ Al + O \qquad (1)$$

$$MgO = Mg + O \qquad (2)$$

Machlin[48] proposes a theoretical treatment for this interaction assuming the diffusion of the reaction products through a static boundary layer at the crucible - melt interface.

Olette[46] in studying the evaporation of arsenic from iron noted that the evaporation characteristics could conceivably be affected by the presence of Cu, Sn, Si and Al in the melt. These third elements are present in small amounts and no conclusive evidence is shown by the results.

Olette did show that the type of crucible used had a drastic effect on evaporation properties of Al and Si. He postulates that an unexpected increase in evaporation rate is due to the formation of volatile suboxides:

$$MgO_s + Al_{Fe} = Al_2O)_g + Mg_g \qquad (3)$$

$$MgO_s + Si_{Fe} = SiO)_g + Mg_g \qquad (4)$$

He also showed that Al evaporation from Al_2O_3 crucibles was quite negligible, until some silica was added:

$$SiO_{2s} + Al_{Fe} = Al_2O_g + SiO_g \qquad (5)$$

Spendlow et al[36] studying the vacuum melting of high alloy materials utilized three crucible materials, alumina, magnesia and Zircoa. They concluded that on their system (Ni, Cr, Mo, Ti, Al, C) that the evaporation characteristics were independent of the crucible material used. Their results gave evidence that in Mg O crucibles Mg was evaporated (because of its high vapour pressure) but that its presence had no noticeable effects on the system.

Knuppel and Oeters[60] studying the evaporation of hydrogen from iron, under reduced pressures determined specific evaporation coefficients of 7.25×10^{-3} sec^{-1} and 11.47×10^{-3} sec^{-1} for alumina and magnesia crucibles respectively. They cite the work of Brotzmann[71] in explaining the difference is caused by porosity variations. They state the alumina crucible was sintered with Ca O to form a very compact crucible, whereas the Mg O crucible was more porous, which resulted in an increase in the evaporation area and hence an apparent increase in the specific evaporation coefficient.

Figure 29 depicts a magnesia crucible after it had been used for ten melts. The actual penetration of the iron into the crucible wall is seen to be very uniform and quite slight. None of the rammed crucibles used displayed any cracking due to thermal stresses, however, the prefired zircoa crucible did show signs of cracking and some melt penetration.

The magnified penetration of iron into the crucible wall is shown in the micrograph of figure 30. No attempt has been made in the present work to identify the products of the crucible melt interaction, however, Spendlow et al[36] have identified a spinel, some feldspar and some forsterite. The reaction products are seen in figure 30, the light section being the iron.

The experimental results seem to substantiate the fact that the crucible material has no effect on the evaporation of manganese. The majority of the experiments were carried out on magnesia crucibles (run No. 10 onwards), however, the results of experiments on the alumina crucibles (runs 2, 3, 5) and zircoa crucibles (runs 8, 9) are not inconsistent with the magnesia crucible results.

The experiments were performed on steel with a typical analysis (in weight percent):

C	P	S	Mn
.057	.01	.026	.33

A typical analysis after vacuum degassing is:

C	P	S	Mn
.004	.01	.007	.29

From the activity data of Schenck and Neumann[56] it is seen that the low carbon content of the melts would have very little effect on the manganese activity, and also the small amounts of S and P present would be expected to have no noticeable effects on manganese. The effect of third element on the evaporation of manganese is thus assumed negligible.

APPENDIX C

TEMPERATURE MEASUREMENT

The obvious advantage of two colour pyrometry over normal optical and total radiation pyrometry is that emissivities are relatively unimportant. The temperature is measured as a function of the ratio of the radiant energy emitted in two wavelength bands. By utilizing the ratio technique, the errors caused by target emissivity are greatly reduced as are any contamination effects such as gases and films on windows, as long as both wavelengths are affected equally.

For radiation in the visible portion of the spectrum, Planck's law reduces to Wien's approximation:

$$E_{\lambda_1} = \varepsilon_{\lambda_1} C_1 \lambda^{-5} \exp - C_2/\lambda_1 T$$

where $E_{\lambda_1} \equiv$ the monochromatic emissive power of the body

$\lambda_1 \equiv$ wavelength

$T \equiv$ temperature of the body

$C_1, C_2 \equiv$ constants

$\varepsilon_{\lambda_1} \equiv$ emissivity of the body at λ_1

The ratio of the radiation emitted from a body at two different wave lengths is:

$$R = \frac{\varepsilon_{\lambda_1} C_1 \lambda_1^{-5} \exp - C_2/\lambda_1 T}{\varepsilon_{\lambda_2} C_1 \lambda_2^{-5} \exp - C_2/\lambda_2 T} \qquad (2)$$

$$R \quad \left\{ \left(\left[\frac{\lambda_2}{\lambda_1} \right] \right)^5 \exp - C_2 \left(\frac{\lambda_2 - \lambda_1}{\lambda_2 \quad \lambda_1} \right) \right\} / T_R \qquad (3)$$

where T_R is the temperature of the body as measured

Expression (3) is derived assuming emissivity is a weak function of wavelength.

The two colour pyrometers used (Latronics Colouratio and Milletron Thermoscope) measure the ratio of the energy of the green wavelength to that of the red. Ordinary glass, which was employed as the sight glass for the temperature measurements is opaque to the visible spectrum, and being green coloured has the effect of absorbing the red wavelength and transmitting the green, producing high temperature readings. It was found that a 0.25 inch green glass created an apparent temperature rise of 20° to 30°C and that similar temperature increases were noticed as the thickness of the glass was increased to 1 inch. The use of quartz, which is transparent for wave lengths up to the infra-red region (7000 $\overset{\circ}{A}$) overcomes this effect, as was noticed. One would normally expect an exponential decrease of light intensity transmitted vs the thickness, according to Lambert's Law:

$$I = I_o \exp - 2\alpha x \qquad (4)$$

where I is the intensity transmitted

I_o is the incident intensity

2α is the absorption coefficient of the medium

x is the thickness of the absorbing medium

The experimental results show a linear relationship between the temperature increase and the absorbing medium thickness, up to a thickness of 1 inch.

The experimental results were calculated assuming the surface temperature equivalent to the bulk temperature since the conditions of high turbulence and relatively low evaporation rates should eliminate the possibility of surface cooling. The effect of surface cooling would be to decrease the experimental specific evaporation rate at high temperatures which would decrease the apparent activation energy, indicating more diffusion control than that actually present.

APPENDIX D

Error Analysis

The experimental errors in this study occur in the height estimation, the determination of the slope from the concentration-time plot, the calculation of the activity coefficient for the high carbon determinations, the concentration measurement and the temperature measurement. The experimental errors for each of these quantities are given in table VI. The errors in functions calculated from the measured values were estimated using a technique suggested by Mickley et al[68].

If Q is a function of q_1, q_2 etc., that is,

$$Q = f\,(q_1, q_2, \ldots\ldots q_n) \qquad (1)$$

the differential change in Q resulting from a differential change in the measured quantities q_1, q_2, etc. is:

$$dQ = \frac{\partial f}{\partial q_1}\, dq_1 + \frac{\partial f}{\partial q_2}\, dq_2 + \ldots\ldots\ldots \frac{\partial f}{\partial q_n}\, dq_n \qquad (2)$$

where $\partial f/\partial q_n$ is the partial derivative of the function with respect to the measured quantity q_n and dq_n is the estimated error in q_n.

Thus, for the case of high carbon runs, where,

$$k = \frac{hs}{\gamma} \qquad (3)$$

h = height of melt

s = slope of log concentration time plot

γ = activity coefficient of Mn in high carbon runs.

The maximum total error is then given by:

$$dk = \frac{s}{\gamma}\, dh + \frac{h}{\gamma}\, ds + \frac{hs}{\gamma^2}\, d\gamma \qquad (4)$$

This yields an estimated error in the specific evaporation constant for high carbon runs of approximately ± 20% and approximately ± 10% for low carbon runs. These errors are illustrated on the data points of figure 26.

The experimental evaporation rate of iron was determined from the evaporation experiments, utilizing the decrease in height of the melt. The height measurement was reproducible within ± 0.01 inch for heights of approximately 0.22 inch, resulting in an uncertainty of ± 10%. This also represents the error in the calculation of the experimental evaporation rate of iron, which was calculated from the height difference.

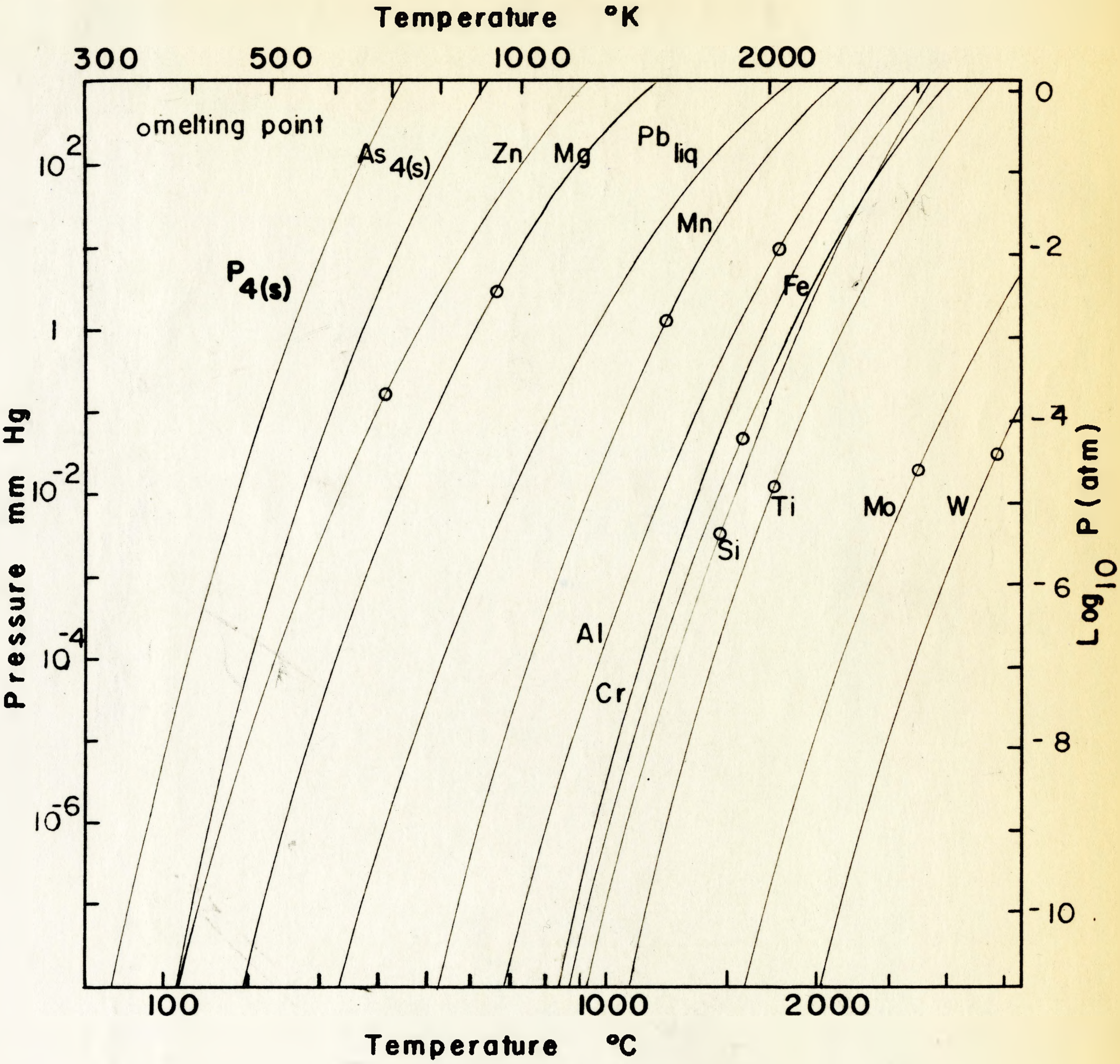

FIGURE I

Vapour Pressure - Temperature Curves

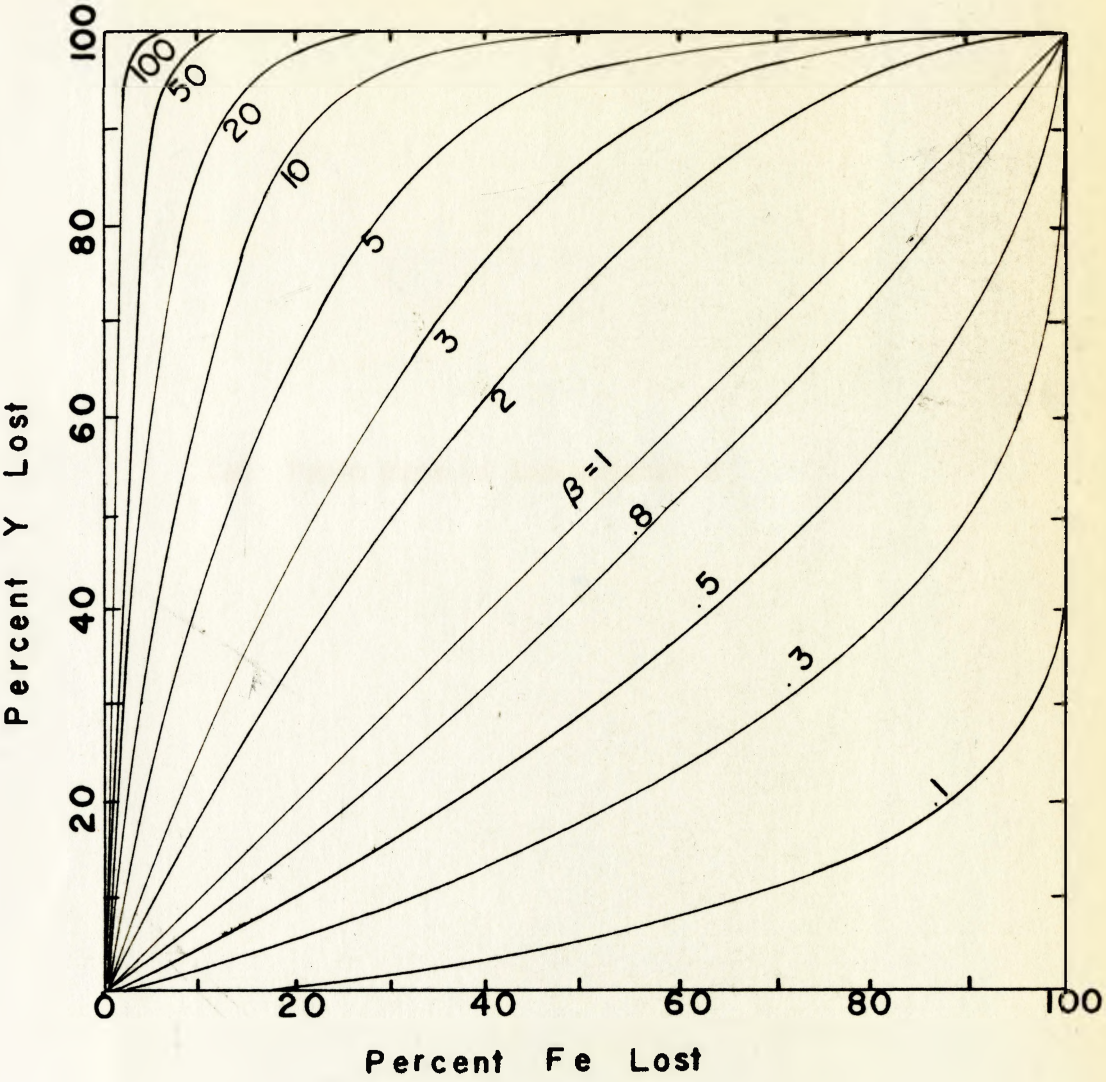

FIGURE 2

Percent of Iron Lost vs Percent of
Element Y lost During Vacuum Treatment

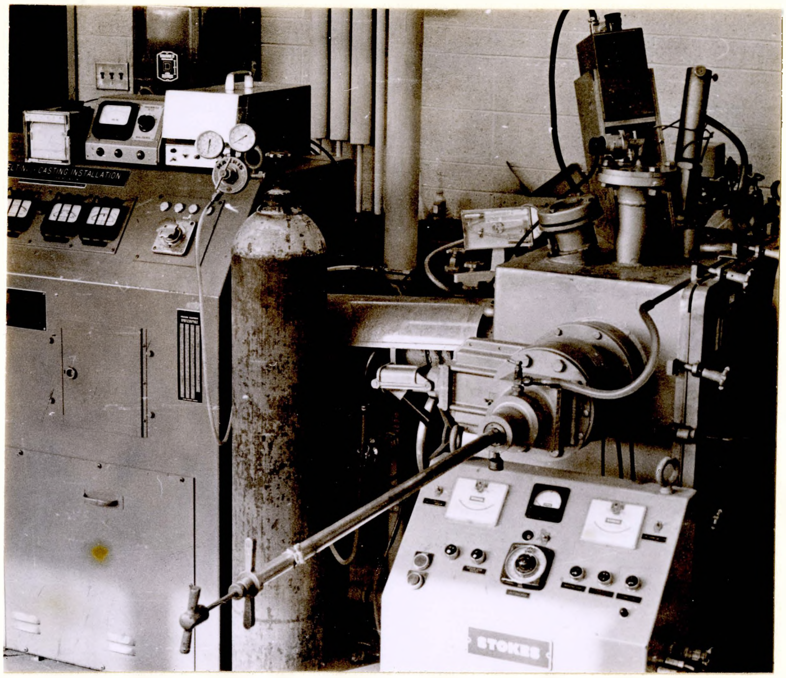

(a) Front view of the apparatus

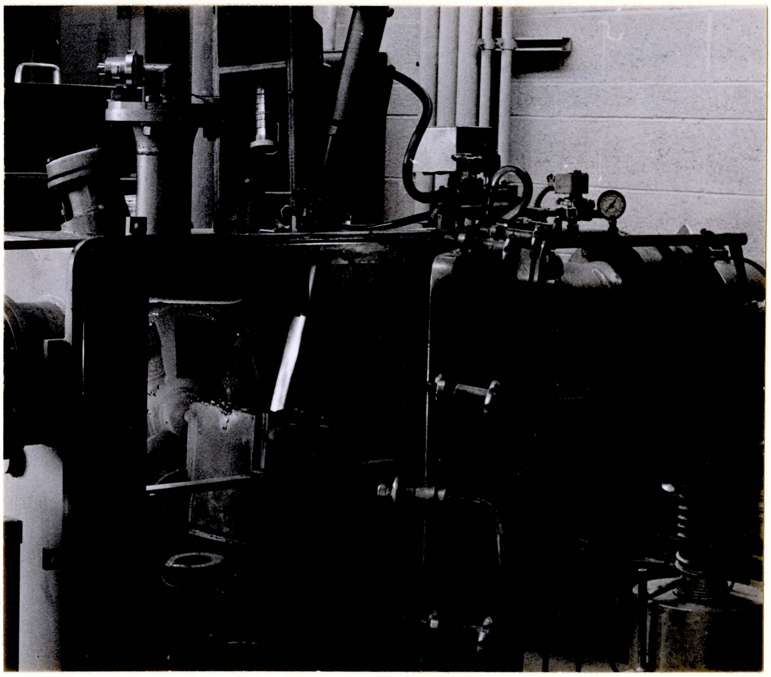

(b) Method of sampling from crucible

Figure 3 - Photograph of the Vacuum apparatus and Associated Equipment

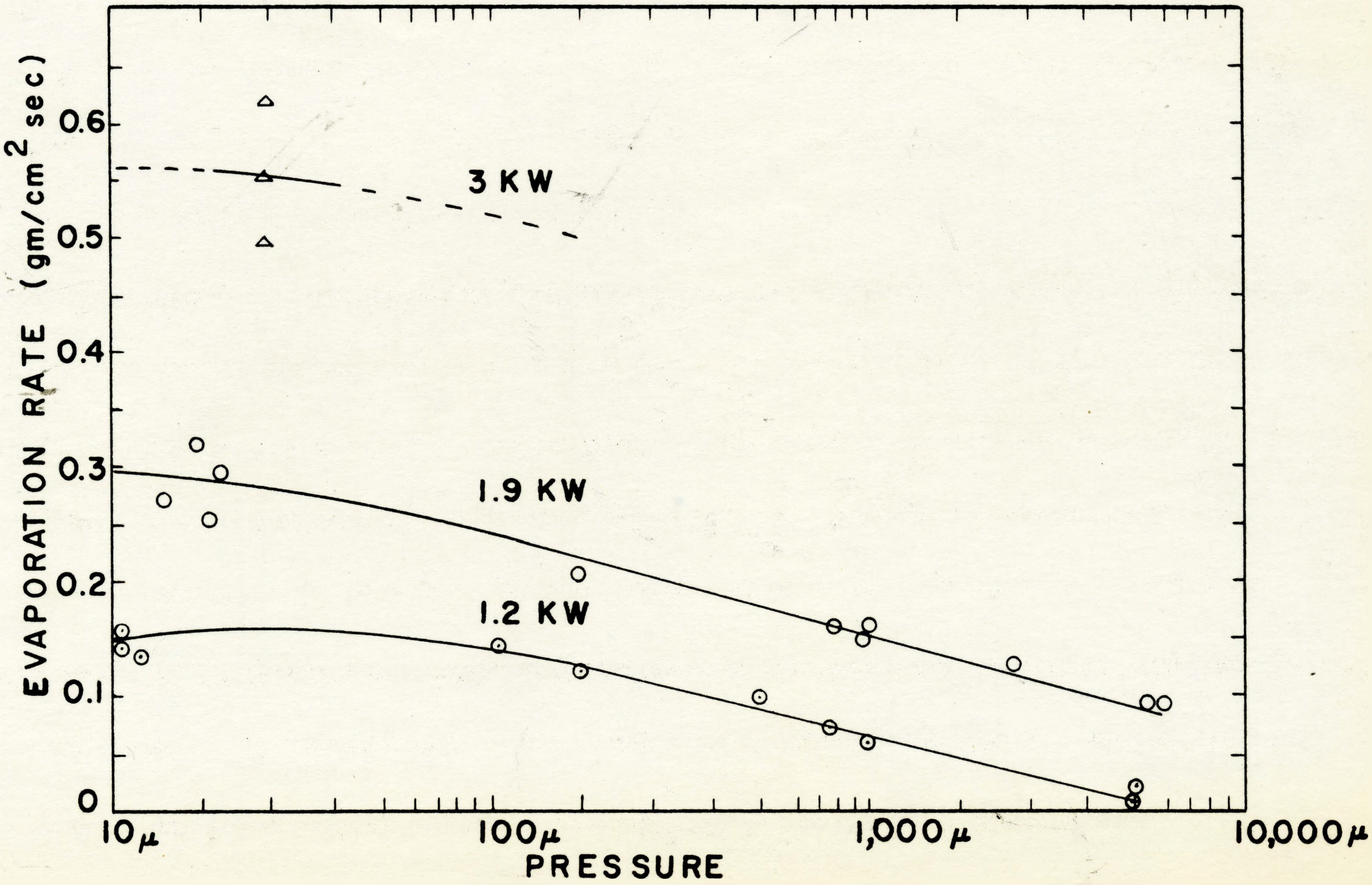

FIGURE 3·1

Effect of Pressure on Rate of Evaporation of Zinc

SCHEMATIC DIAGRAM OF VACUUM APPARATUS

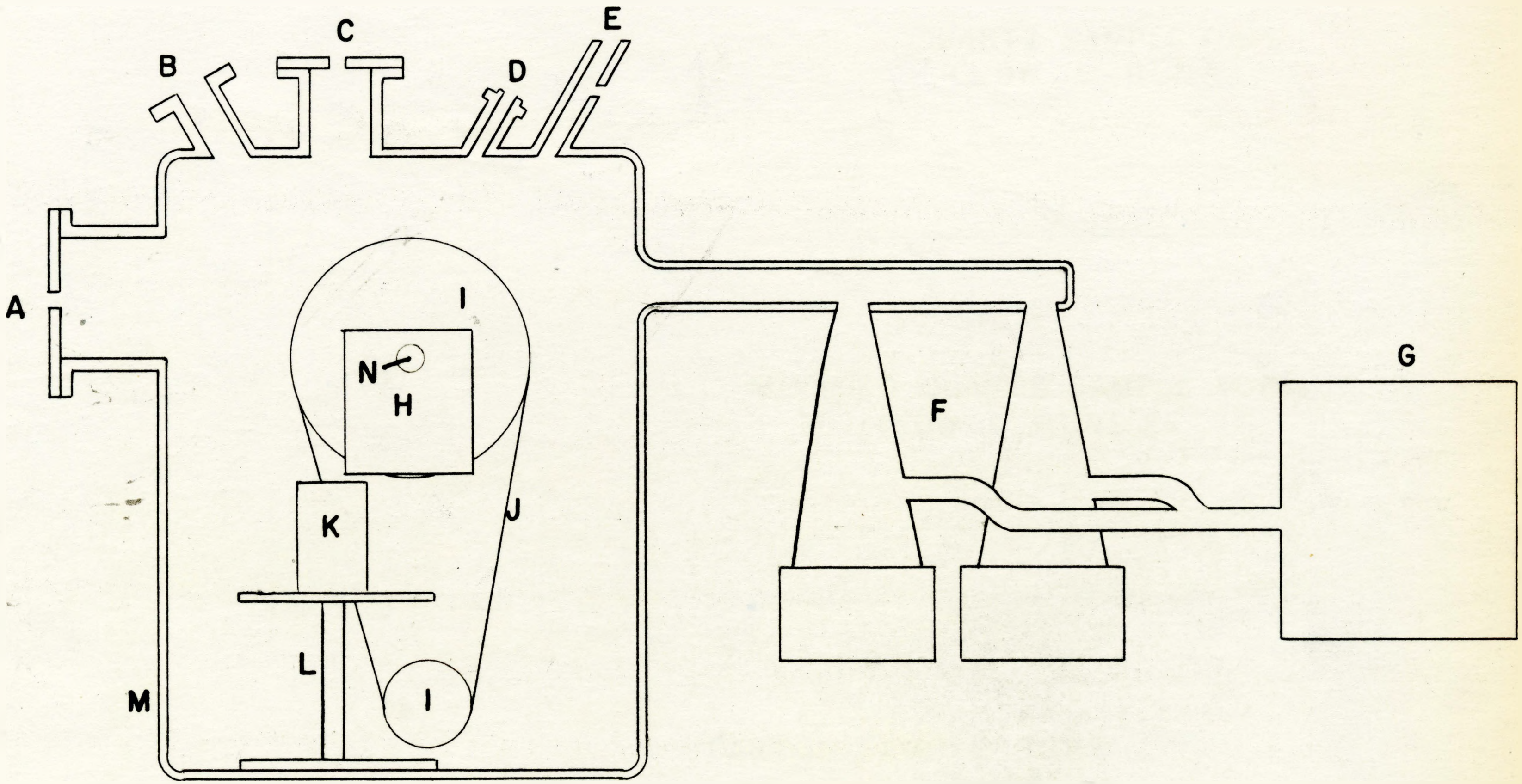

A	Addition Port
B	Observation Port
C	Pressure Measurement
D	Pyrometer Sighting
E	Sample Port
F	Booster Pumps
G	Backing Pump
H	Induction Coil
I – J –	Pouring Mechanism
K	Casting Mould
L	Mould Support
M	Water – Cooled Vacuum Unit
N	Axis of Rotation

FIGURE 4

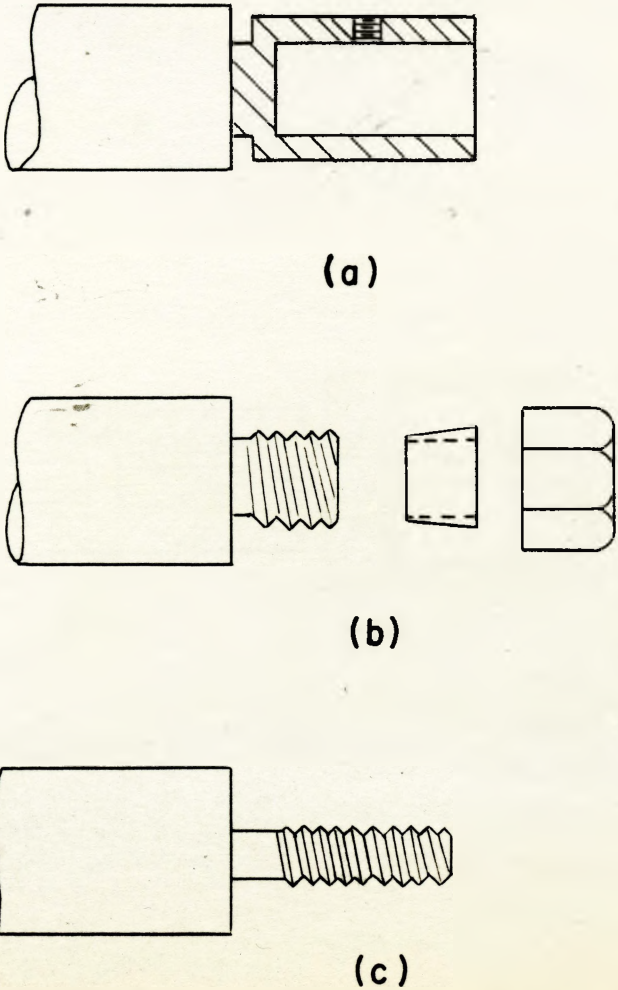

SAMPLING

FIGU

QUARTZ SAMPLE TUBE
(LOW C RUNS)

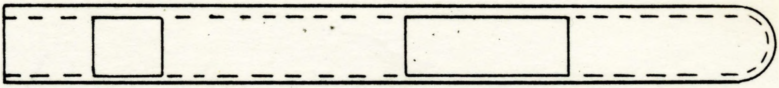

MODIFIED QUARTZ SAMPLE TUBE
(LOW C RUNS)

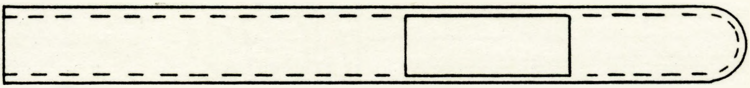

CARBON SAMPLE TUBE
(C SAT'D RUNS)

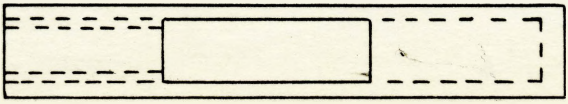

TUBES

RE 5

THERMOCOUPLE ARRANGEMENT

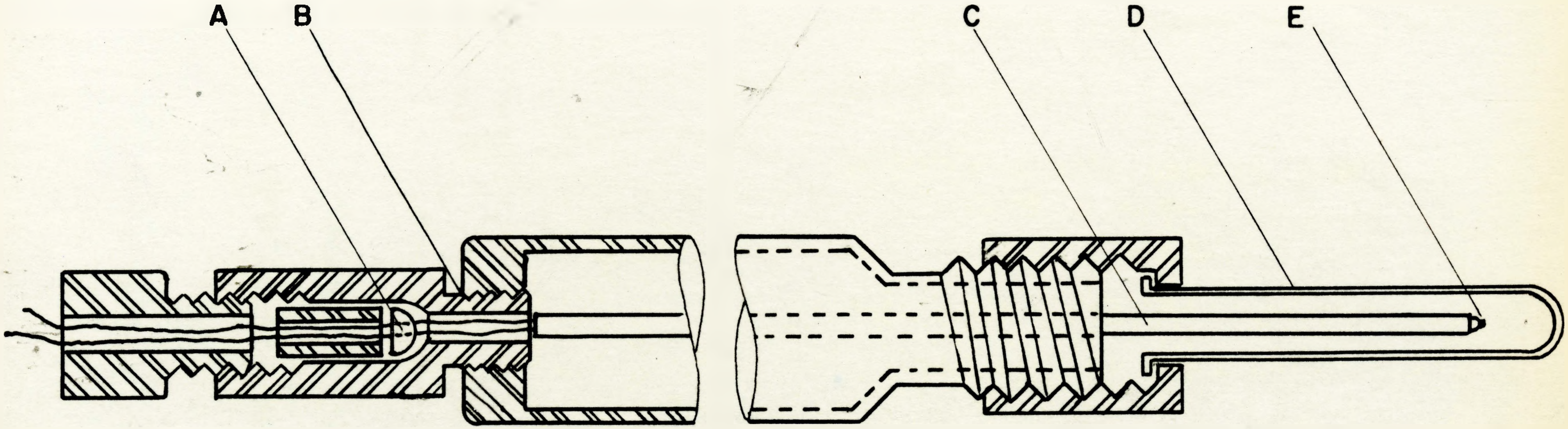

A	Rubber Vacuum Seal
B	Vacuum Pipe Seal
C	Thermocouple Sheath
D	Immersion Sheath
E	Thermocouple Junction

FIGURE 6(a)

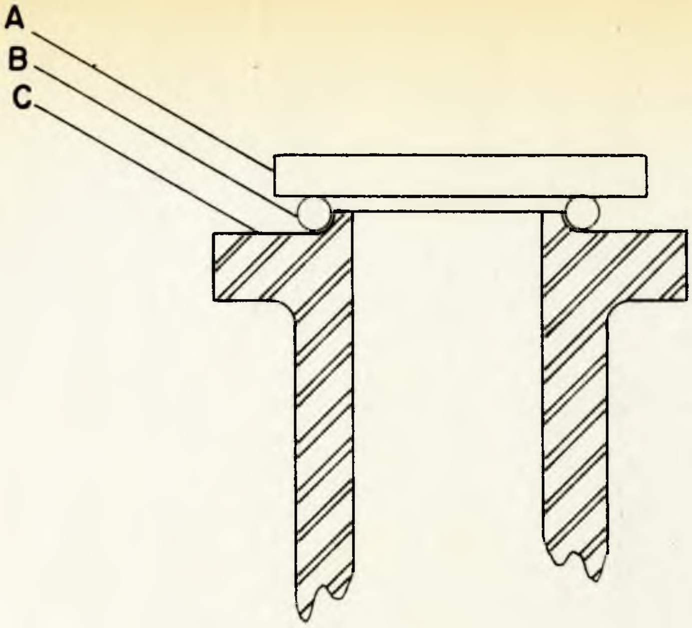

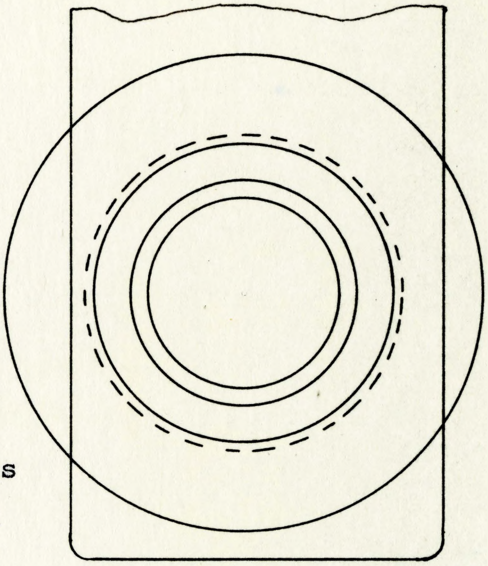

A Pyrometer Sight Glass

B "O" Ring Vacuum Seal

C Observation Port

VACUUM SETUP
FOR
OPTICAL PYROMETER

FIGURE 6(b)

APPARATUS FOR MAKING ADDITIONS
UNDER VACUUM

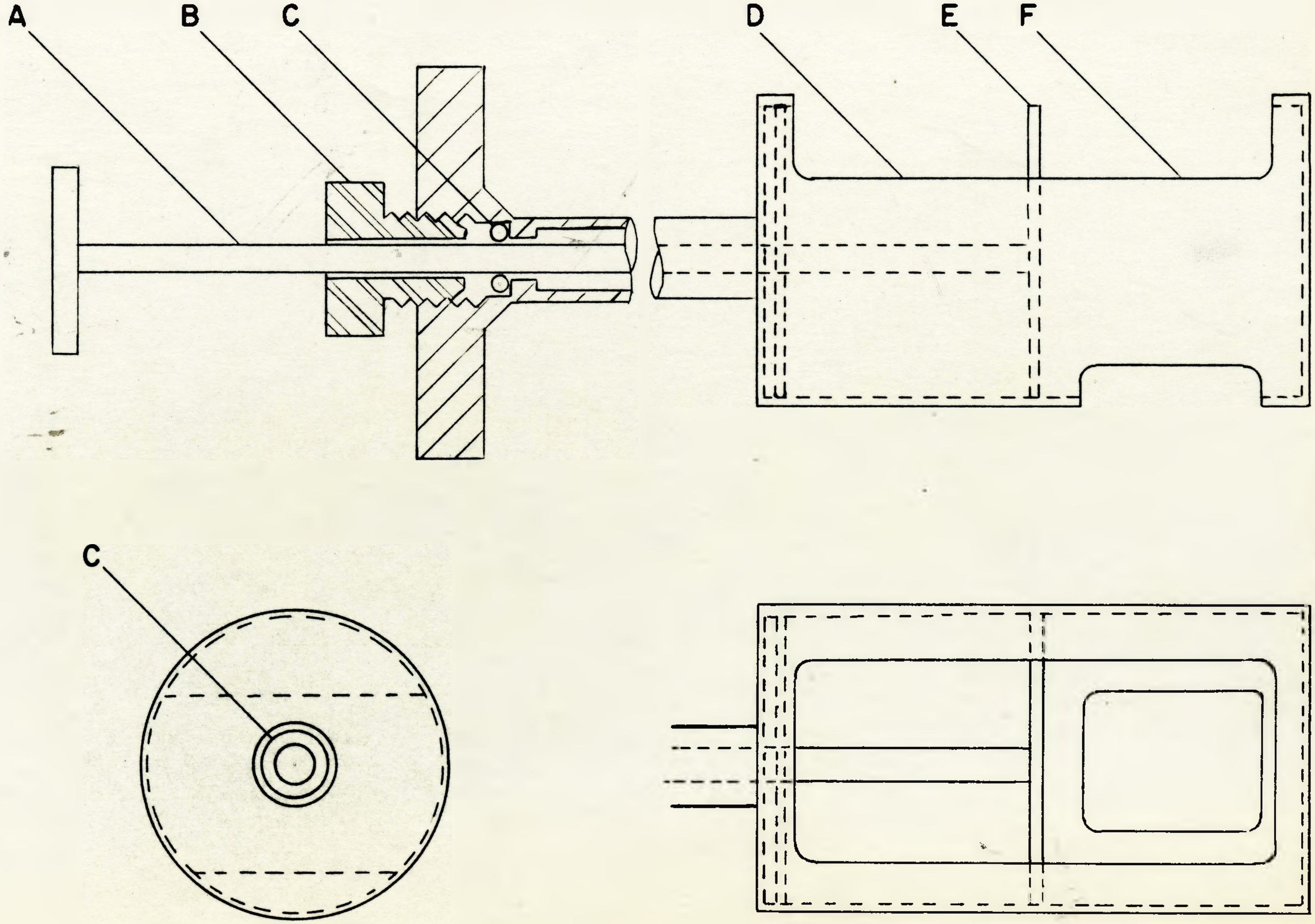

A Addition Control Handle
B Vacuum Seal Control
C Rubber "O" Ring
D Addition Storage
E Sliding Mechanism
F Addition Chamber

FIGURE 7

CONDENSATION EXPERIMENTS

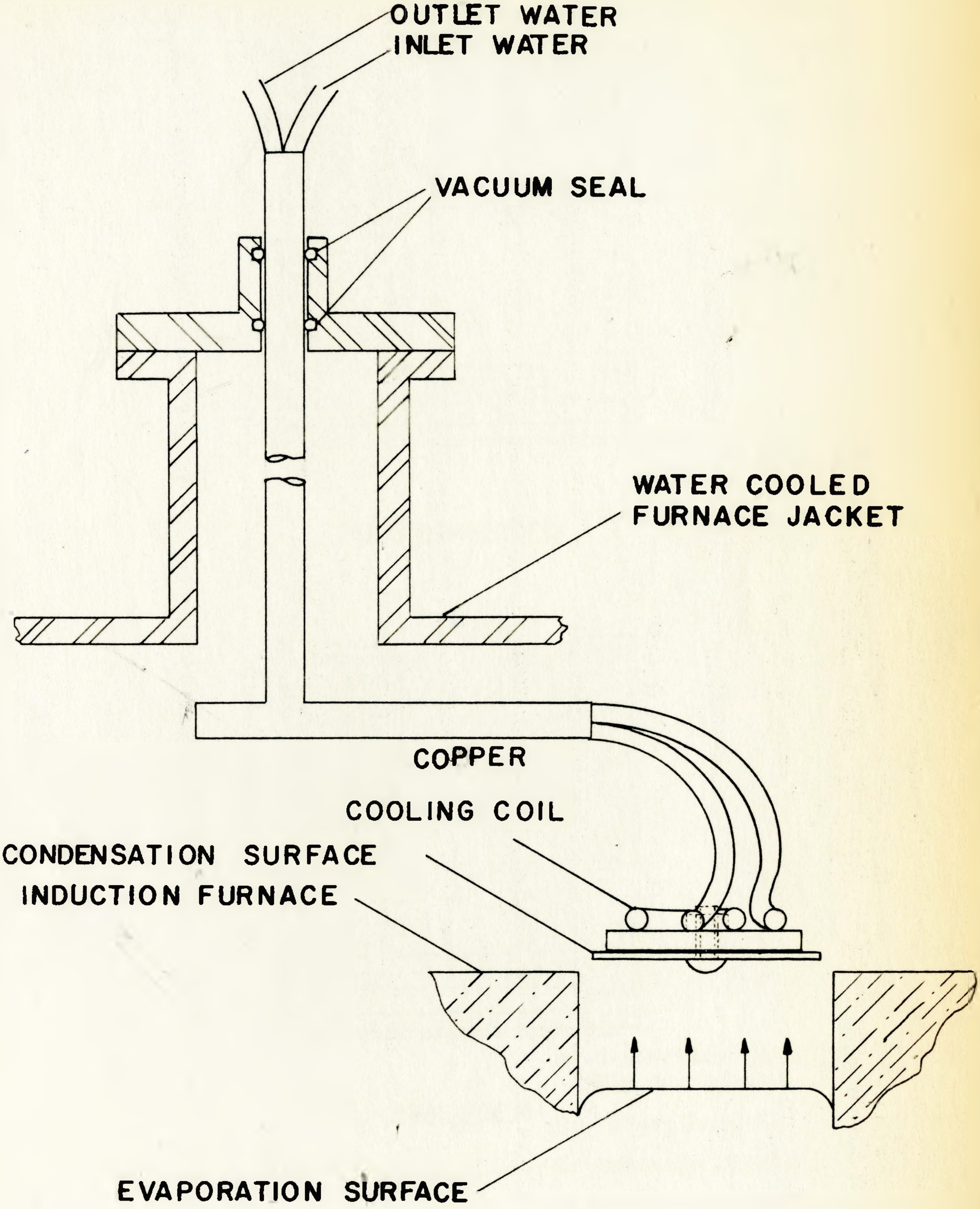

FIGURE 8

INDUCTION FURNACE

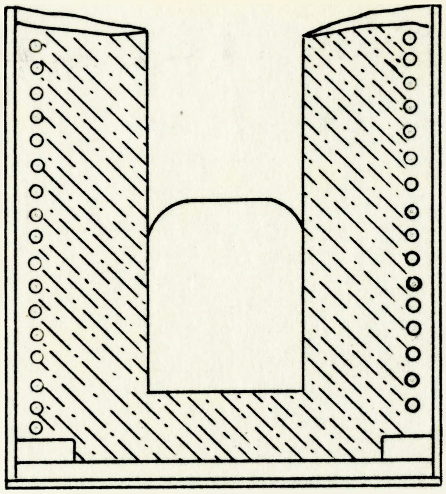

(a) UNSHIELDED

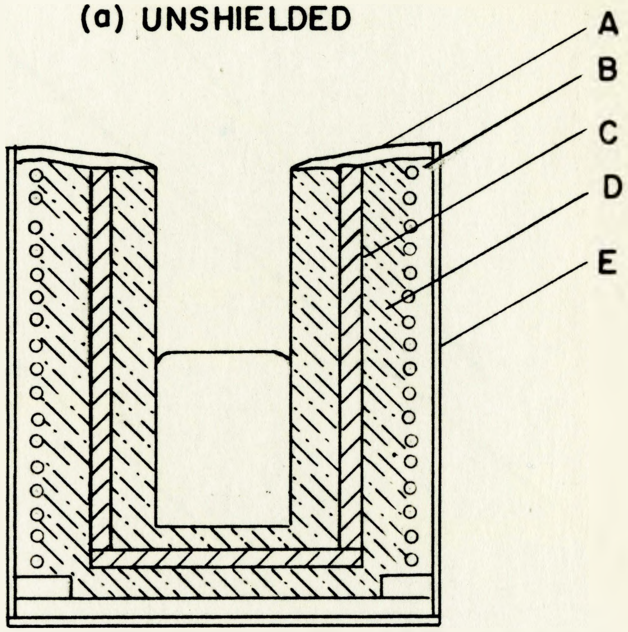

A	Refractory Cement for Pouring Spout
B	Induction Coil
C	Graphite Shield
D	Refractory Material
E	Asbestos Board Box

(b) SHIELDED

FIGURE 9

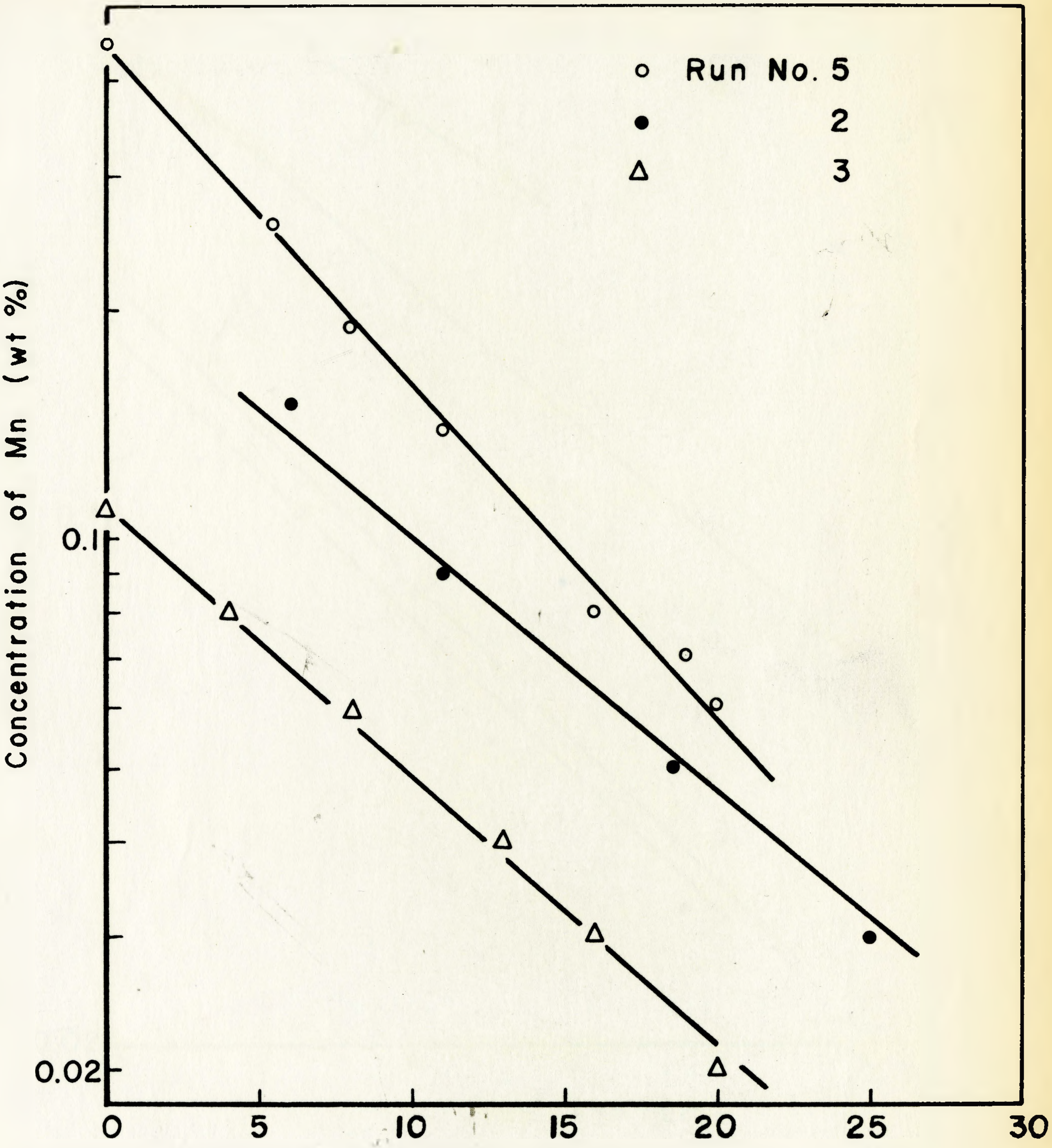

FIGURE 10

Concentration-Time Curves

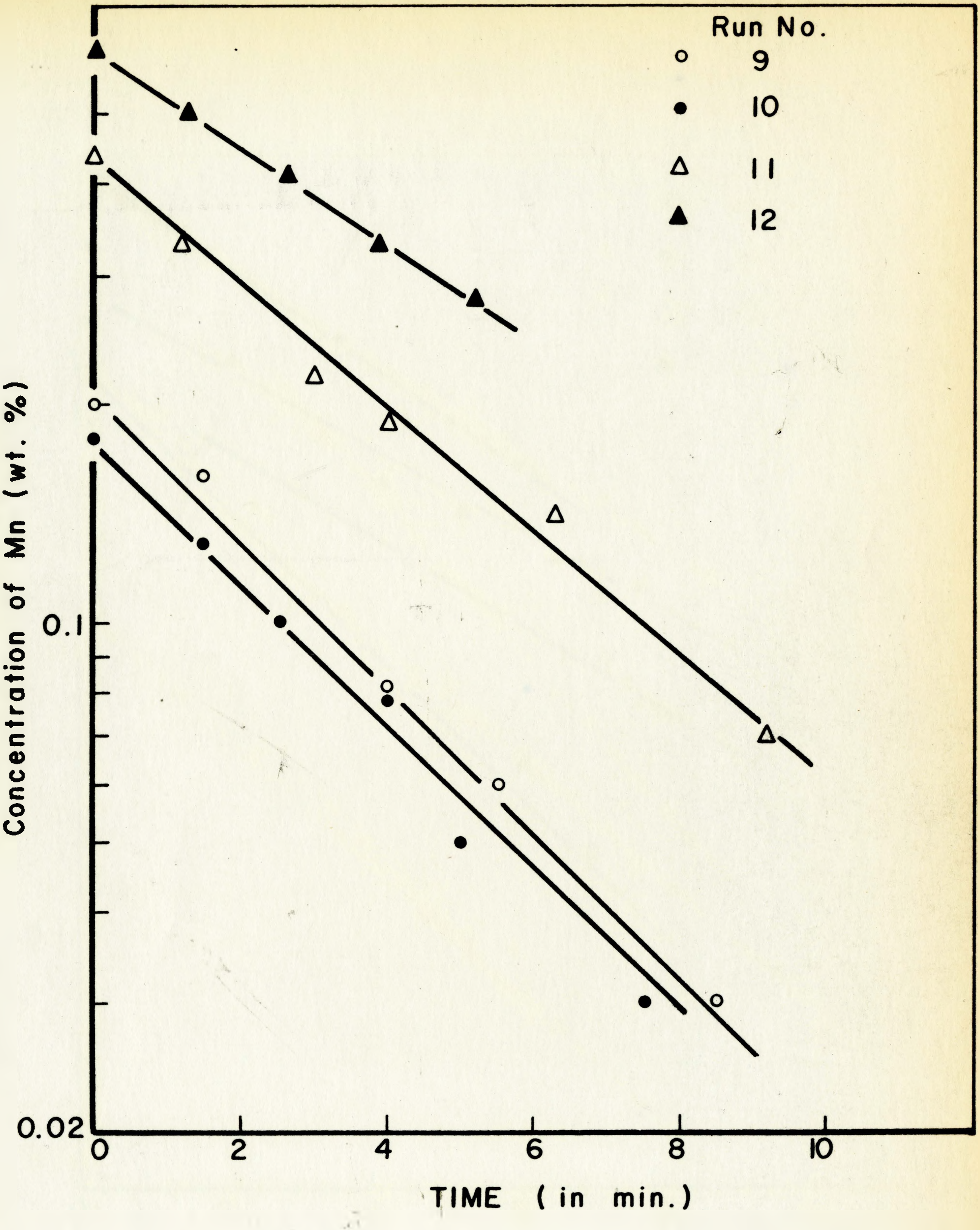

FIGURE II

Concentration – Time Curves

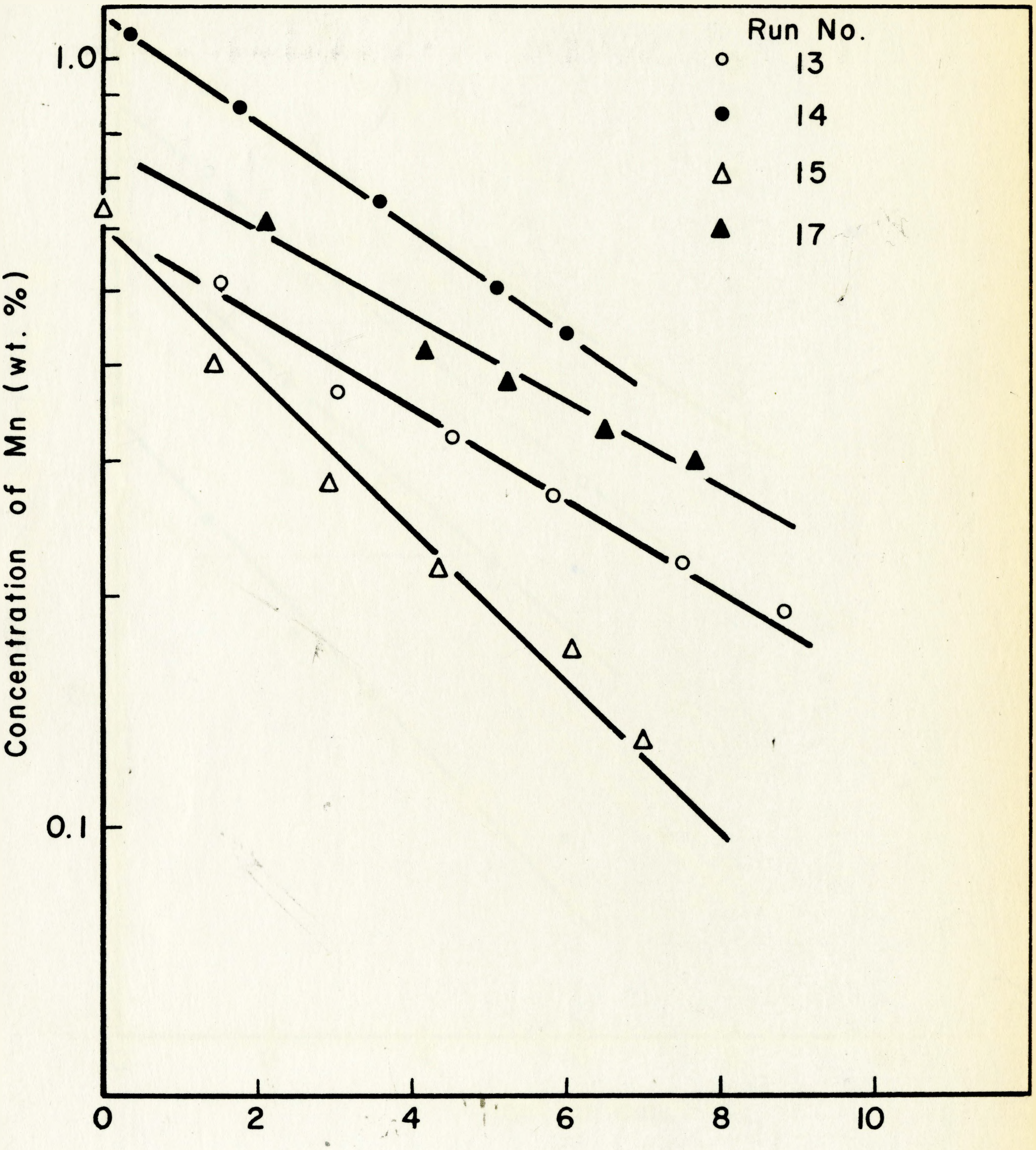

FIGURE 12

Concentration – Time Curves

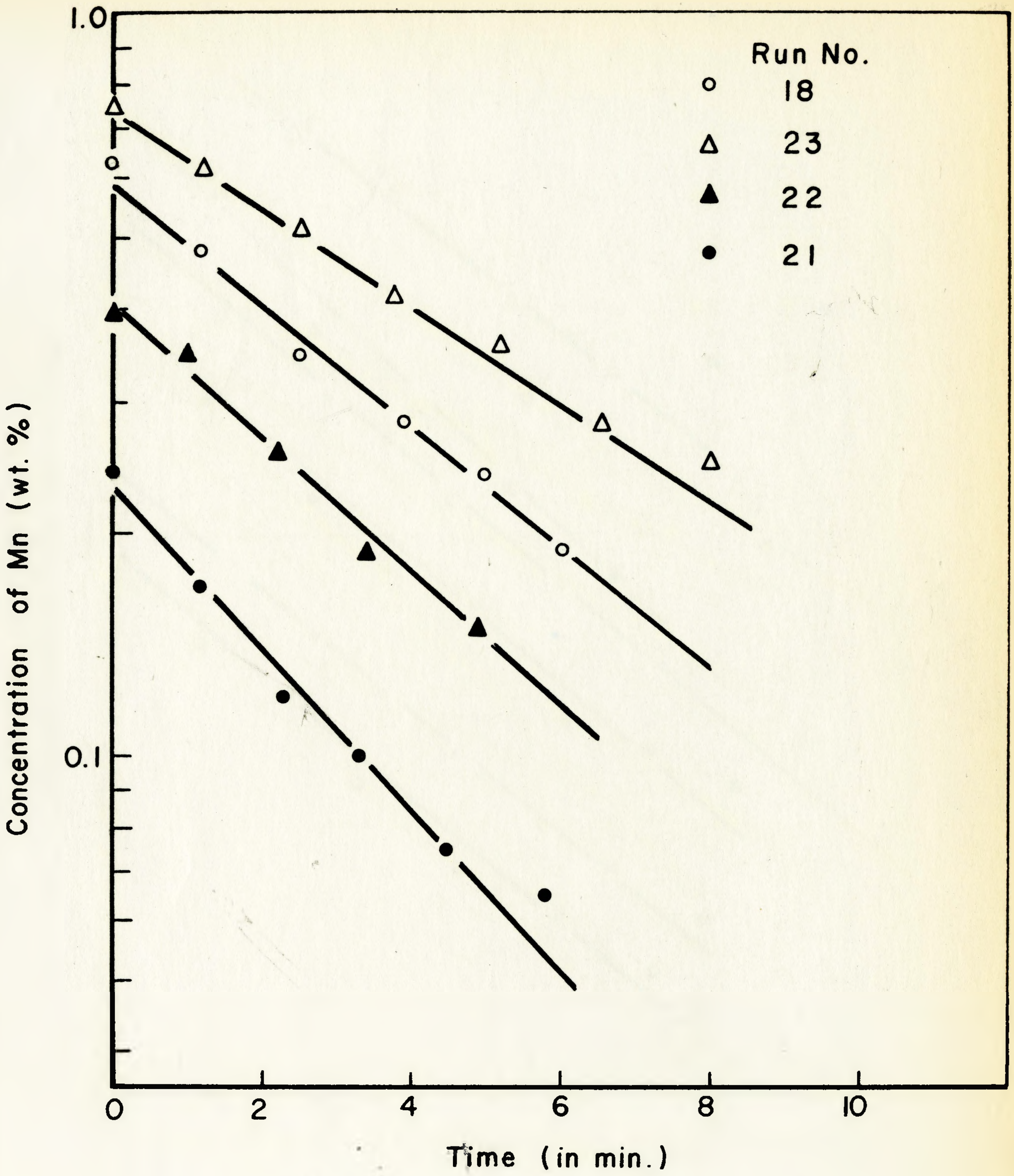

FIGURE 13
Concentration – Time Curves

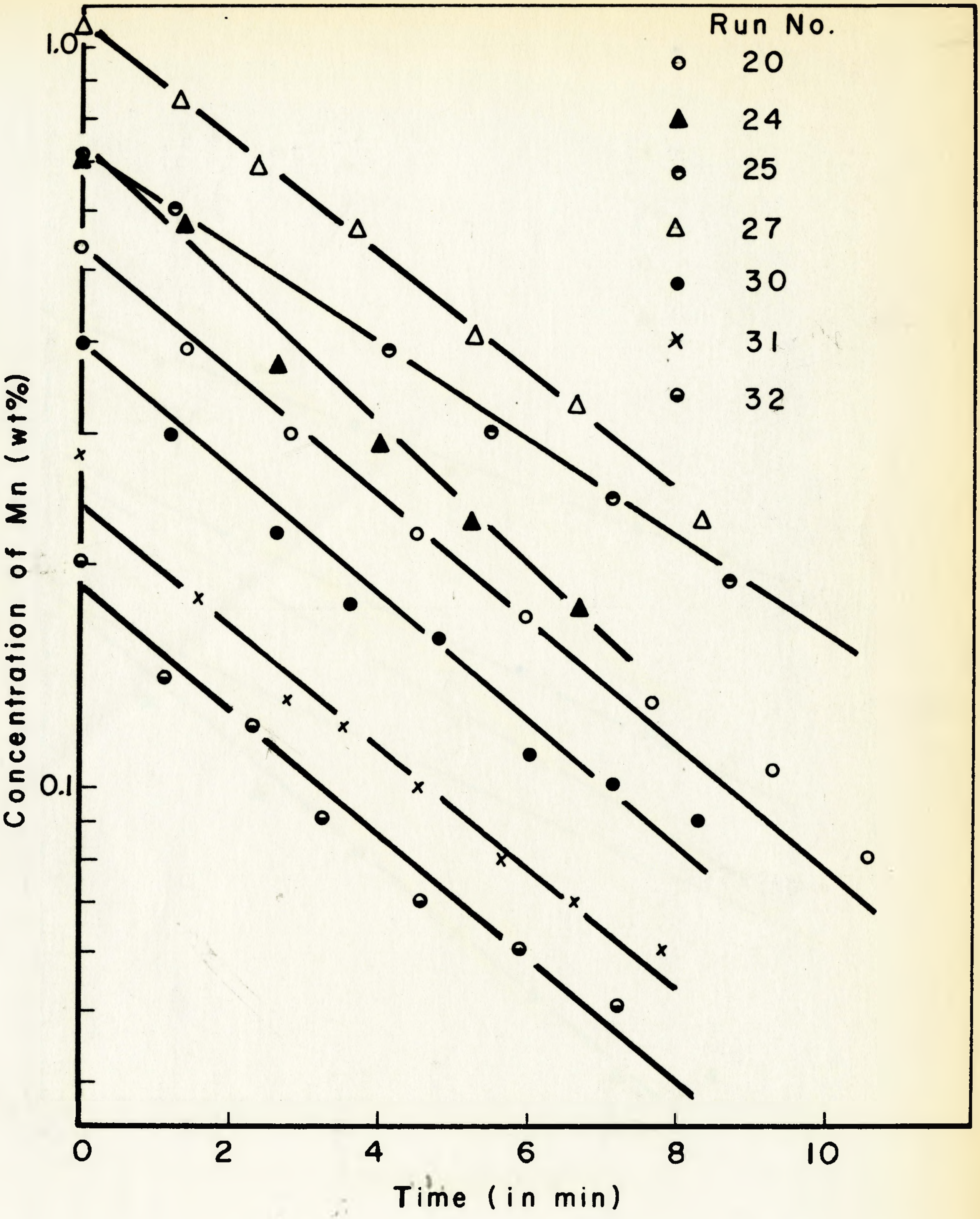

FIGURE 14

Concentration – Time Curves

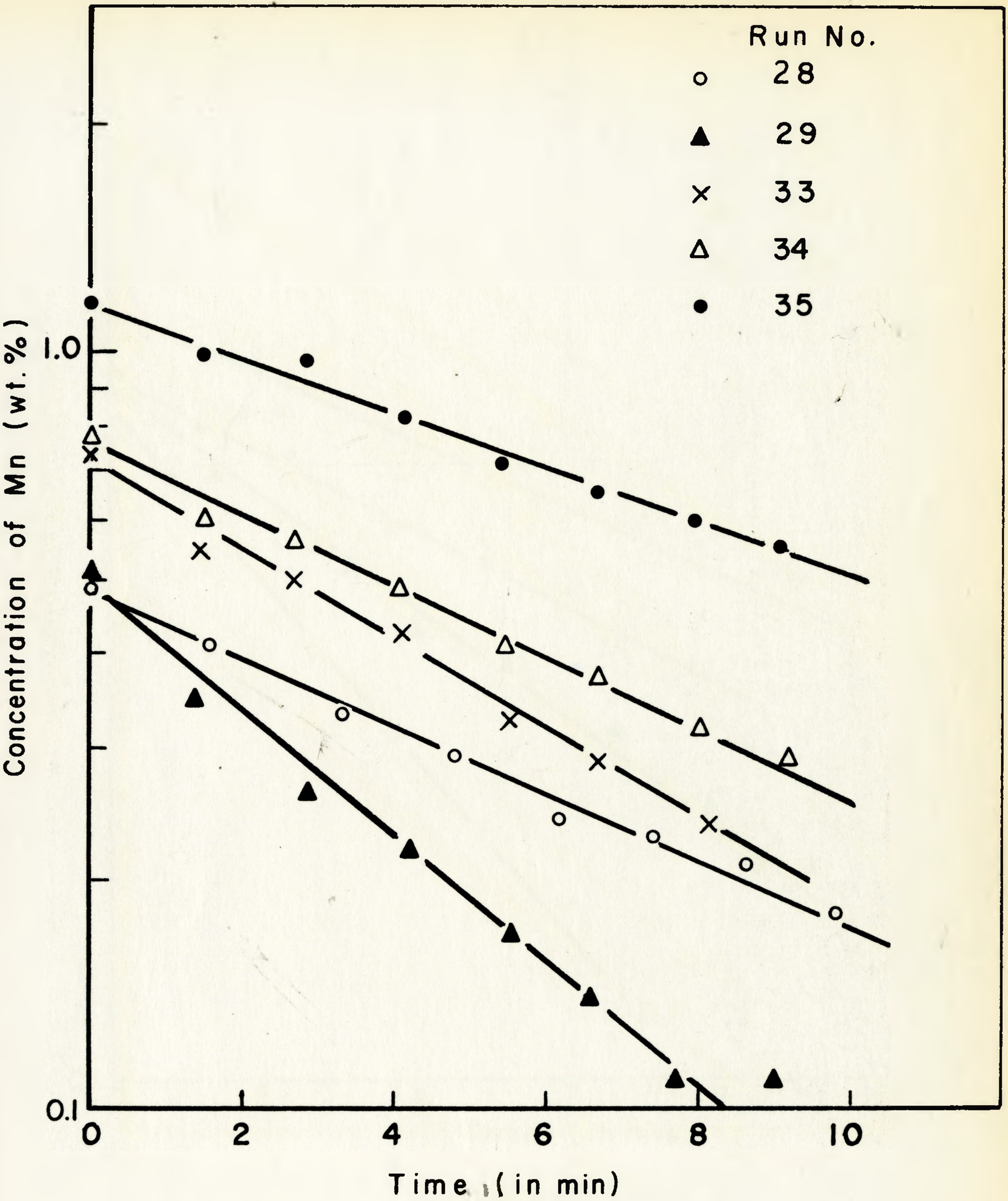

FIGURE 15

Concentration – Time Curves

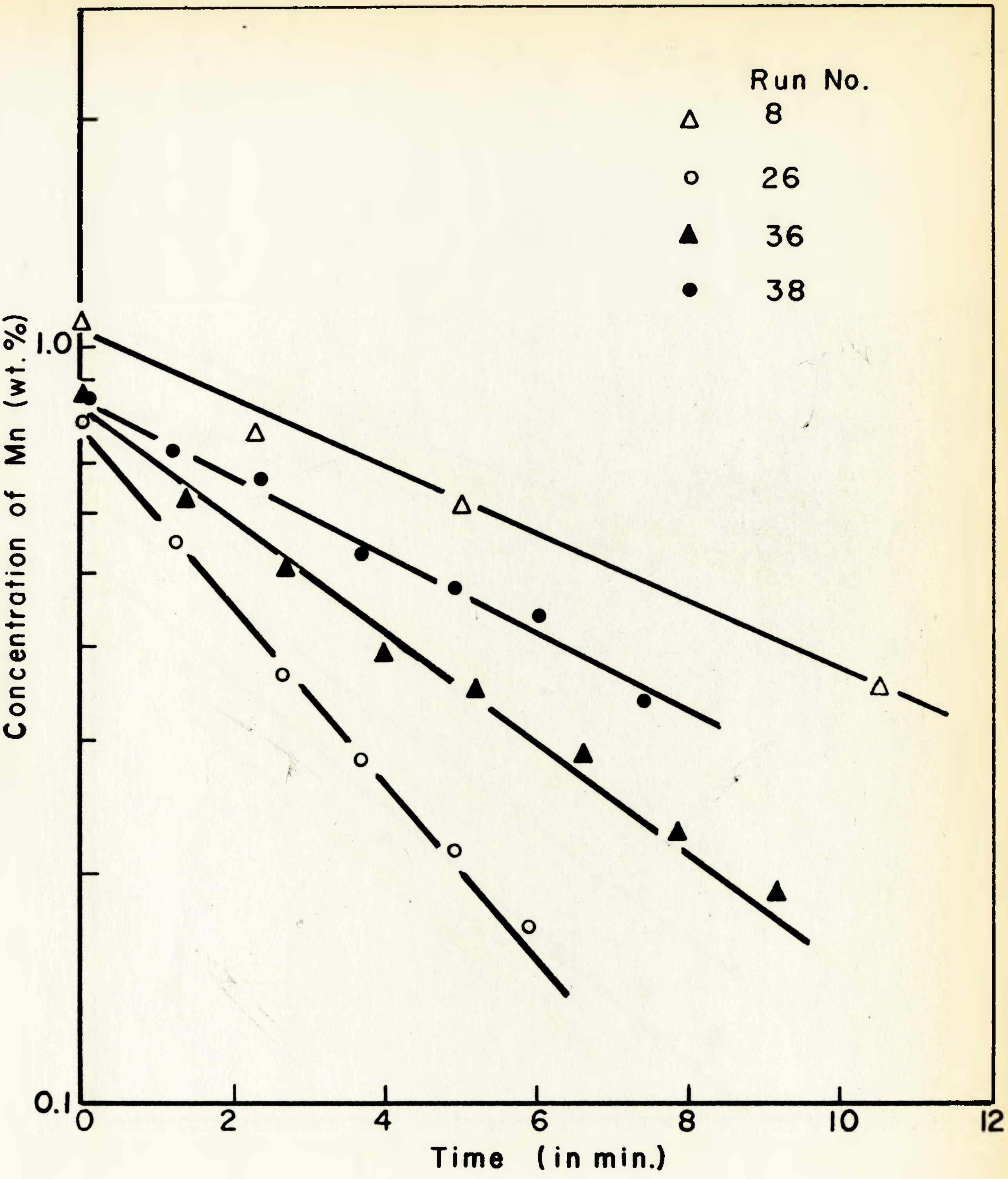

FIGURE 16

Concentration – Time Curves

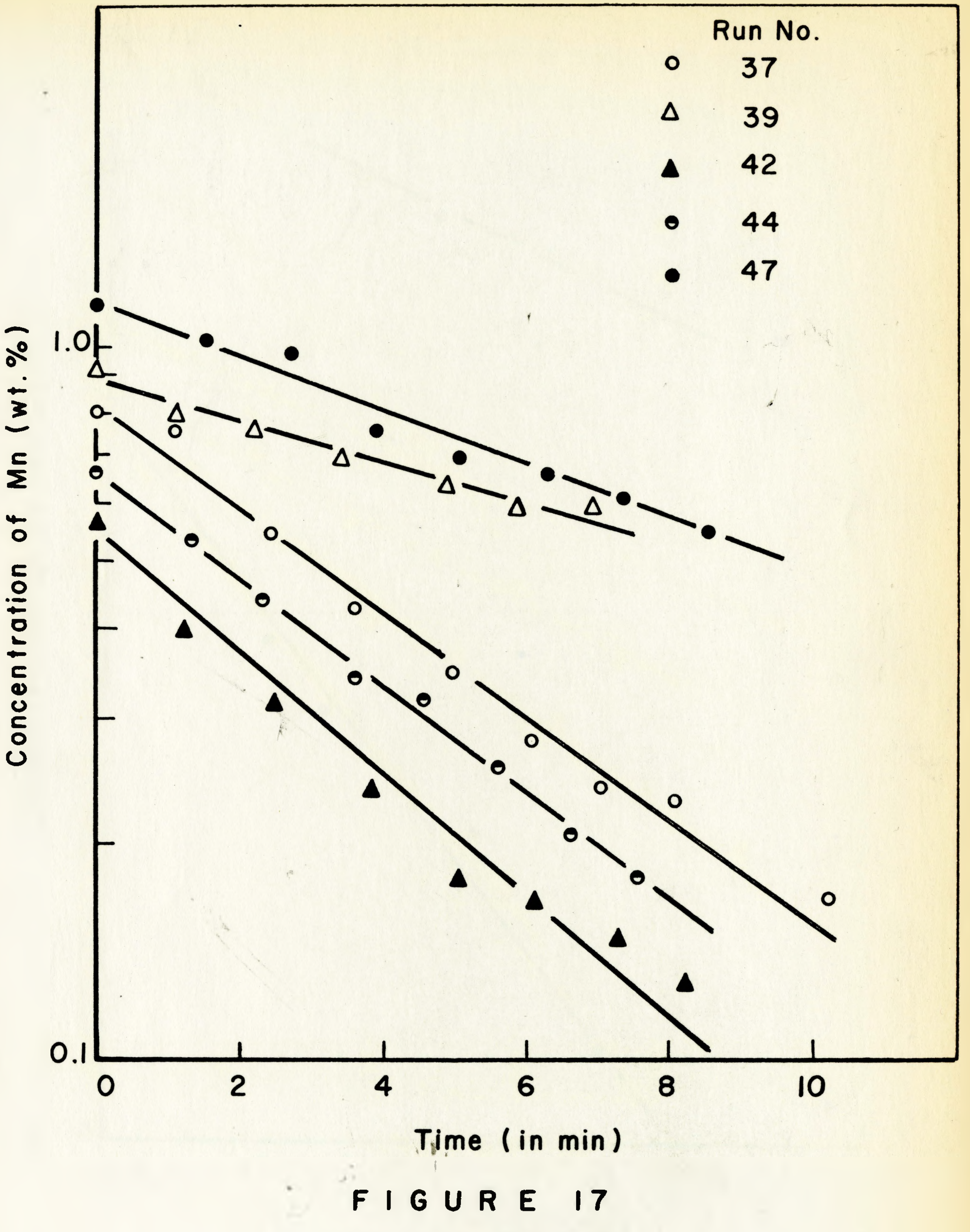

FIGURE 17

Concentration – Time Curves

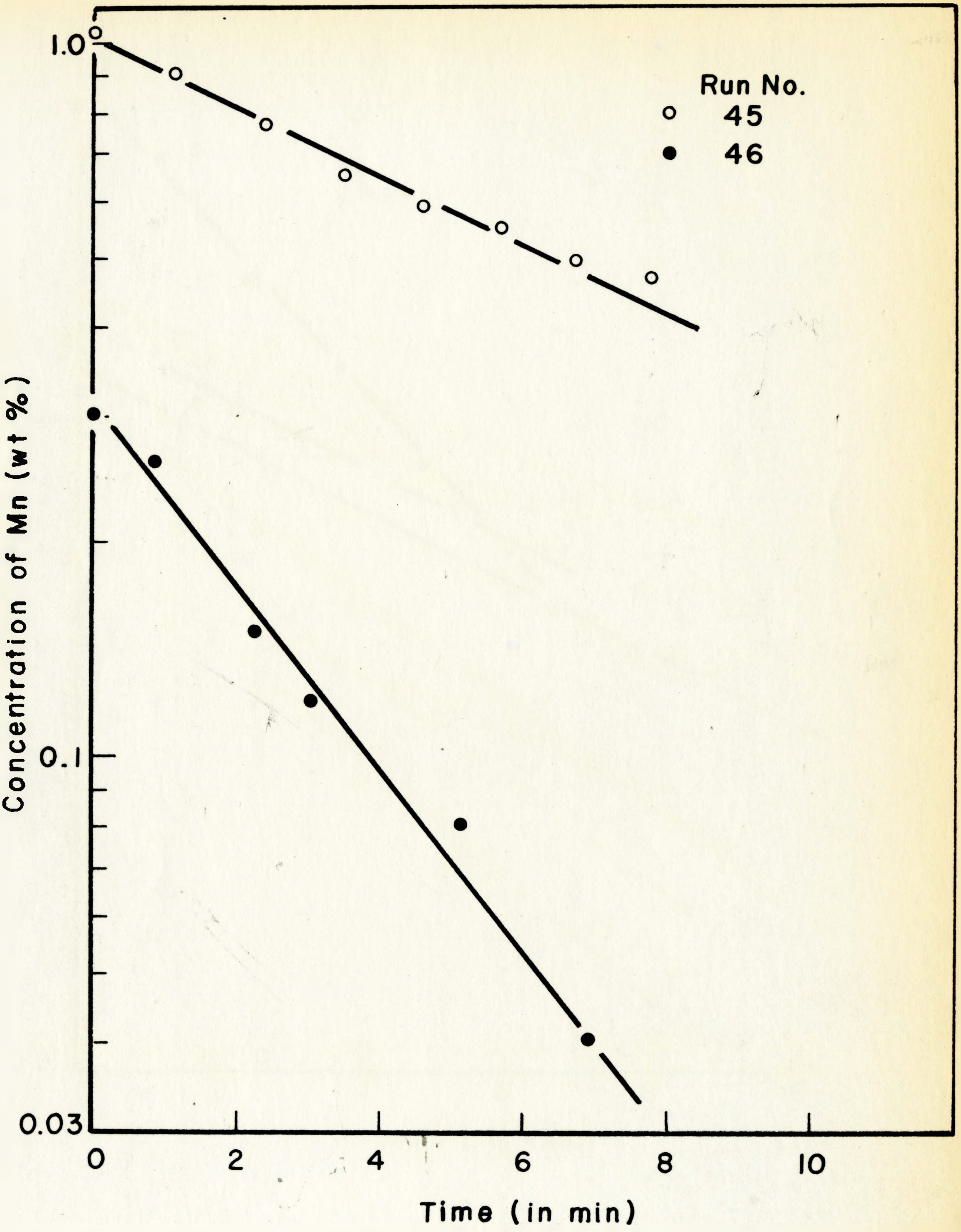

FIGURE 18

Concentration – Time Curves

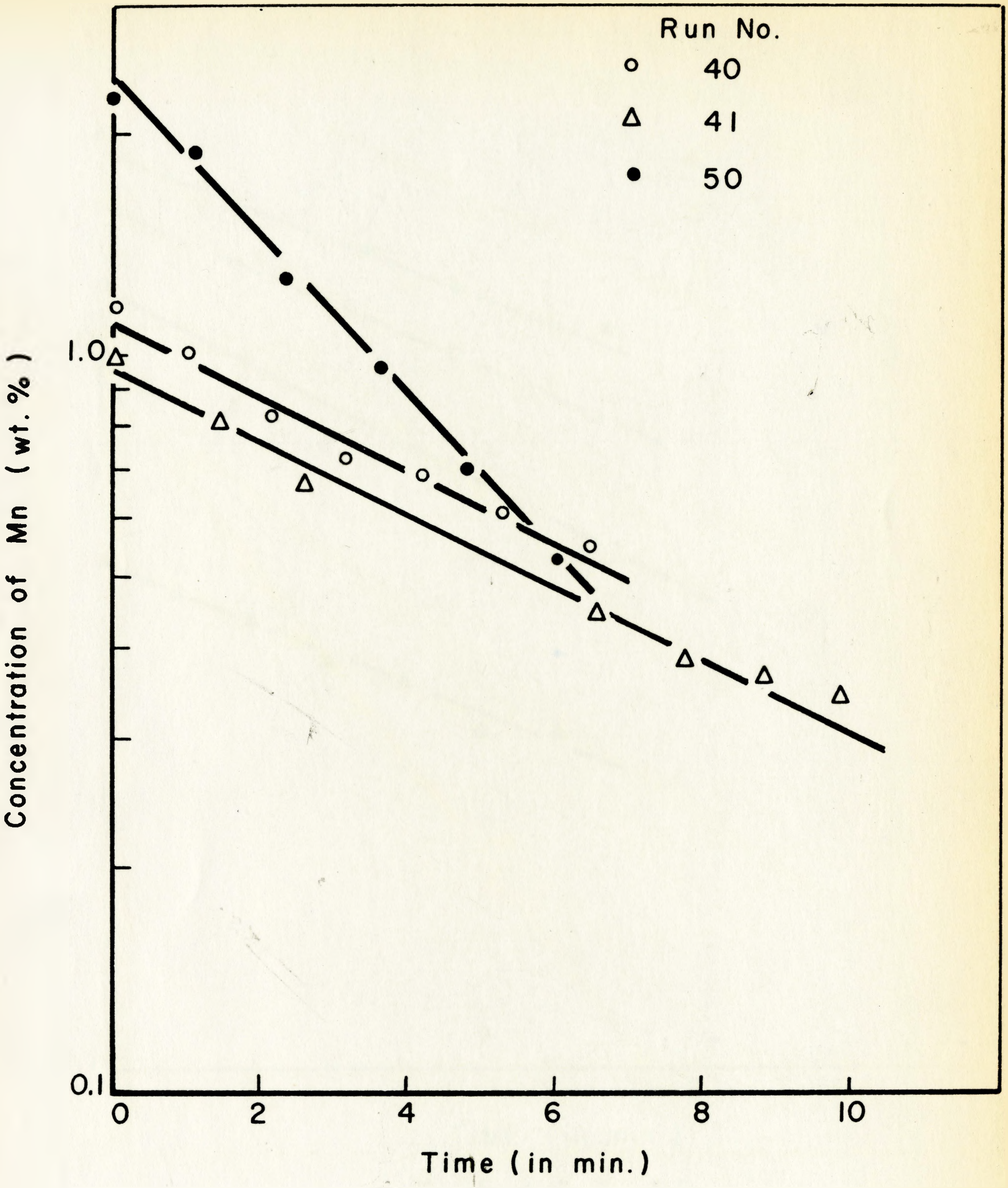

FIGURE 19

Concentration – Time Curves

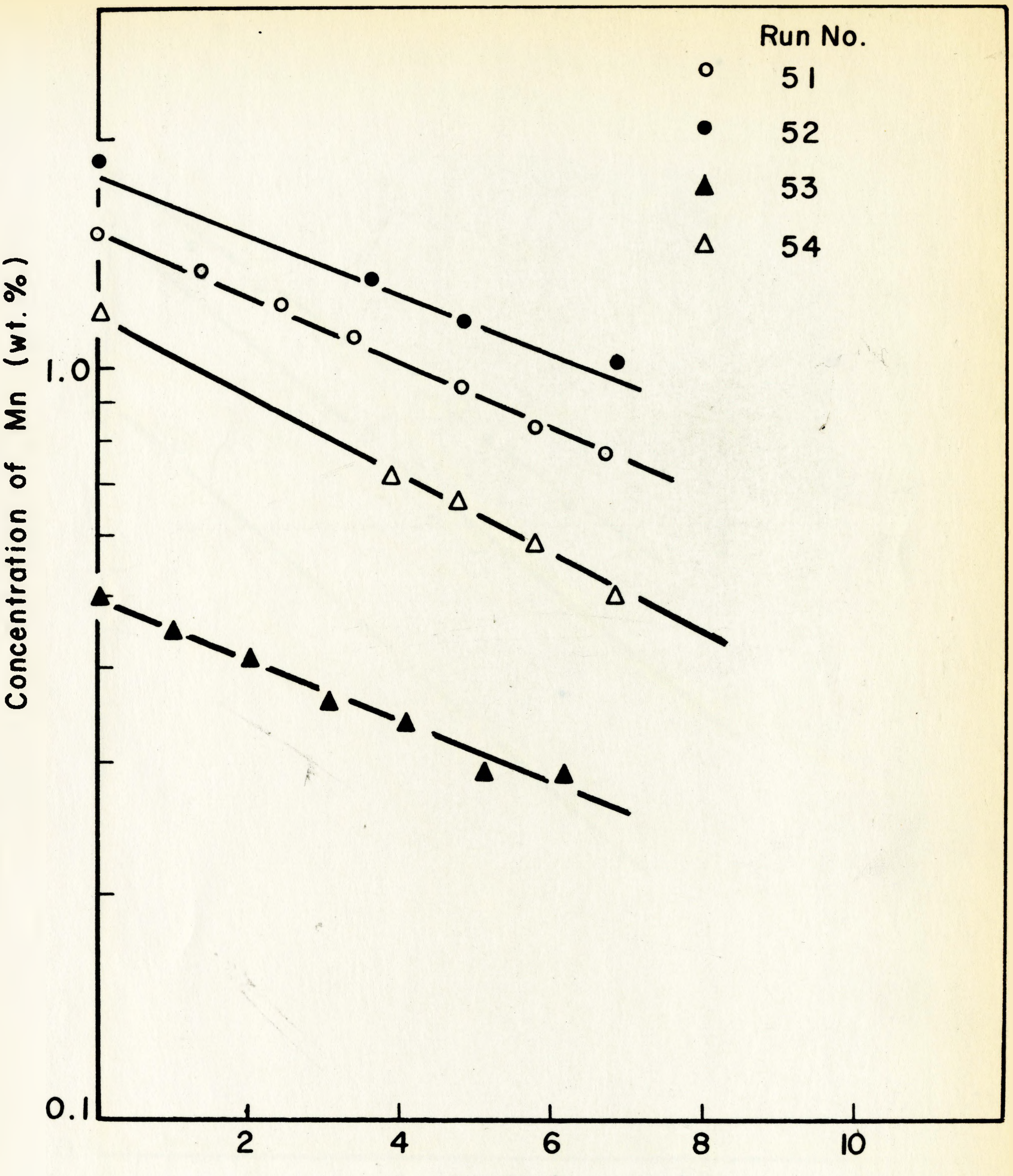

FIGURE 20

Concentration – Time Curves

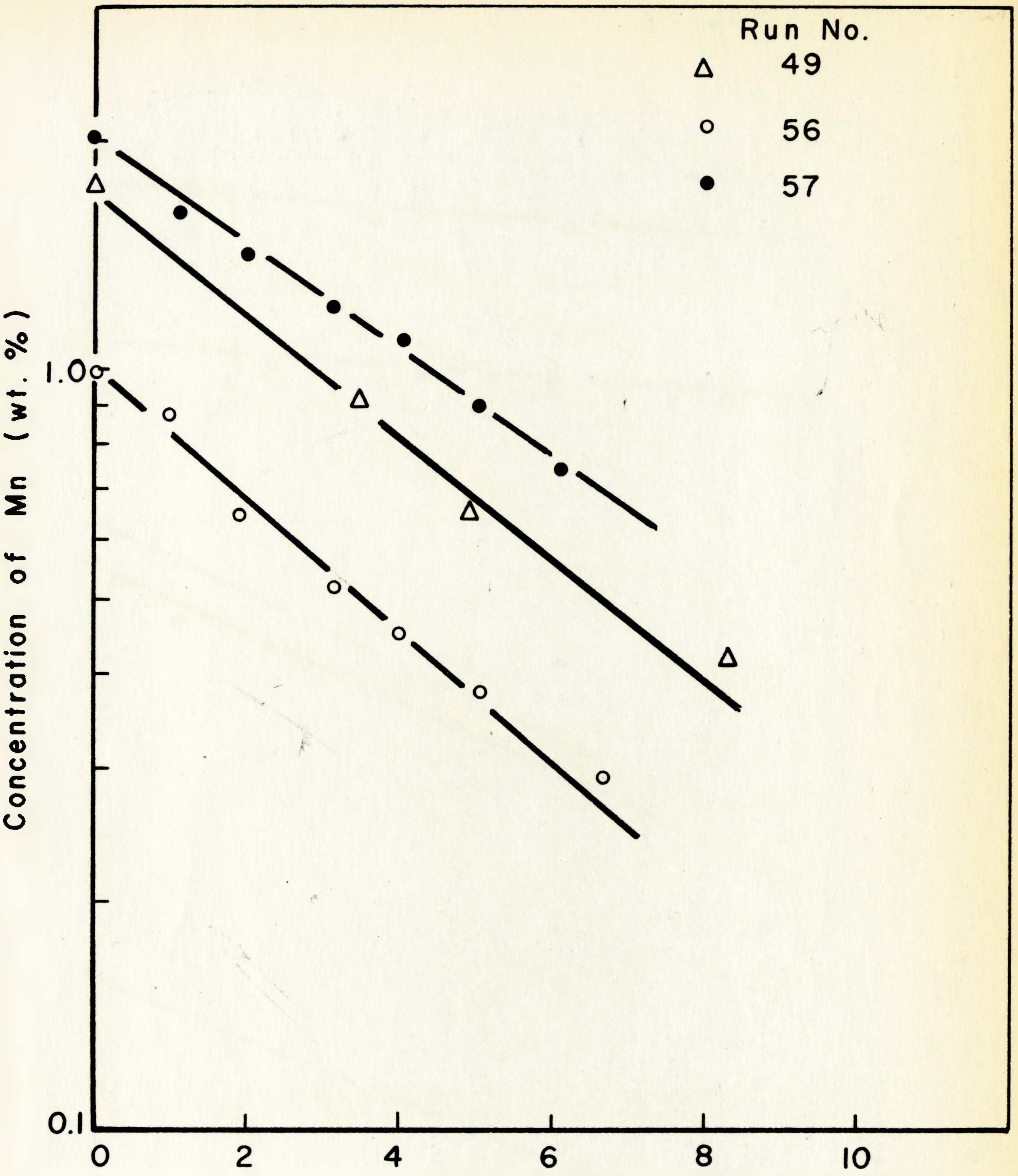

Concentration – Time Curves

FIGURE 21

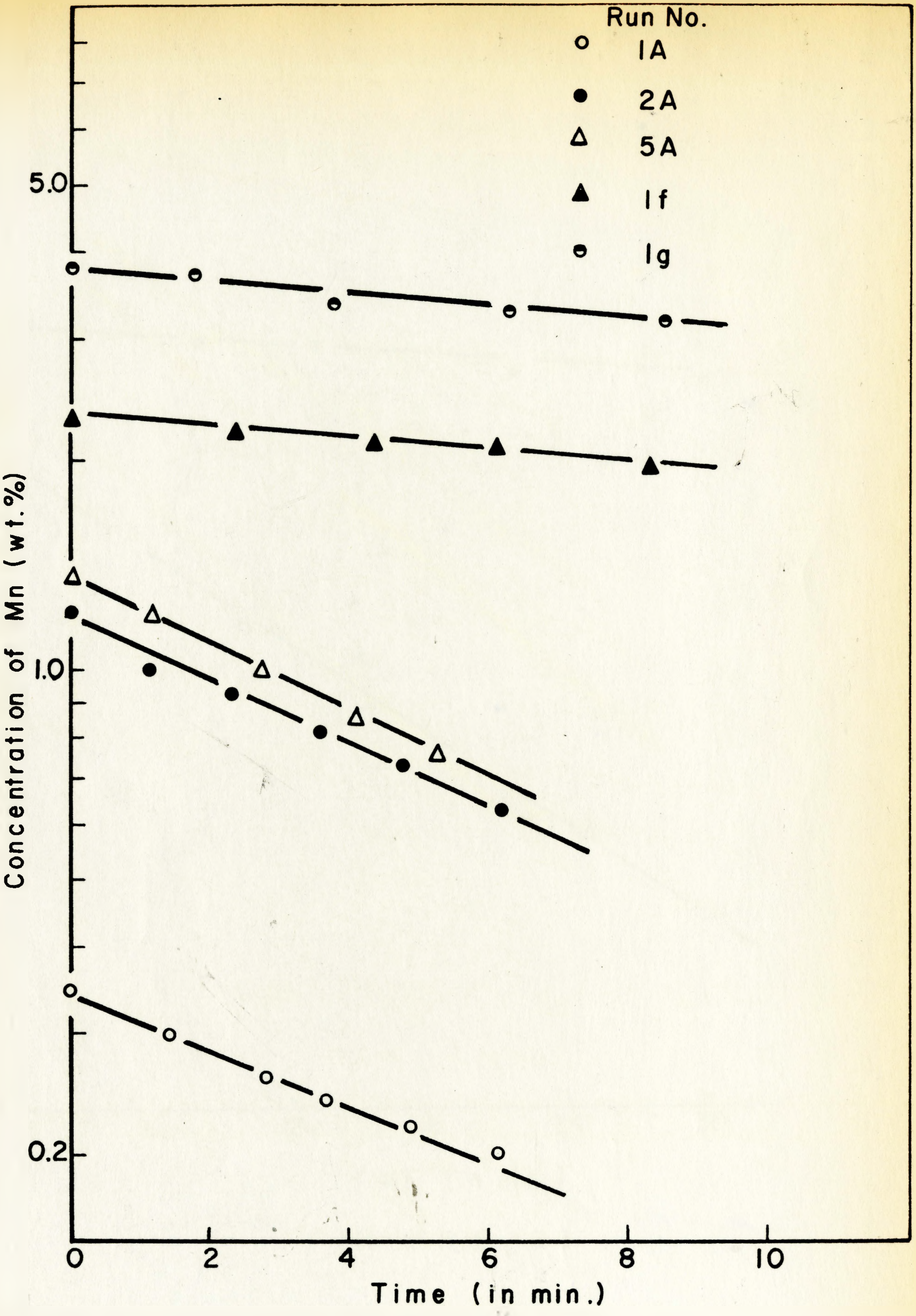

FIGURE 22

Concentration – Time Curves

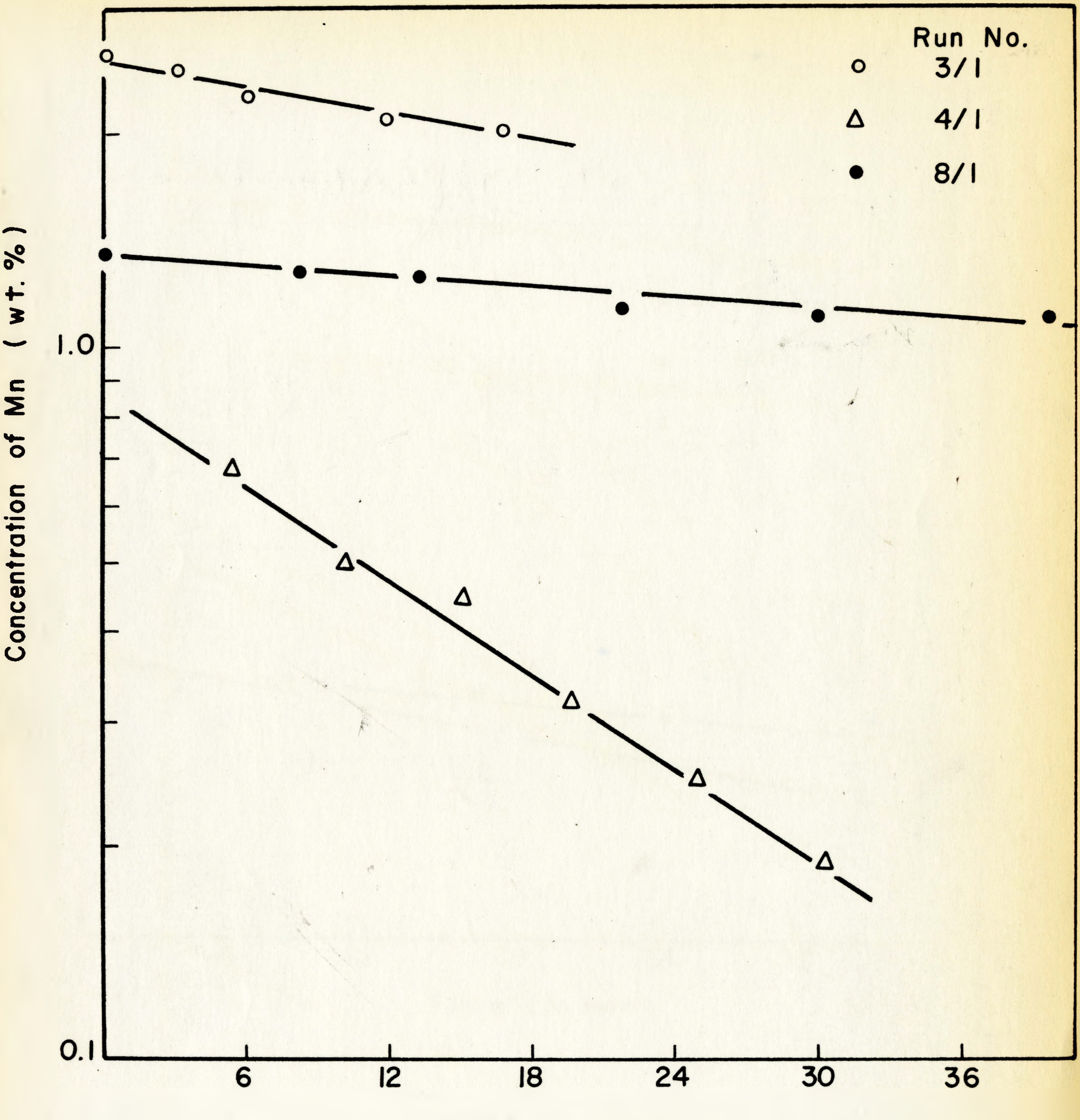

FIGURE 23
Concentration – Time Curves

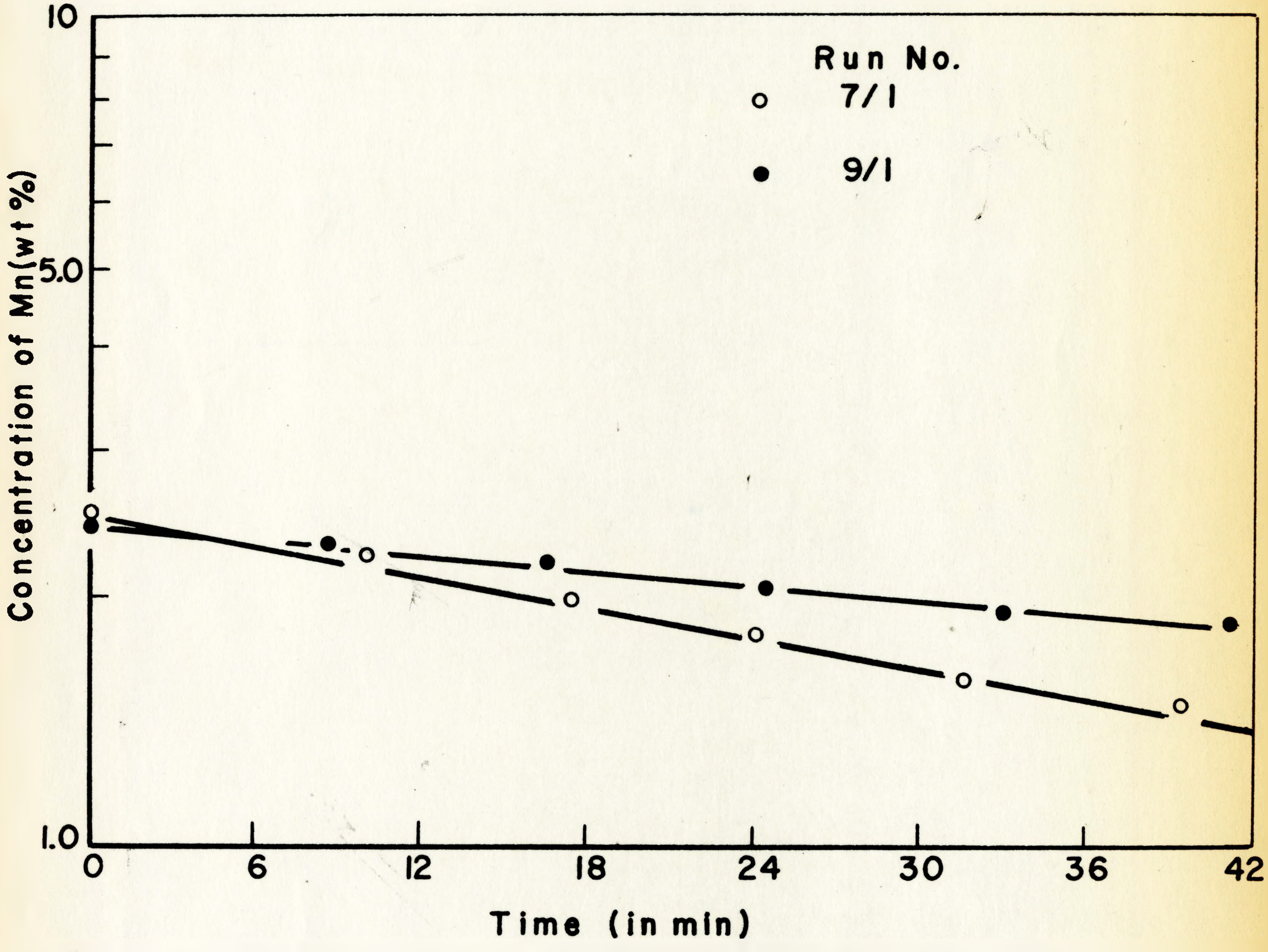

FIGURE 24

Concentration – Time Curves

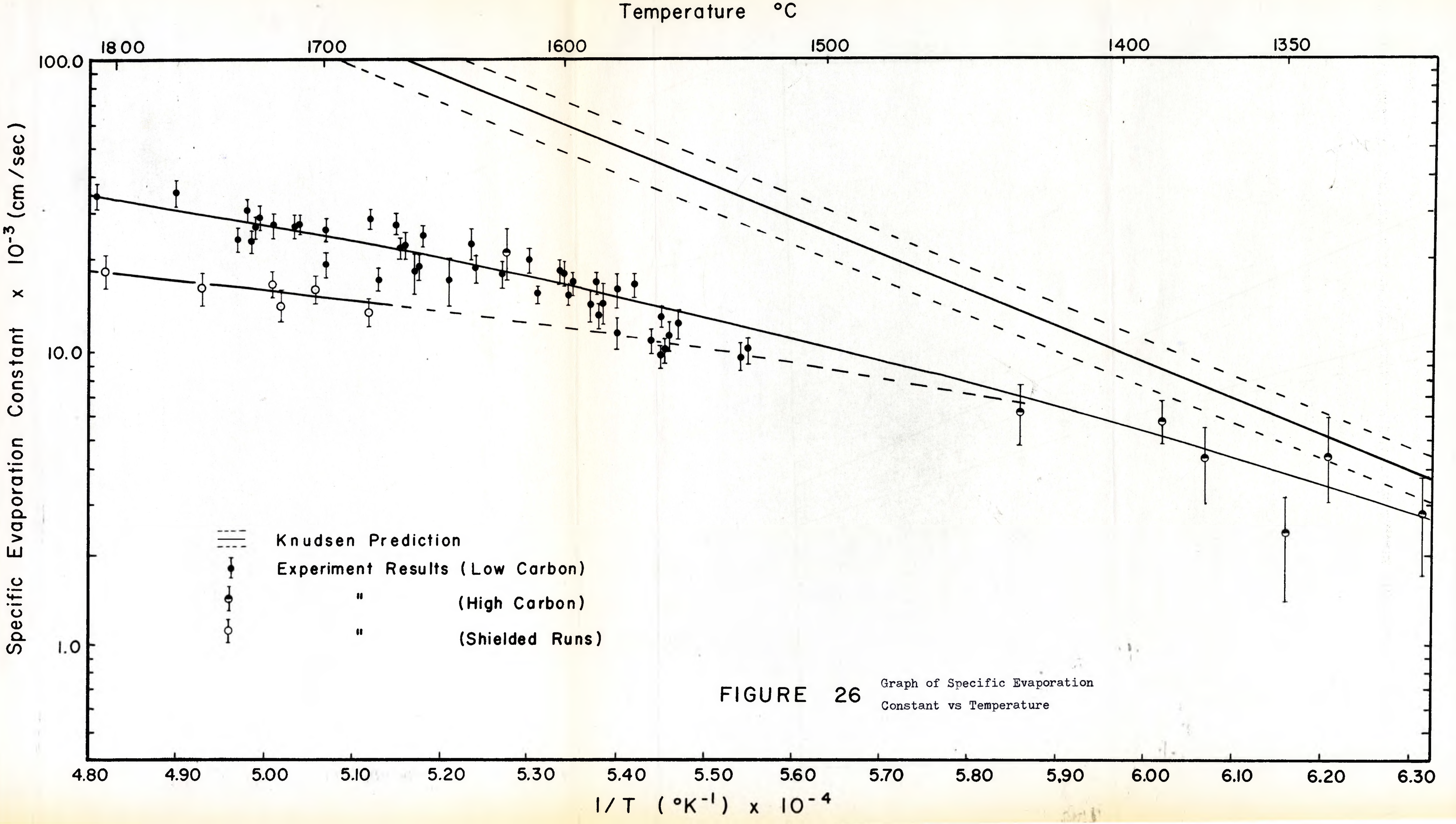

FIGURE 26 Graph of Specific Evaporation Constant vs Temperature

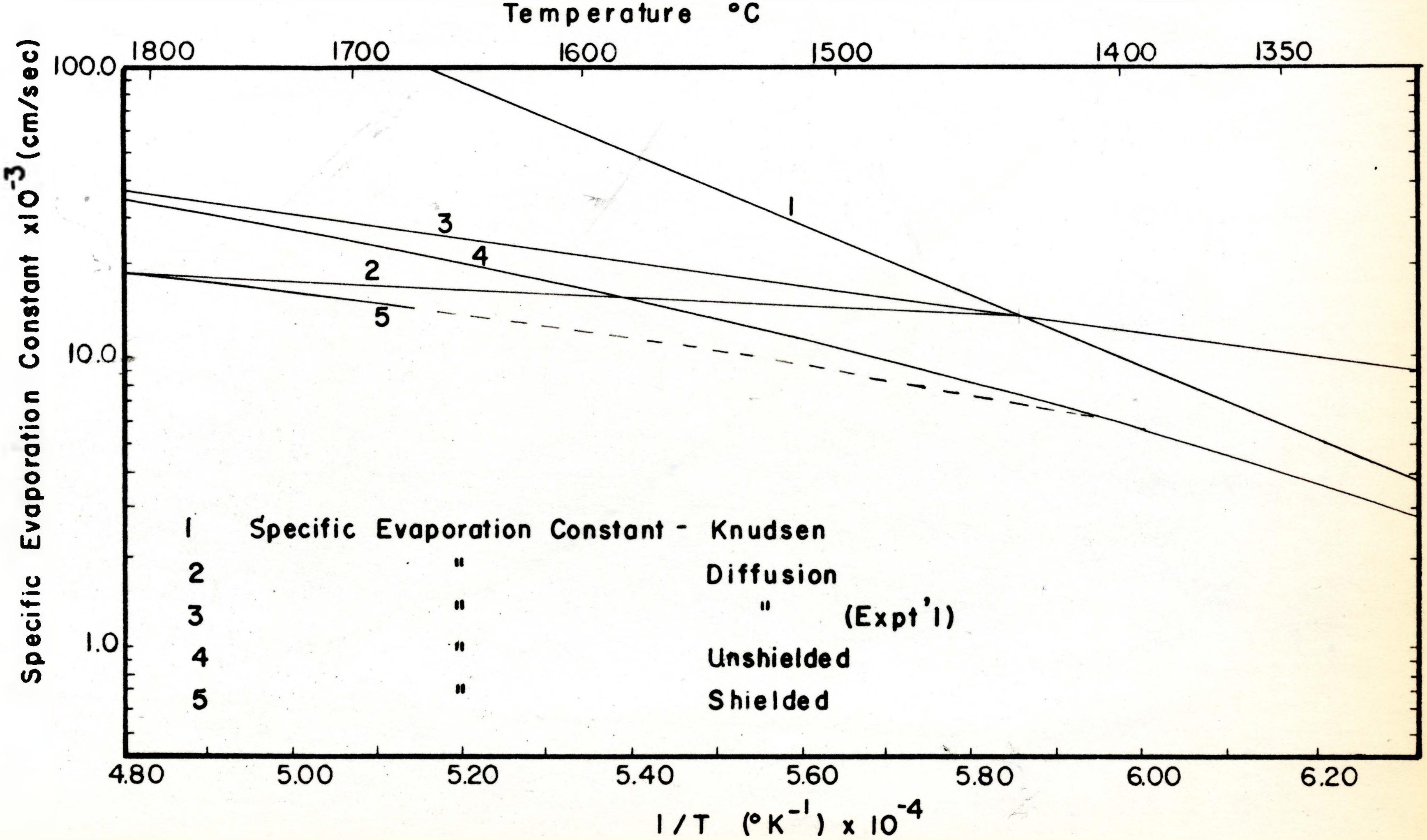

FIGURE 27

Specific Evaporation Constants as a function of Temperature

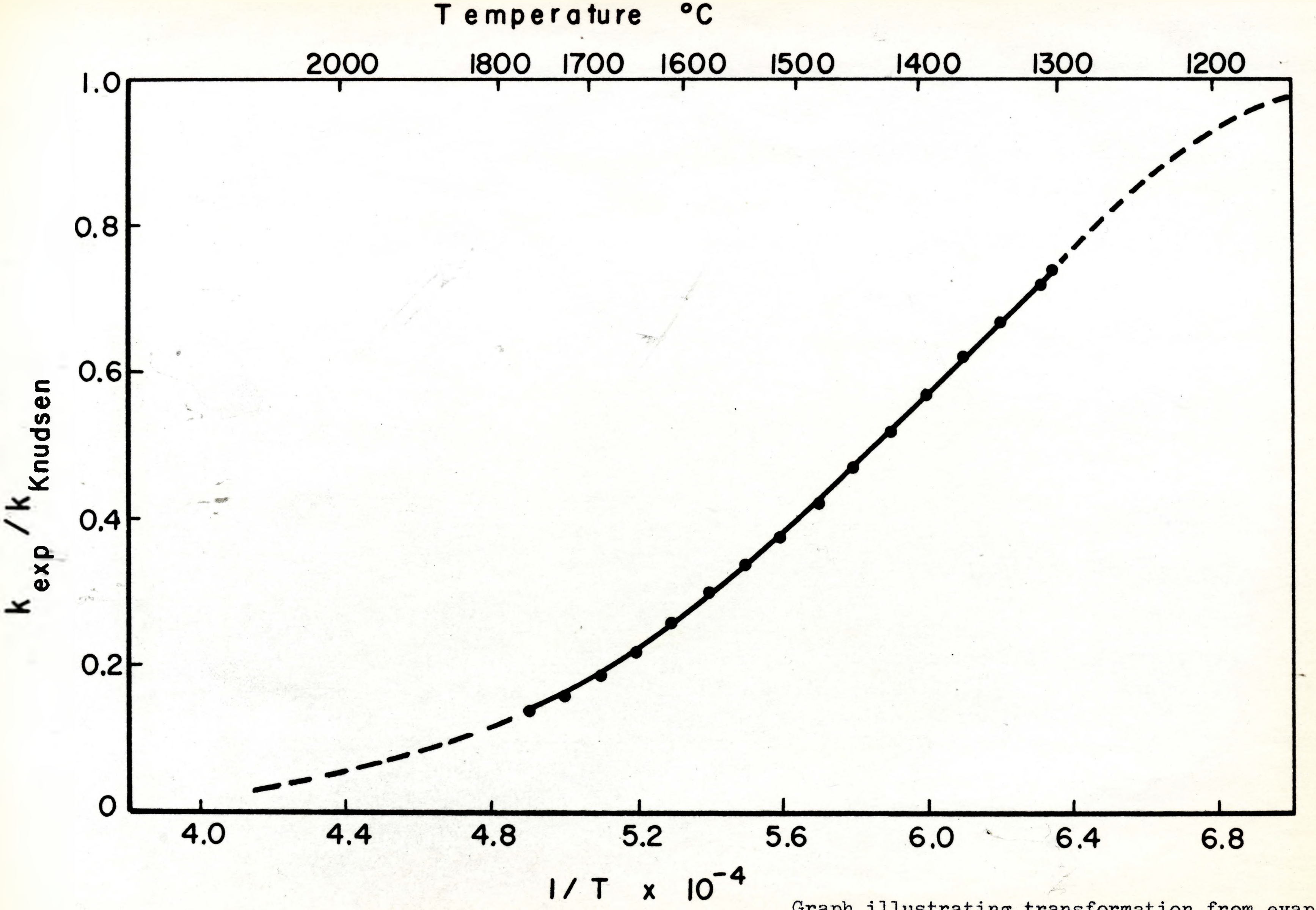

Graph illustrating transformation from evaporation control to diffusion control as the temperature is increased.

FIGURE 28

Figure 29 – Photograph of a magnesia crucible, showing the degree of penetration of the melt into the crucible wall

Figure 30: Micrograph illustrating the penetration of Iron into a Magnesia crucible; X100.